

Stratocumulus Convection off the West Coast of South America

By

Ellen J. Steiner
Wayne H. Schubert

Department of Atmospheric Science
Colorado State University
Fort Collins, Colorado



**Department of
Atmospheric Science**

Paper No. 270

STRATOCUMULUS CONVECTION OFF
THE WEST COAST OF SOUTH AMERICA

Ellen J. Steiner
Wayne H. Schubert

The research reported here has been supported
by the GARP Section of the Office of Climate
Dynamics, National Science Foundation
Grants DES 74-11438
ATM 76-09370

Department of Atmospheric Science
Colorado State University
Fort Collins, Colorado

May 1977

Atmospheric Science Paper No. 270

ABSTRACT

STRATOCUMULUS CONVECTION OFF
THE WEST COAST OF SOUTH AMERICA

The stratocumulus regime off the South American coast is investigated using a horizontally inhomogeneous version of Lilly's (1968) cloud topped mixed layer model. This model is coupled with a longwave radiation model devised by Cox (1973) and Cox et al. (1976). Computed are the mixed layer temperature and moisture structure and convective fluxes as the marine layer air moves equatorward along trajectories calculated from the mean surface wind field. By the calculation of many such trajectories, two dimensional fields of the model parameters were derived for the region bounded by 75°W and 100°W, and 2.5°S and 27.5°S. Model runs were made for mean July and August conditions, and sensitivity tests were performed to show the effects of solar absorption and different initial divergences. Variations in the mixed layer temperature and moisture structure, and convective fluxes are described for each of these experiments.

ACKNOWLEDGEMENTS

We wish to thank Dr. Stephen Cox for his advice and for the use of his radiation models, Mr. Garrett Campbell for his advice and assistance, and Mr. Roy Jenne for supplying much of the data used in the computations. For help in the preparation of this report we also wish to thank Dorothy Chapman, Susan Kuehl and Renee Jorgensen. This research was supported by the GARP Section of the Office of Climate Dynamics, National Science Foundation, Grants DES 74-11438 and ATM 76-09370.

TABLE OF CONTENTS

	<u>PAGE</u>
ABSTRACT	ii
ACKNOWLEDGEMENTS	iii
TABLE OF CONTENTS	iv
LIST OF FIGURES	v
LIST OF SYMBOLS	viii
1.0 INTRODUCTION	1
2.0 GOVERNING EQUATIONS.	5
3.0 PROCEDURE	10
3.1 Summary of the Governing Equations	10
3.2 Input Parameters	12
3.3 Trajectory Calculation	18
4.0 RESULTS	22
4.1 Results of the July Case	22
4.2 Results of the August Case	56
4.3 Results of the July Case with No Solar Absorption	75
4.4 Results of the July Case with a Different Initial Divergence	88
5.0 CONCLUSIONS	93
REFERENCES	96

LIST OF FIGURES

<u>FIGURE</u>		<u>PAGE</u>
1.1	Four year average (1967-1970) of cloud brightness for January and July (from Miller and Feddes, 1971).	2
1.2	Schematic diagram of a stratocumulus topped mixed layer. Shown are the total water mixing ratio, $q+\ell$, the saturation mixing ratio, q^* , and the moist static energy, h , for the case of the air temperature slightly warmer than the sea surface. Very near the surface the air is saturated at sea surface temperature and pressure, so h and q are equal to their surface saturation values, h_S^* and q_S^* . Above a shallow, nearly saturated layer, h and $q+\ell$ become mixed (h_M and $(q+\ell)_M$). At the top of the mixed layer, the warm, dry air results in discontinuities of h , $q+\ell$, and q^* .	3
3.1	One month averaged 00Z July and August temperature and mixing ratio profiles for the stations Guayaquil (2.15°S, 79.88°W), indicated by the dotted lines, Lima (12.02°S, 77.13°W), indicated by the dash-dot lines, and Antofagasta (23.42°S, 70.47°W), indicated by the solid lines.	14
3.2	July and August dry static energy, s , moist static energy, h , and saturation moist static energy, h^* , profiles for Guayaquil, Lima, and Antofagasta. Dashed lines indicate the extrapolated values.	15
3.3	July and August downward longwave radiative flux for Guayaquil, Lima, and Antofagasta.	17
3.4	Method used for the trajectory computation. (See explanation in text.)	19
4.1	The July input variables of a) sea surface temperature, b) surface wind speed, and c) large-scale divergence. Heavy lines indicate trajectories. On the graph of sea surface temperature, the trajectory beginning at 76.5°W, 27.5°S is marked every 300 km with the time in hours from initialization.	23
4.2	July a) cloud top, b) cloud base, c) depth of the cloud layer, and d) cloud top temperature.	27
4.3	July mixed layer a) moist static energy, and b) total water mixing ratio.	32

<u>FIGURE</u>		<u>PAGE</u>
4.4	July vertical profiles of the turbulent moist static energy flux every 300 km along the trajectory beginning at 76.5°W, 27.5°S. Time in hours from initialization is indicated.	34
4.5	July vertical profiles of the turbulent flux of total water every 300 km along the trajectory beginning at 76.5°W, 27.5°S. Time in hours from initialization is indicated.	35
4.6	July turbulent moist static energy fluxes at a) the surface and b) top of the layer.	37
4.7	July turbulent flux of total water at a) the surface, and b) top of the layer.	39
4.8	July vertical profiles of the turbulent virtual dry static energy flux every 300 km along the trajectory beginning at 76.5°W, 27.5°S. The time in hours from initialization is indicated.	41
4.9	July turbulent flux of virtual dry static energy at a) the surface, b) just below cloud base, c) just above cloud base, and d) layer top.	43
4.10	July jump of a) total radiative flux, and b) moist static energy at cloud top.	48
4.11	July a) jump of radiative flux at cloud top minus the turbulent flux of moist static energy at cloud top, and b) the mass entrainment at cloud top.	50
4.12	July difference between the sea surface temperature and the air temperature at the surface.	52
4.13	July a) β , b) γ , and c) b.	53
4.14	The August input variables of a) sea surface temperature, b) surface wind speed, and c) large-scale divergence. Heavy lines indicate trajectories.	57
4.15	August a) cloud top, b) cloud base, and c) depth of the cloud layer.	61
4.16	August mixed layer a) moist static energy and b) total water mixing ratio.	64
4.17	August turbulent flux of moist static energy at a) the surface and b) top of the layer.	66
4.18	August turbulent flux of total water at a) the surface, and b) top of the layer.	68

<u>FIGURE</u>		<u>PAGE</u>
4.19	August turbulent flux of virtual dry static energy at a) the surface, b) just below cloud base, c) just above cloud base, and d) layer top.	70
4.20	August jump of total radiative flux at cloud top.	74
4.21	a) Cloud top, b) cloud base, and c) depth of the cloud layer for the July case with no solar absorption.	76
4.22	Mass entrainment at cloud top for the July case with no solar absorption.	80
4.23	Turbulent flux of moist static energy at a) the surface and b) top of the layer for the July case with no solar absorption.	81
4.24	Turbulent flux of total water at a) the surface and b) top of the layer for the July case with no solar absorption.	83
4.25	Jump of a) total radiative flux, and b) moist static energy at cloud top for the July case with no solar absorption.	85
4.26	Difference between the sea surface temperature and the air temperature at the surface for the July case with no solar absorption.	87
4.27	a) Cloud top, b) cloud base, and c) depth of the cloud layer for the July case with an initial divergence of $3.0 \times 10^{-6} \text{sec}^{-1}$.	89
4.28	Jump of moist static energy at cloud top for the July case with an initial divergence of $3.0 \times 10^{-6} \text{sec}^{-1}$.	92

LIST OF SYMBOLS

Subscripts and Superscripts

$()_B$	Value at layer top
$()_M$	Mixed layer value
$()_S$	Surface value
$()^+$	Just above level ()
$()^-$	Just below level ()
$()^*$	Saturation value

English Symbols

a	Radius of the earth
b	Dimensionless variable defined in (2.19)
c_p	Specific heat at constant pressure
C_T	Transfer coefficient
d	Distance increment
D	Large-scale divergence
$F_{L\downarrow}$	Downward longwave radiative flux
$(F_{L\downarrow})_0$	Reference downward longwave flux
g	Gravity
h	Moist static energy
h_0	Reference moist static energy
H	Scale height
k	Entrainment parameter
λ	Liquid water mixing ratio
L	Latent heat of condensation
p	Pressure
q	Water vapor mixing ratio
q_0	Reference water vapor mixing ratio

$q+l$	Total water vapor plus liquid water mixing ratio
R	Gas constant
s	Dry static energy
s_V	Virtual dry static energy
t	Time
T	Temperature
V	Surface wind speed
w_B	Large-scale subsidence at cloud top
$\overline{w'h'}$	Turbulent flux of moist static energy
$\overline{w'l'}$	Turbulent flux of liquid water
$\overline{w'q'}$	Turbulent flux of water vapor
$\overline{w'(q'+l')}$	Turbulent flux of water vapor plus liquid water
$\overline{w's_V'}$	Turbulent flux of virtual dry static energy
$(\overline{w's_V'})_{\min}$	Minimum virtual dry static energy flux
$\overline{w'T'}$	Turbulent heat flux
x	Downstream distance
z	Height
z_B	Cloud top
z_C	Cloud base

Greek Symbols

α	Direction towards which the wind is blowing
β	Dimensionless variable defined in (2.19)
γ	Dimensionless variable defined in (2.19)
δ	Constant defined in (2.19)
ΔF_L	Jump of longwave radiative flux at cloud top
ΔF_R	Jump of total radiative flux at cloud top

ΔF_S	Jump of shortwave radiative flux at cloud top
Δh	Jump of moist static energy at cloud top
$\Delta(q+\ell)$	Jump of water vapor plus liquid water at cloud top
ϵ	Dimensionless variable defined in (2.19)
λ	Longitude
ρ	Density
σ	Stefan-Boltzman constant
ϕ	Latitude

1.0 INTRODUCTION

One of the most constant features of the general circulation of the atmosphere are the stratocumulus clouds which occur in the descending branches of the Hadley circulation of both the northern and southern hemispheres. These clouds, which are seasonally a semi-permanent atmospheric feature covering a considerable portion of the subtropics, have recently come under theoretical (Lilly, 1968; Deardorff, 1976; Schubert, 1976; Schubert, Wakefield, Steiner and Cox, 1977) and observational (Wakefield and Schubert, 1976) study. Stratocumulus are prevalent in the eastern oceans as a result of the large-scale oceanic and atmospheric conditions there. Figure 1.1 shows the four year (1967-70) average cloud brightness for January and July. The most striking examples of stratocumulus occur in July off the coasts of California, Peru and Chile, and Southwest Africa. Equatorward of the stratocumulus there exists the trade cumulus regime, characterized by small fractional area of cloudiness, and the cumulonimbus regime, characterized by its narrow band of intense low level convergence. In this paper, we investigate the stratocumulus regime using a horizontally inhomogeneous version of Lilly's (1968) cloud-topped mixed layer model. By solving the model equations along trajectories, we model the modification of the marine layer air as it moves equatorward, circling around the subtropical high. The specific case covered is that of stratocumulus off the South American coast.

A schematic diagram of stratocumulus is presented in Figure 1.2. Stratocumulus are low level clouds which usually increase in height and depth away from the coast. They exist below the trade inversion, capping a marine layer mixed in moist static energy, h , ($=c_p T + gz + Lq$)

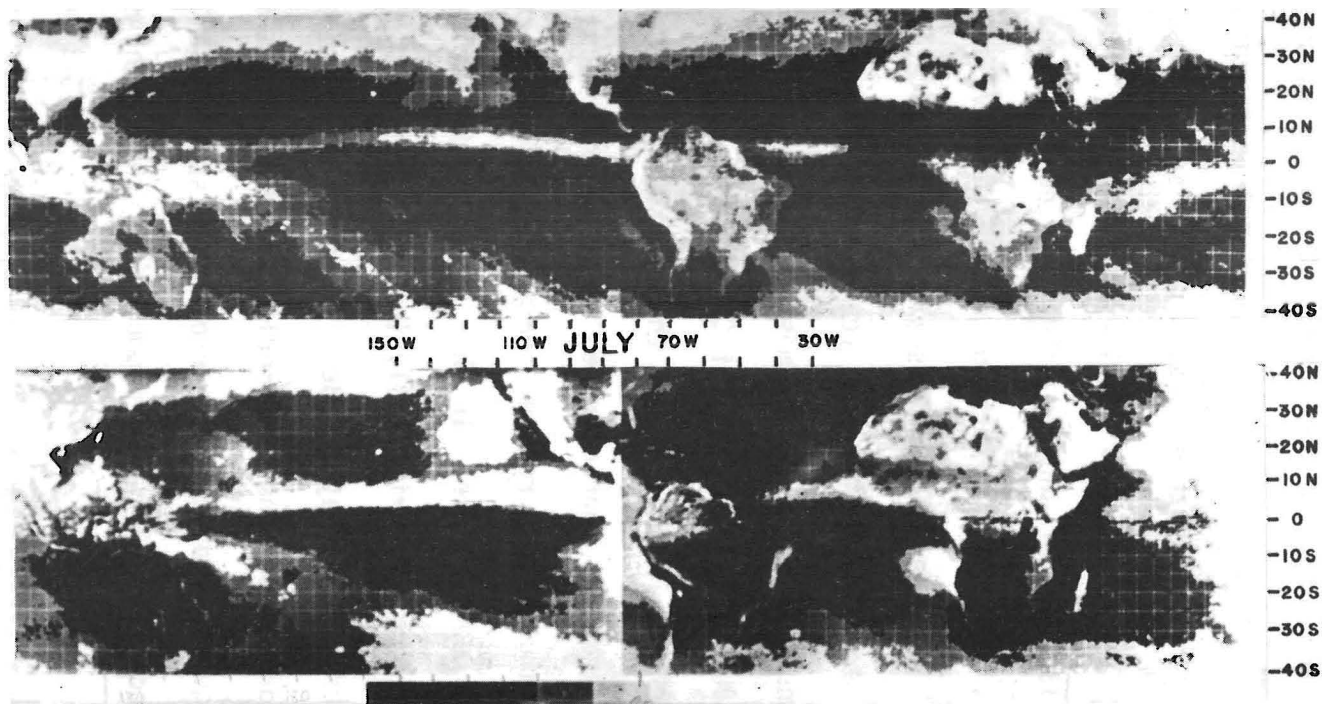


Figure 1.1 Four year average (1967-1970) of cloud brightness for January and July (from Miller and Feddes, 1971).

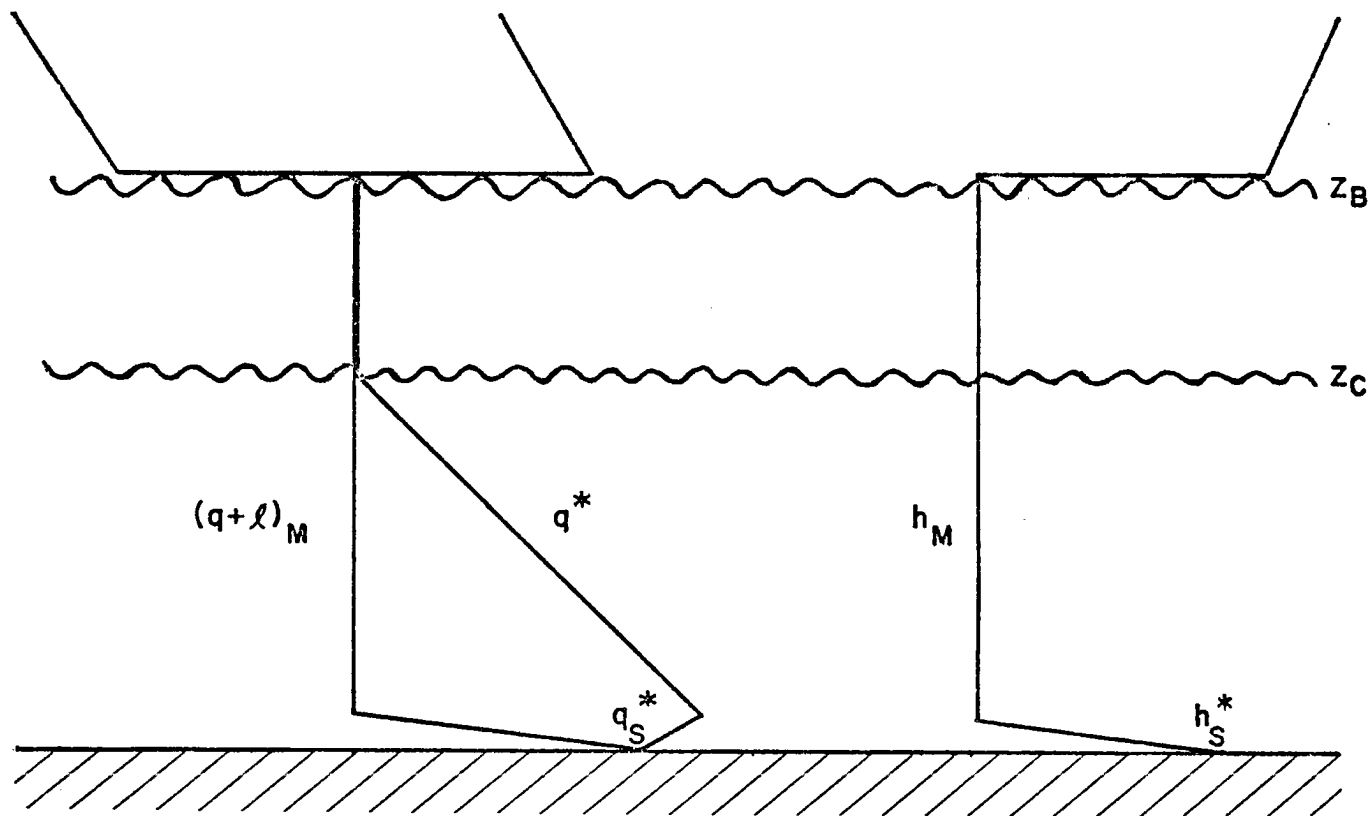


Figure 1.2 Schematic diagram of a stratocumulus topped mixed layer. Shown are the total water mixing ratio, $q+l$, the saturation mixing ratio, q^* , and the moist static energy, h , for the case of the air temperature slightly warmer than the sea surface. Very near the surface the air is saturated at sea surface temperature and pressure, so h and q are equal to their surface saturation values, h_S^* and q_S^* . Above a shallow nearly saturated layer, h and $q+l$ become mixed (h_M and $(q+l)_M$). At the top of the mixed layer, the warm, dry air results in discontinuities of h , $q+l$, and q^* .

and total water content, $q+\lambda$. Thus, they rarely rain. In this model, the trade inversion is considered to be infinitesimally thin, resulting in "jumps", or discontinuities of h , $q+\lambda$, and radiative flux at cloud top.

In Chapter 2, we review the governing equations and in Chapter 3 the computational procedure. Results of model runs for mean July and August conditions are presented in Chapter 4.

2.0 GOVERNING EQUATIONS

In this chapter we present a brief summary of the governing equations of the model. A more complete discussion can be found in Lilly (1968), Schubert (1976) and Schubert, Wakefield, Steiner and Cox (1977).

The turbulent fluxes of moist static energy, h , and total water mixing ratio, $q+\ell$, at the bottom of the mixed layer are given by

$$\overline{w'h'}_S = C_T V (h_S^* - h_M), \quad (2.1)$$

$$\overline{w'(q+\ell)'}_S = C_T V (q_S^* - (q+\ell)_M), \quad (2.2)$$

where C_T is the transfer coefficient, V is the surface wind speed, and h_M and $(q+\ell)_M$ are the mixed layer moist static energy and total water mixing ratio, respectively. h_S^* and q_S^* are the saturation values of h and q at sea surface temperature, T_S , and pressure, p_S . Henceforth, the subscript "S" will denote values at the surface, the subscript "B" will denote values at layer top, and the subscript "M" will denote mixed layer values. Thus, the turbulent fluxes at the bottom of the layer are directly proportional to the surface wind speed and the difference between the surface saturation and mixed layer values of h and $q+\ell$.

The mixed layer budgets of moist static energy and total water are given by

$$\frac{\partial h_M}{\partial t} + V \frac{\partial h_M}{\partial x} = - \frac{\partial}{\partial z} \overline{w'h'}, \quad (2.3)$$

and

$$\frac{\partial (q+\ell)_M}{\partial t} + V \frac{\partial (q+\ell)_M}{\partial x} = - \frac{\partial}{\partial z} \overline{w'(q+\ell)'}, \quad (2.4)$$

where V is the component of wind in the downstream x -direction. Since the layer is mixed with respect to h and $q+\ell$, the turbulent fluxes of h and $q+\ell$ must be linear functions of height. Therefore,

$$\overline{w'h'} = \left(1 - \frac{z}{z_B}\right) (\overline{w'h'})_S + \frac{z}{z_B} (\overline{w'h'})_B, \quad (2.5)$$

$$\overline{w'(q'+\ell')} = \left(1 - \frac{z}{z_B}\right) \overline{w'(q'+\ell')}_S + \frac{z}{z_B} \overline{w'(q'+\ell')}_B, \quad (2.6)$$

where z_B represents mixed layer depth (i.e. cloud top height). Differentiating (2.5) and (2.6) with respect to height and substituting into (2.3) and (2.4) yields

$$\frac{\partial h_M}{\partial t} + V \frac{\partial h_M}{\partial x} = \frac{[(\overline{w'h'})_S - (\overline{w'h'})_B]}{z_B}, \quad (2.7)$$

$$\frac{\partial (q+\ell)_M}{\partial t} + V \frac{\partial (q+\ell)_M}{\partial x} = \frac{[\overline{w'(q'+\ell')}_S - \overline{w'(q'+\ell')}_B]}{z_B}. \quad (2.8)$$

These equations indicate that the advective plus local time change of h_M and $(q+\ell)_M$ is directly proportional to the divergence of the turbulent fluxes of these quantities.

Integrating the budget equations for h and $q+\ell$ in the inversion layer at cloud top and taking the limit as the depth of that layer goes to zero yields

$$\left(\frac{\partial z_B}{\partial t} + V \frac{\partial z_B}{\partial x} - w_B\right) \Delta h + (\overline{w'h'})_B = \frac{\Delta F_R}{\rho}, \quad (2.9)$$

$$\left(\frac{\partial z_B}{\partial t} + V \frac{\partial z_B}{\partial x} - w_B\right) \Delta(q+\ell) + \overline{w'(q'+\ell')}_B = 0, \quad (2.10)$$

where w_B is the large-scale subsidence at the top of the layer, given by $-\text{divergence} \cdot z_B$, Δh and $\Delta(q+\ell)$ are the "jumps" of h and $q+\ell$ at

cloud top (that is, their values just above cloud top minus their mixed layer values), and ΔF_R is the jump of radiative flux at the top of the layer. For the computation of ΔF_R , we need to know the temperature just below cloud top. The dry static energy just below cloud top is given by the dry static energy at cloud base plus the change that occurs when following a moist adiabat from cloud base to cloud top, i.e.

$$s(z_B^-) = s(z_C) + \left(\frac{\partial s}{\partial z}\right)_{h^*} (z_B - z_C). \quad (2.11)$$

Since it can be shown that

$$\left(\frac{\partial s}{\partial z}\right)_{h^*} = \frac{L}{T + \gamma} \frac{b}{H}, \quad (2.12)$$

where H is the scale height, RT_S/g , and γ and b are defined in (2.19), and since $s(z_C)$ is $h_M - L(q+\ell)_M$, we can rewrite (2.11) as

$$T(z_B^-) = \frac{1}{c_p} [h_M - L(q+\ell)_M + \frac{L}{T+\gamma} \frac{b}{H} (z_B - z_C) - gz_B]. \quad (2.13)$$

The net mass flow into the mixed layer per unit horizontal area per unit time is given by $\rho \left(\frac{\partial z_B}{\partial t} + V \frac{\partial z_B}{\partial x} - w_B \right)$, where ρ is the density. Such a mass flux can be due to a local increase in mixed layer depth with time, a horizontal flow across the top of the mixed layer when it deepens in the downstream direction, a large-scale subsidence, or a combination of these three effects.

In order that (2.9) and (2.10) predict cloud top consistently, we can combine them to give

$$\frac{\frac{\Delta F_R}{\rho} - (w'h')_B}{\Delta h} = \frac{-w'(q'+\ell')_B}{\Delta(q+\ell)}. \quad (2.14)$$

Cloud base, z_C , is given by

$$\frac{z_C}{H} = \frac{(\gamma+1) [q_S^* - (q+\ell)_M] - \frac{\gamma}{L} [h_S^* - h_M]}{b} \quad (2.15)$$

Equation (2.15) indicates that cloud base will rise as the mixed layer warms or dries.

A weighted average of Lilly's (1968) maximum and minimum entrainment conditions discussed by Schubert (1976) is

$$\frac{k}{z_B} \int_0^{z_B} \overline{w' s_V'} dz + \frac{1}{2} (1-k) (\overline{w' s_V'})_{\min} = 0 \quad 0 \leq k \leq 1, \quad (2.16)$$

where k is the entrainment parameter and $\overline{w' s_V'}$ is the virtual dry static energy flux. $k=1$ corresponds to Lilly's maximum entrainment condition and $k=0$ corresponds to his minimum entrainment condition.

Including the effects of both vapor and liquid water on buoyancy, virtual dry static energy is defined

$$s_V = s + \epsilon L (\delta q - \ell). \quad (2.17)$$

Letting $L \overline{w' q'} = \frac{\gamma}{\gamma+1} \overline{w' h'}$ when $z_C < z < z_B$, the turbulent virtual dry static energy flux can be expressed as

$$\overline{w' s_V'} = \begin{cases} \beta \overline{w' h'} - \epsilon L \overline{w' (q'+\ell')} & z_C < z < z_B \\ \overline{w' h'} - (1 - \epsilon \delta) L \overline{w' q'} & 0 \leq z < z_C. \end{cases} \quad (2.18)$$

The remaining variables in (2.15), (2.17), and (2.18) are given by

$$b = \frac{g}{c_p} \left(\frac{\partial q^*}{\partial T} \right)_p + g \left(\frac{\partial q^*}{\partial p} \right)_T, \quad \gamma = \frac{L}{c_p} \left(\frac{\partial q^*}{\partial T} \right)_p, \quad (2.19)$$

$$\delta = 0.608, \quad \epsilon = \frac{c_p T_S}{L}, \quad \beta = \frac{1 + \gamma \epsilon (\delta+1)}{1+\gamma}.$$

Carrying out the integration in (2.16) gives

$$\begin{aligned}
& \beta + (1-\beta) \frac{z_C^2}{z_B^2} (\overline{w'h'})_B + \beta + (1-\beta) \frac{z_C}{z_B} \left(2 - \frac{z_C}{z_B}\right) (\overline{w'h'})_S \\
& - \epsilon + (1-\epsilon(\delta+1)) \frac{z_C^2}{z_B^2} L\overline{w'(q'+\ell')}_{B} - \epsilon + (1-\epsilon(\delta+1)) \frac{z_C}{z_B} \left(2 - \frac{z_C}{z_B}\right) L(\overline{w'q'})_S \\
& + \frac{1-k}{k} \min \left\{ \begin{array}{l} \beta(\overline{w'h'})_B - \epsilon L\overline{w'(q'+\ell')}_{B} \\ \left[\left(1 - \frac{z_C}{z_B}\right) (\overline{w'h'})_S + \frac{z_C}{z_B} (\overline{w'h'})_B \right] (1-\epsilon\delta) L \left[\left(1 - \frac{z_C}{z_B}\right) (\overline{w'q'})_S + \frac{z_C}{z_B} \overline{w'(q'+\ell')}_{B} \right] \\ (\overline{w'h'})_S - (1-\epsilon\delta) L(\overline{w'q'})_S \end{array} \right\} = 0. \tag{2.20}
\end{aligned}$$

$\overline{w's_V'}$ is linear in both the subcloud and cloud layers, with a positive jump across cloud base. Therefore, $(\overline{w's_V'})_{\min}$ must occur at cloud top, just below cloud base, or at the surface; these possibilities are indicated in (2.20).

Equations (2.1), (2.2), (2.7), (2.8), (2.9), (2.14), (2.15) and (2.20) form a closed set of eight equations in the eight unknowns, z_B , z_C , h_M , $(q+\ell)_M$, $(\overline{w'h'})_S$, $(\overline{w'h'})_B$, $(\overline{w'q'})_S$ and $\overline{w'(q'+\ell')}_{B}$.

3.0 PROCEDURE

3.1 Summary of the Governing Equations

The following is a list of the equations needed to compute the model's outputs:

$$(\overline{w'h'})_S = C_T V [h_S^* - h_M] \quad (3.1)$$

$$(\overline{w'q'})_S = C_T V [q_S^* - (q+l)_M] \quad (3.2)$$

$$\frac{z_C}{H} = \frac{(1+\gamma) [q_S^* - (q+l)_M] - \frac{\gamma}{L} [h_S^* - h_M]}{b} \quad (3.3)$$

$$\Delta h = h_0 + \frac{\partial h}{\partial z} z_B - h_M \quad (3.4)$$

$$\Delta(q+l) = q_0 + \frac{\partial q}{\partial z} z_B - (q+l)_M \quad (3.5)$$

$$T(z_B^-) = \frac{1}{c_p} [h_M - L(q+l)_M + \frac{L}{1+\gamma} \frac{b}{H} (z_B - z_C) - g z_B] \quad (3.6)$$

$$\Delta F_R = \sigma T^4(z_B^-) - F_L^+(z_B^+) + \Delta F_S \quad (3.7)$$

$$\begin{pmatrix} a_{11} & a_{12} \\ a_{21} & a_{22} \end{pmatrix} \begin{pmatrix} (\overline{w'h'})_B \\ (\overline{w'(q+l')})_B \end{pmatrix} = \begin{pmatrix} b_1 \\ b_2 \end{pmatrix} \quad (3.8)$$

$$\frac{\partial h_M}{\partial t} + V \frac{\partial h_M}{\partial x} = \frac{[(\overline{w'h'})_S - (\overline{w'h'})_B]}{z_B} \quad (3.10)$$

$$\frac{\partial (q+l)_M}{\partial t} + V \frac{\partial (q+l)_M}{\partial x} = \frac{[\overline{w'(q+l')})_S - \overline{w'(q+l')})_B]}{z_B} \quad (3.11)$$

$$\frac{\partial z_B}{\partial t} + V \frac{\partial z_B}{\partial x} = -D z_B + \frac{\Delta F_R}{\rho} - \frac{(\overline{w'h'})_B}{\Delta h} \quad (3.12)$$

These equations are solved in the following order:

- (1) Compute the surface fluxes from (3.1) and (3.2),
- (2) Compute cloud base from (3.3).
- (3) Compute the cloud top jumps in h and $q+\ell$ from (3.4) and (3.5).
- (4) Using (3.6), compute the cloud top jump in net radiation flux from (3.7).
- (5) Solve the two by two system (3.8) and (3.9) for $\overline{(w'h^T)}_B$ and $\overline{(w'(q'+\ell'))}_B$.
- (6) Predict h_M , $(q+\ell)_M$ and z_B from (3.10), (3.11) and (3.12).

To perform these calculations, we need the constants R , c_p , L , C_T , g , σ , an entrainment parameter k , and a reference temperature and pressure from which to compute H , ρ , ϵ , γ , β and b . In addition to these, the input parameters required for this procedure are wind speed V , sea surface temperature T_S , sea surface saturation mixing ratio and moist static energy q_S^* and h_S^* , the temperature and moisture structure above the mixed layer (i.e., h_0 , $\frac{\partial h}{\partial z}$, q_0 , $\frac{\partial q}{\partial z}$), the downward longwave flux just above cloud top, $F_{L\downarrow}(z_B^+)$, the cloud top jump in short wave flux, ΔF_S , and the large-scale divergence, D . The input parameters are discussed in section 3.2, and the calculation of trajectories along which solutions to the equations are computed is discussed in section 3.3.

Of steps 1-6 above, only step 5 is not straightforward. In order to determine the correct coefficient matrix and inhomogeneous terms to use in the system (3.8) and (3.9), it is necessary to find where $\overline{(w's_V^T)}_{\min}$ occurs. To do this, we assume $\overline{(w's_V^T)}_{\min}$ is at one of the three possible places (at cloud top, just below cloud base, or at the surface) to obtain coefficients for the fluxes at cloud top from (2.20).

Then solving (3.8) and (3.9) simultaneously, and using (2.5), (2.6), and (2.18) to calculate $\overline{w's_y'}$ at all three points, we can check our assumption. Stepping through this procedure three times assuming the minimum at a different point each time, we can determine where the minimum occurs and whether it is unique. Equations (3.10), (3.11), and (3.12) were solved for the steady state case, that is, $\frac{\partial}{\partial t} = 0$, using the fourth order Runge-Kutta scheme.

3.2 Input Parameters

The sea surface temperature data were monthly averages tabulated by Washington and Thiel (1970) on a 2.5° square grid mesh. For the wind velocity field, we used data compiled by Wyrтки and Meyers (1975) on a 2° latitude by 10° longitude grid mesh, and interpolated it onto a 2.5° grid mesh. q_S^* and h_S^* are calculated from the sea surface temperature field and a surface pressure of 102 kPa, and the large-scale divergence was calculated from the wind velocity. In order to compute H , ρ , γ , ϵ , β , and b , we used the sea surface temperature as the reference temperature. The constants used were $R = 287 \text{ J}/(\text{kg}^\circ\text{K})$, $c_p = 1004.5 \text{ J}/(\text{kg}^\circ\text{K})$, $L = 2.453 \times 10^6 \text{ J}/\text{kg}$, $C_T = .0015$, $g = 9.8 \text{ m}/\text{sec}^2$, and $\sigma = 5.673 \times 10^{-8} \text{ J}/(\text{m}^2\text{sec}^\circ\text{K}^4)$. All calculations were done for an entrainment parameter of $k = 0.2$. Although this parameter actually may be a function of some of the other input variables, Schubert (1976) has shown that varying it between 0.1 and 0.3, which are probably reasonable bounds, makes little difference in the results.

The model requires $h(z_B(x)^+)$ and $q(z_B(x)^+)$ in order to compute Δh and $\Delta(q+\epsilon)$. For this we used averaged 00Z July and August temperature and moisture data supplied by R. Jenne for the stations Guayaquil (2.15°S , 79.88°W), Lima (12.02°S , 77.13°W), and Antofagasta (23.42°S , 70.47°W).

The data had at least 5 kPa resolution and were one month averages for the years 1958 for Guayaquil and 1967 for Lima and Antofagasta (Figure 3.1). To eliminate the low level inversion and marine layer apparent in the soundings for Lima and Antofagasta, we extrapolated lines of T and q to the surface. The reason for this is that we need T and q above our computed mixed layer. From this modified data we obtained

$$h = \frac{\partial h}{\partial z} z + h_0 ,$$

$$q = \frac{\partial q}{\partial z} z + q_0 .$$

Using linear interpolation, we derived a latitudinal dependence for $\frac{\partial h}{\partial z}$, h_0 , $\frac{\partial q}{\partial z}$, and q_0 . Figure 3.2 shows the s, h, and h* profiles, both actual and modified, for the three stations. The higher h values at Guayaquil above the stable layers of the other two stations are accounted for mainly by Guayaquil's greater moisture.

It is revealing to compare the temperature and moisture profiles for Guayaquil, Lima, and Antofagasta. Since Guayaquil is near the equator, it just borders the edge of the stratocumulus regime as shown in Figure 1.1. Consequently, it doesn't come under the strong subsidence of the descending Hadley cell as do Lima and Antofagasta, and there is no strong inversion at Guayaquil as there is at the other two stations. Also, the air is not as close to being saturated in the lower levels at Guayaquil. That these features show up in one month averages at Lima and Antofagasta demonstrates the persistence of the stratocumulus clouds there during July and August.

As we expect, Guayaquil is warmer than the other two stations at levels below their stable layers. In contrast, Lima and Antofagasta are

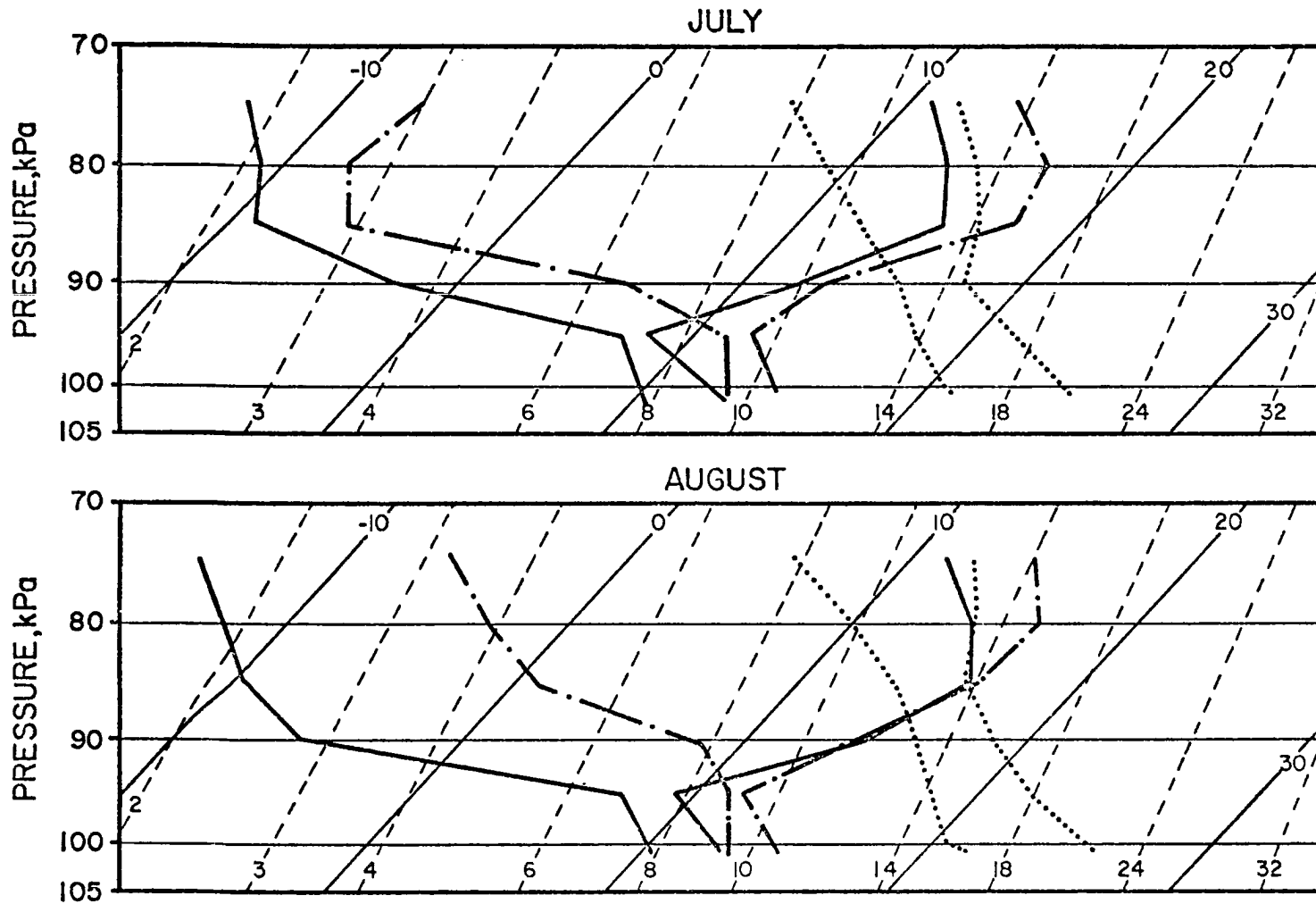


Figure 3.1 One month averaged 00Z July and August temperature and mixing ratio profiles for the stations Guayaquil (2.15°S, 79.88°W), indicated by the dotted lines, Lima (12.02°S, 77.13°W), indicated by the dash-dot lines, and Antofagasta (23.42°S, 70.47°W), indicated by the solid lines.

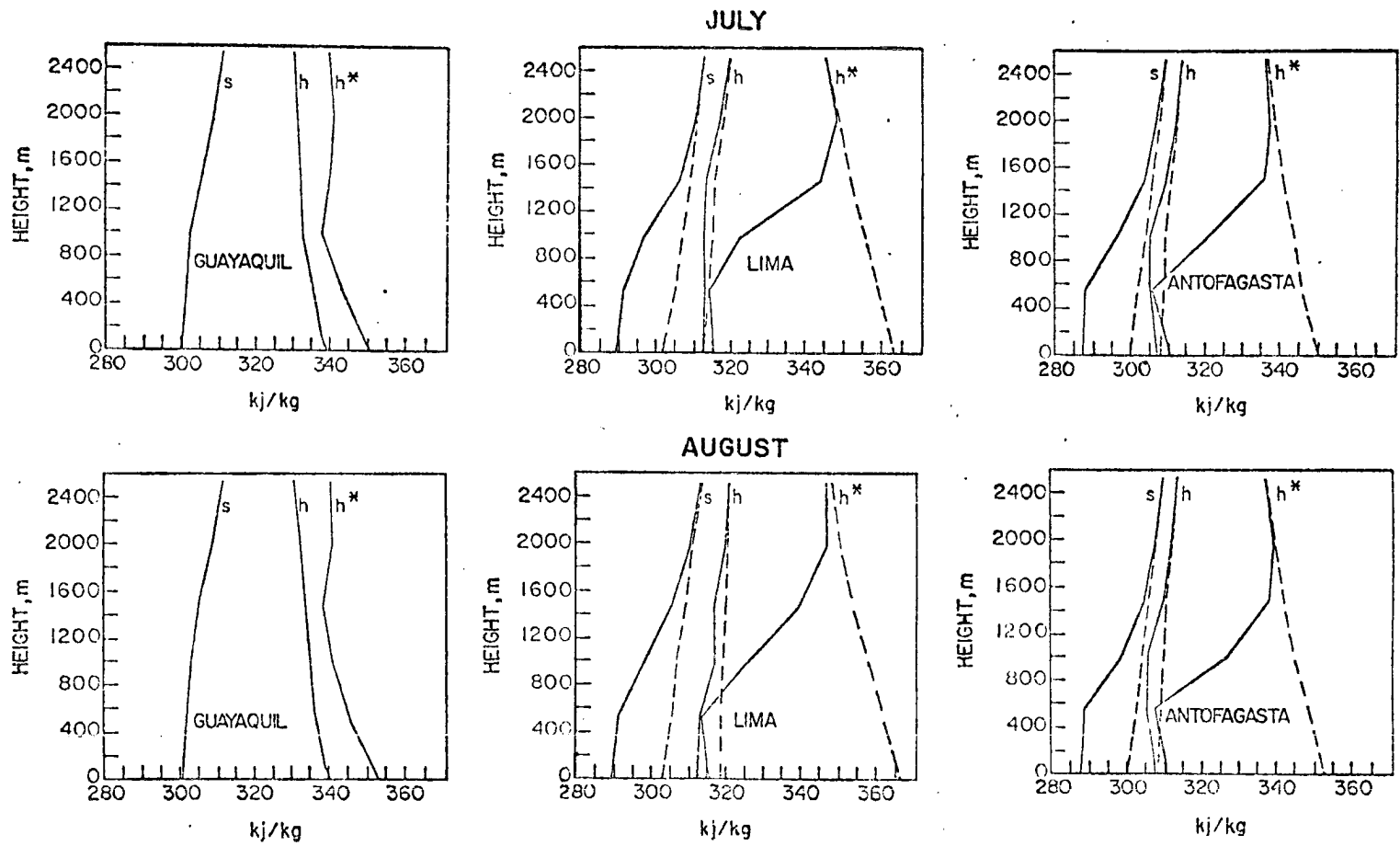


Figure 3.2 July and August dry static energy, s , moist static energy, h , and saturation moist static energy, h^* , profiles for Guayaquil, Lima, and Antofagasta. Dashed lines indicate the extrapolated values.

relatively close in temperature and moisture although they are approximately 10° latitude apart, as are Guayaquil and Lima. Note also the strong drying out of the air above the mixed layers at Lima and Antofagasta; such drying is absent at Guayaquil. For all three stations, there are only slight differences in temperature and moisture from July to August.

The model also requires

$$\Delta F_R = \Delta F_L + \Delta F_S = \sigma T^4(z_B^-) - F_{L\downarrow}(z_B^+) + \Delta F_S. \quad (3.13)$$

$\sigma T^4(z_B^-)$ is computed using the temperature determined from (3.6). To find $F_{L\downarrow}(z_B^+)$, we used a longwave radiation model devised by Cox (1973) and Cox et al. (1976). The input parameters for this model were the modified T and q profiles for Guayaquil, Lima, and Antofagasta, as well as a carbon dioxide mixing ratio value of 0.486 gm/kg and an ozone mixing ratio value of 0.0μ gm/kg, which were prescribed for lack of other information. The $F_{L\downarrow}$ profiles for the three stations are shown in Figure 3.3. As for h and q, we found $F_{L\downarrow} = \frac{\partial F_{L\downarrow}}{\partial z} z + (F_{L\downarrow})_0$ for each station, and used linear interpolation to determine latitudinal dependence for $\frac{\partial F_{L\downarrow}}{\partial z}$ and $(F_{L\downarrow})_0$.

We chose to neglect any latitudinal or z dependence of ΔF_S because the variations of that term are so small compared to the others. Instead, we used another of Cox's models which gave us the daily integrated shortwave radiation throughout the atmosphere for the days July 15 and August 15. The input parameters were the same as those for the longwave case. We assumed 7% absorption by the cloud (Neiburger, 1949) at an estimated cloud top height of 80 kPa for

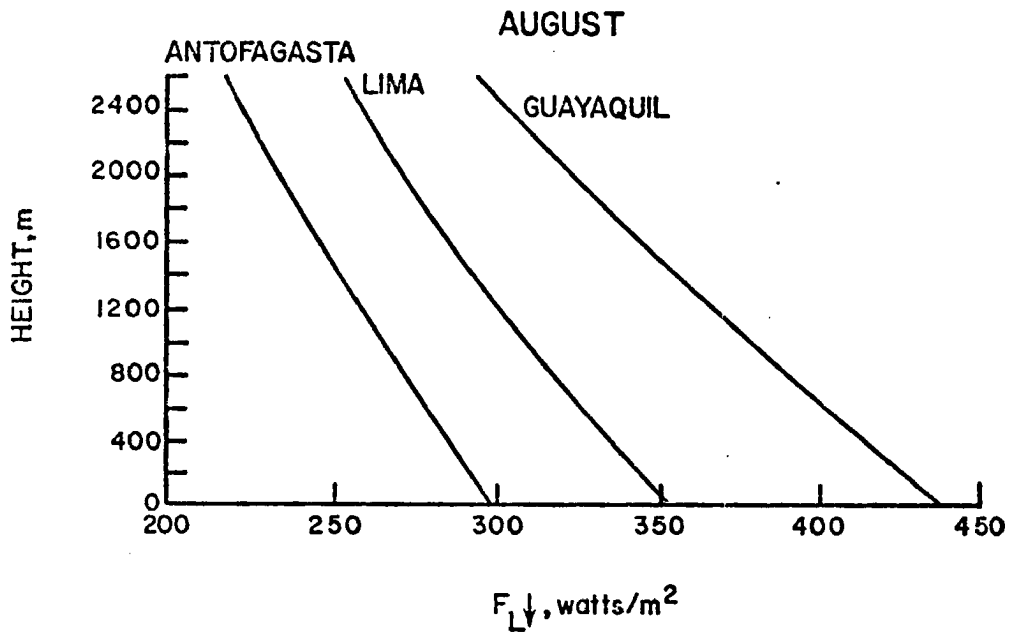
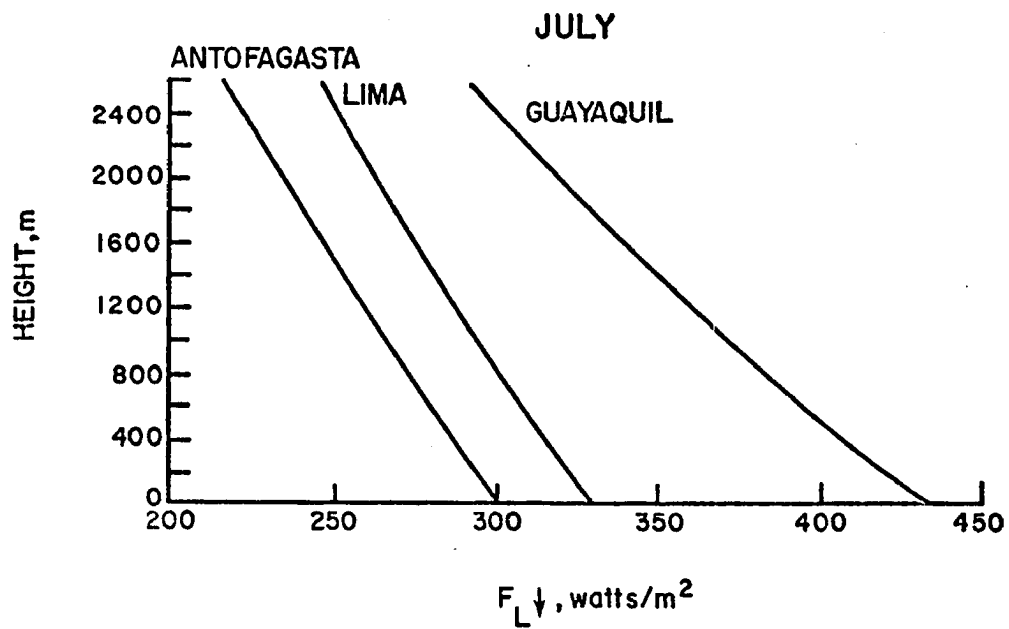
DOWNWARD LONGWAVE
RADIATIVE FLUX

Figure 3.3 July and August downward longwave radiative flux for Guayaquil, Lima, and Antofagasta.

Guayaquil and 86 kPa for Lima and Antofagasta and averaged the result for the three stations. Thus, we found the daily averaged shortwave absorption at cloud top to be 17.8 watts/m² in July and 19.8 watts/m² in August.

3.3 Trajectory Calculation

Given an initial latitude and longitude, a downstream distance increment, and a wind field, it is possible to compute a trajectory and determine the time elapsed between points traveled along it. Figure 3.4 illustrates this procedure. Suppose from an initial latitude and longitude (ϕ_i, λ_i) we move an increment d in direction α , which is the direction towards which the wind is blowing, to a new latitude and longitude $(\phi_{i+1}, \lambda_{i+1})$. The three great circles connecting the pairs of points (ϕ_i, λ_i) and $(\phi_{i+1}, \lambda_{i+1})$, the north pole and (ϕ_i, λ_i) , and the north pole and $(\phi_{i+1}, \lambda_{i+1})$ form the sides of a spherical triangle given by $\frac{d}{a}$, $\frac{\pi}{2} - \phi_i$, and $\frac{\pi}{2} - \phi_{i+1}$, respectively, where a is the radius of the earth. The cosine law for sides states that the cosine of a side of a spherical triangle is equal to the product of the cosines of the other two sides plus the product of the sines of those two sides multiplied by the cosine of their included angle. Applying the cosine law to side $\frac{\pi}{2} - \phi_{i+1}$ we obtain

$$\sin \phi_{i+1} = \sin \phi_i \cos\left(\frac{d}{a}\right) + \cos \phi_i \sin\left(\frac{d}{a}\right) \cos \alpha. \quad (3.14)$$

Applying the cosine law to side $\frac{d}{a}$ we obtain

$$\cos \frac{d}{a} = \sin \phi_i \sin \phi_{i+1} + \cos \phi_i \cos \phi_{i+1} \cos(\lambda_i - \lambda_{i+1}), \quad (3.15)$$

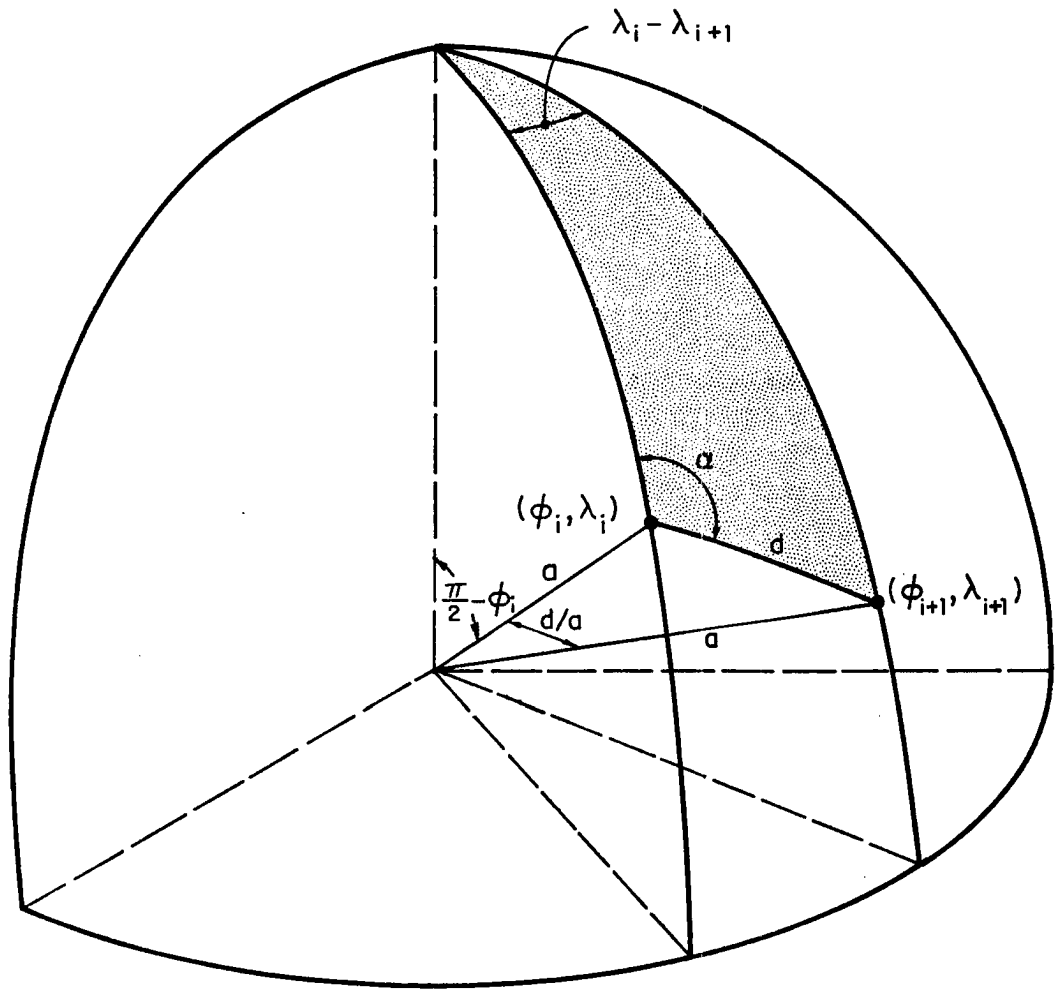


Figure 3.4 Method used for the trajectory computation. (See explanation in text.)

which can be written

$$\cos(\lambda_i - \lambda_{i+1}) = \frac{\cos(\frac{d}{a}) - \sin\phi_i \sin\phi_{i+1}}{\cos\phi_i \cos\phi_{i+1}}. \quad (3.16)$$

The time elapsed in traveling distance d is

$$t_{i+1} - t_i = \frac{d}{V_i}, \quad (3.17)$$

where V_i is the wind speed at (ϕ_i, λ_i) . Thus, using (3.14), (3.16), and (3.17), we can compute the latitude and longitude of successive downstream points and the time increment between each point.

In the manner described, we can see how air is modified as it moves equatorward over the two dimensional fields of T_S , V , and D described in section 3.2. Since we examine only steady state solutions, $\frac{d}{dt} = V \frac{\partial}{\partial x}$, where the positive x -direction is the direction downstream along a trajectory in a natural coordinate system. Therefore, "time" and "downstream distance" are interchangeable in our terminology, and we have chosen to specify the distance, moving 6 km downstream at each step and computing the time increment from (3.17).

To insure against the possibility of our having chosen poor initial conditions for z_B , h_M , or $(q+\epsilon)_M$, we allow the model to reach a horizontally homogeneous steady state before doing any calculations along trajectories. Therefore, we run the model "in place" for 1501 time steps, which is many days of simulated time. Mathematically, that is simply letting $V \frac{\partial}{\partial x} = 0$ and $\frac{d}{dt} = \frac{\partial}{\partial t} \neq 0$.

Between 40 and 50 trajectories were calculated for each of the four cases discussed. Values along the trajectories were interpolated onto 0.5° square grids so that they could be contoured. All trajectories

were begun on the eastern or southern edge of the field bounded by 75°W and 100°W and by 2.5°S and 27.5°S, using an initial divergence of $4.5 \times 10^{-6} \text{ sec}^{-1}$. This initial divergence affects the steady state values the model reaches. It was chosen because it yielded fairly reasonable results, considering the absence of data with which to compare them, whereas allowing the model to stabilize using the small computed divergence for those regions resulted in cloud tops that were far too high. We must emphasize, therefore, that the contour fields presented in Chapter 4, particularly the cloud height and depth fields, express relative rather than absolute values. Experiments were done changing the initial divergence to show that the same relationship exists between the contours though their numerical values may differ. In section 4.4, we discuss the July case using an initial divergence of $3.0 \times 10^{-6} \text{ sec}^{-1}$.

4.0 RESULTS

4.1 Results of the July Case

The movement along the trajectories over the input fields of T_S , V , and D are shown in Figure 4.1. The South American coast is in the upper right hand corner. Because of the northerly component of the wind, no trajectory could be started at 27.5°S west of 95°W . Thus, there is no data in the southwestern corner of the field. That area is denoted by a dashed line along the westernmost trajectory.

The z_B field (Figure 4.2a) clearly depends upon the divergence more than any of the other input variables. The convergence and high cloud tops just off the coast are indications of the ITCZ rather than stratocumulus. The low of 1000 m in the z_B field centered at 77.5°W , 15°S is shifted just north of a region of high divergence, while the rapid increase of z_B towards the west in the lower half of the field corresponds to a region of low divergence. z_B , however, is also linked to the $\rho(\overline{w'h'})_B$, ΔF_R , and Δh fields (Figures 4.5b, 4.10a and 4.10b), and a comparison with those yields interesting and unexpected results. From (3.12), we see that $V \frac{\partial z_B}{\partial x}$ is inversely proportional to Δh , yet the feedback of z_B into Δh is such that Δh becomes high off the coast and towards the southeast in the same regions where z_B becomes high, and Δh is low where z_B is low. Evidently the divergence field and the $(\overline{w'h'})_B$ and $\frac{\Delta F_R}{\rho}$ fields are of sufficient magnitude to counteract this. Another interesting feature is that Δh becomes negative in the middle of the field. Along the zero lines of Δh , z_B mathematically becomes infinitely large unless $\frac{\Delta F_R}{\rho} - (\overline{w'h'})_B$ also vanishes. We find that

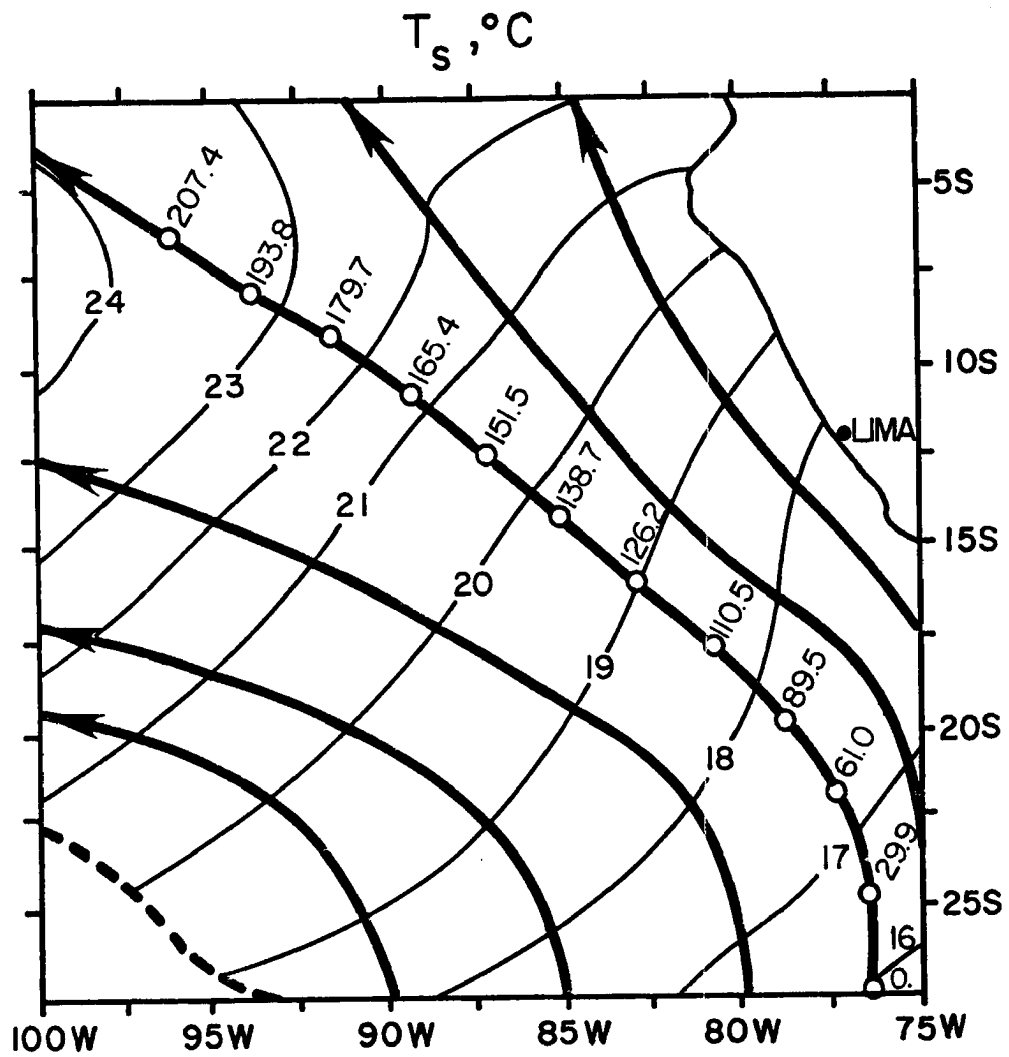


Figure 4.1a July input variable of sea surface temperature. Heavy lines indicate trajectories. The trajectory beginning at 76.5°W , 27.5°S is marked every 300 km with the time in hours from initialization.

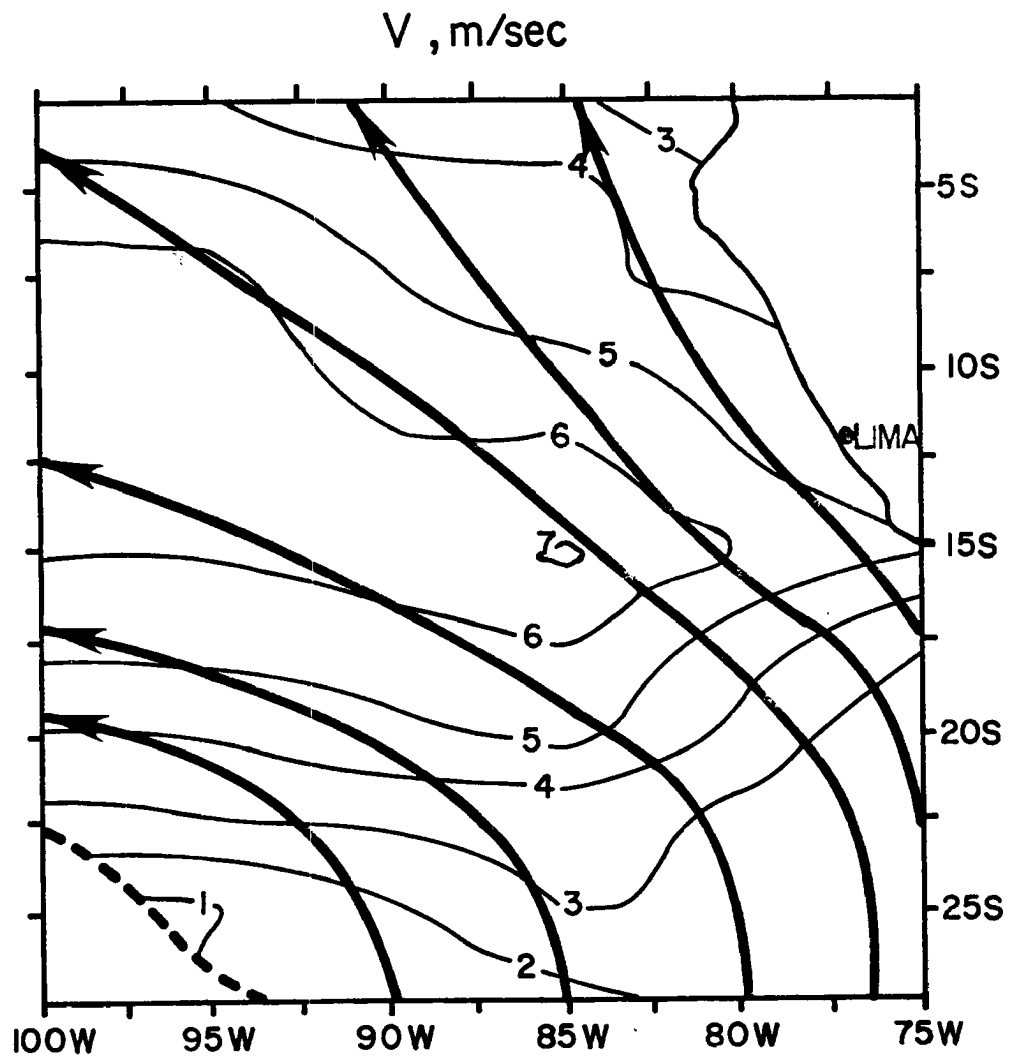


Figure 4.1b July input variable of surface wind speed.
Heavy lines indicate trajectories.

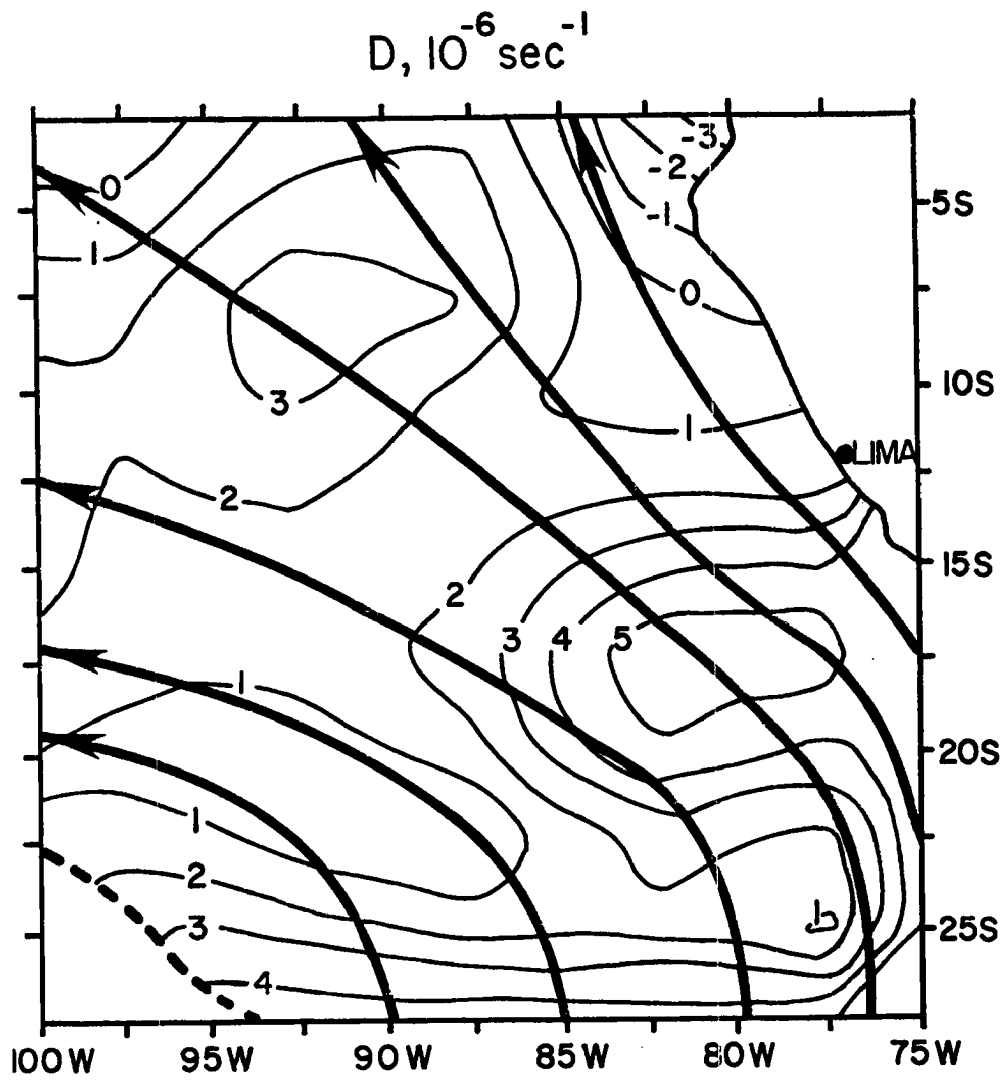


Figure 4.1c July input variable of large-scale divergence. Heavy lines indicate trajectories.

the model can handle the transition from Δh positive to negative, and the z_B field remains smooth. A negative Δh at cloud top is characteristic of the trade cumulus regime. z_B continues to increase in the portion of the field where Δh is negative. Therefore, $\frac{\Delta F_R}{\rho} - (\overline{w'h'})_B$ must become negative. If it did not, a negative mass flux at cloud top would be implied, as would be a negative $\overline{w'(q'+\ell')}_B$ from (3.9). Those situations are physically impossible, and a comparison of Figures 4.10b and 4.11a shows the model does produce an exact correspondence between the negative regions of Δh and the negative regions of $\Delta F_R - \rho(\overline{w'h'})_B$. ΔF_R itself decreases northward as $F_{L+(z_B^+)}$ increases. The actual mass flux into the layer, given by $\rho(\frac{dz_B}{dt} - w_B)$, is shown in Figure 4.11b. That field increases to the west.

z_C will sink as the mixed layer cools or moistens. Figure 4.2b shows z_C decreases to the north. Since T_S increases to the northwest, the decrease of z_C is primarily caused by the rising equatorward values of $(q+\ell)_M$ (Figure 4.3b). z_C decreases most rapidly in the bottom half of the field where the gradient of $(q+\ell)_M$ is also slightly stronger.

The depth of the cloud layer, $z_B - z_C$, (Figure 4.2c) follows very closely the contours of z_B and thus is equally dependent upon the divergence. The minimum cloud depth to the east is nearly coincident with the minimum z_B , and $z_B - z_C$ increases most rapidly towards the west in the lower half of the field as does z_B . Lilly has estimated that a cloud 125 m to 150 m thick can be considered a blackbody. Since $z_B - z_C$ is nearly always thicker than that, our estimation of blackbody radiation has been valid (allowing that that assumption has not "forced" the condition).

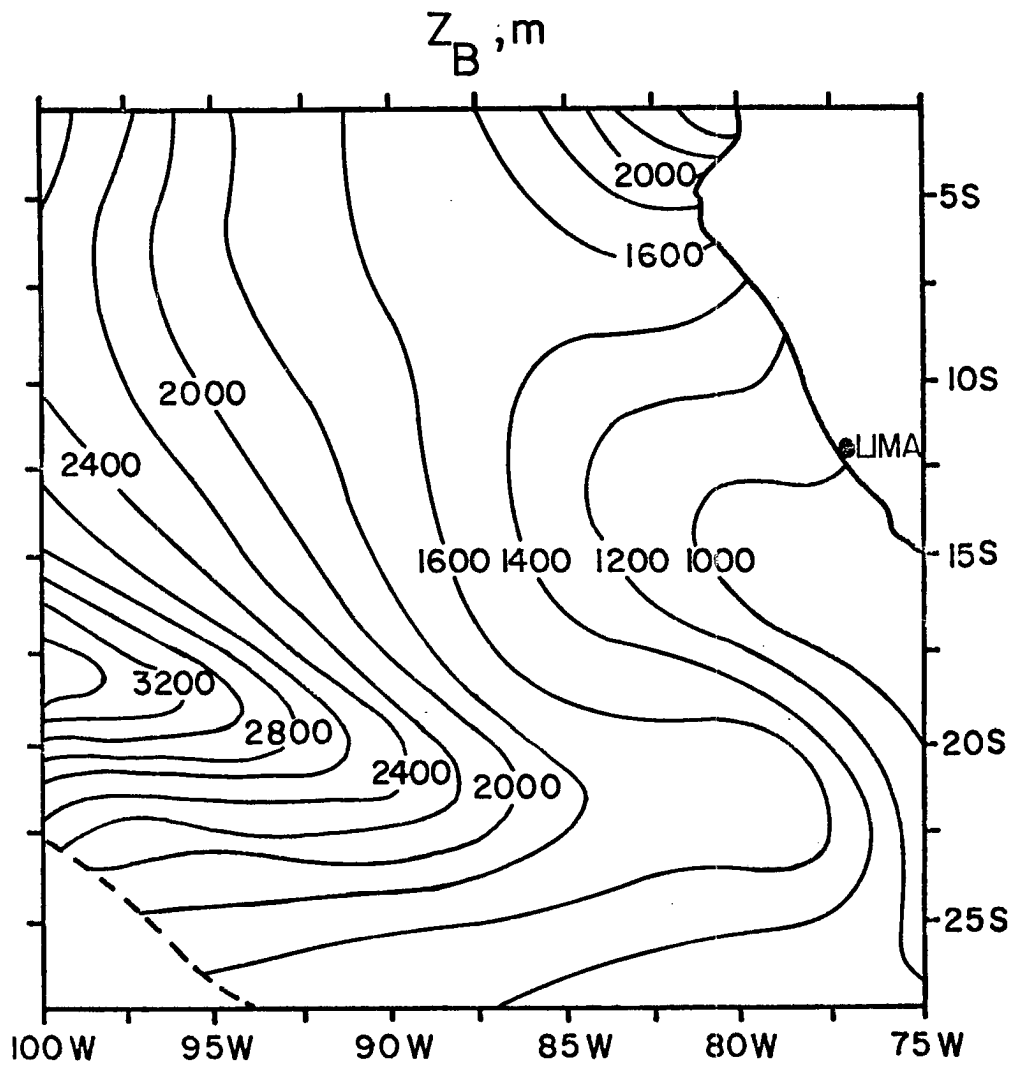


Figure 4.2a July cloud top.

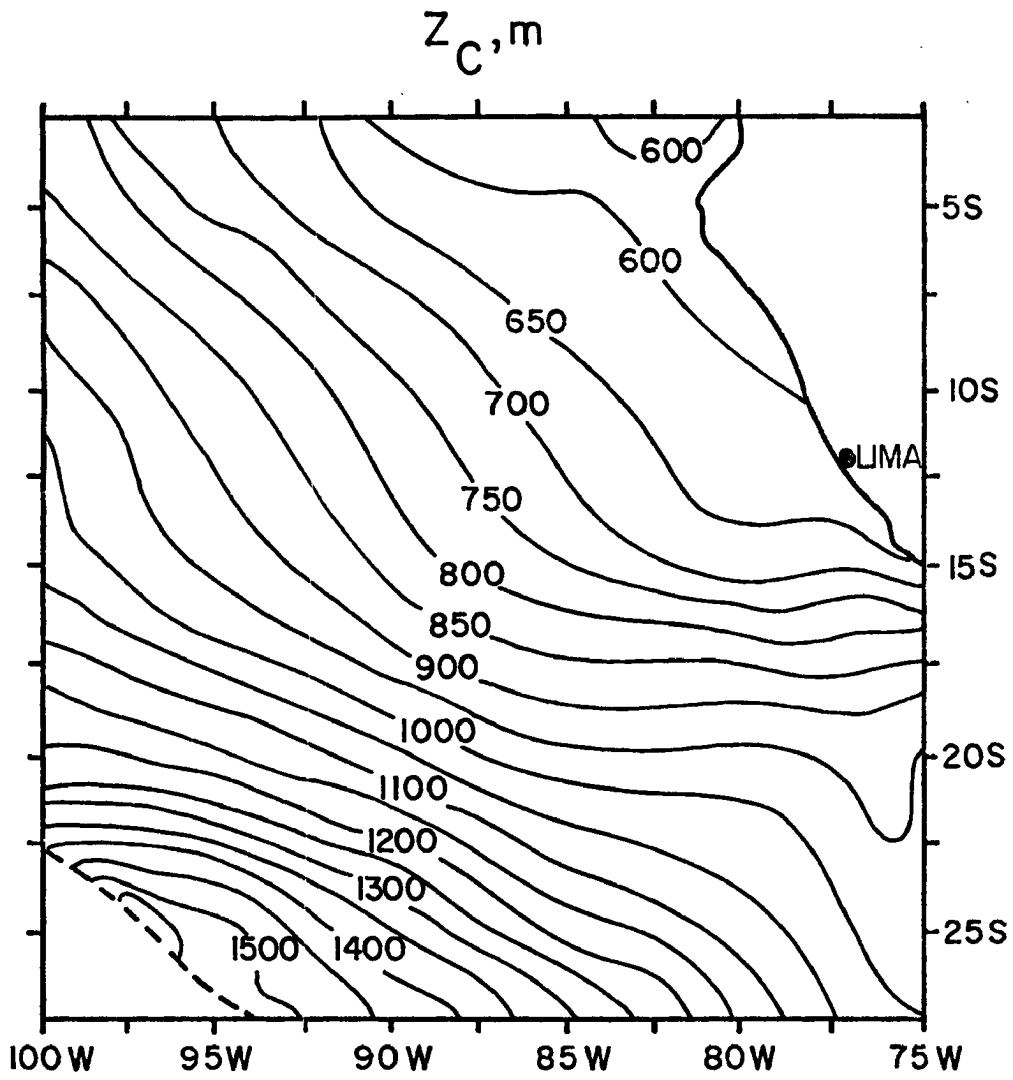


Figure 4.2b July cloud base.

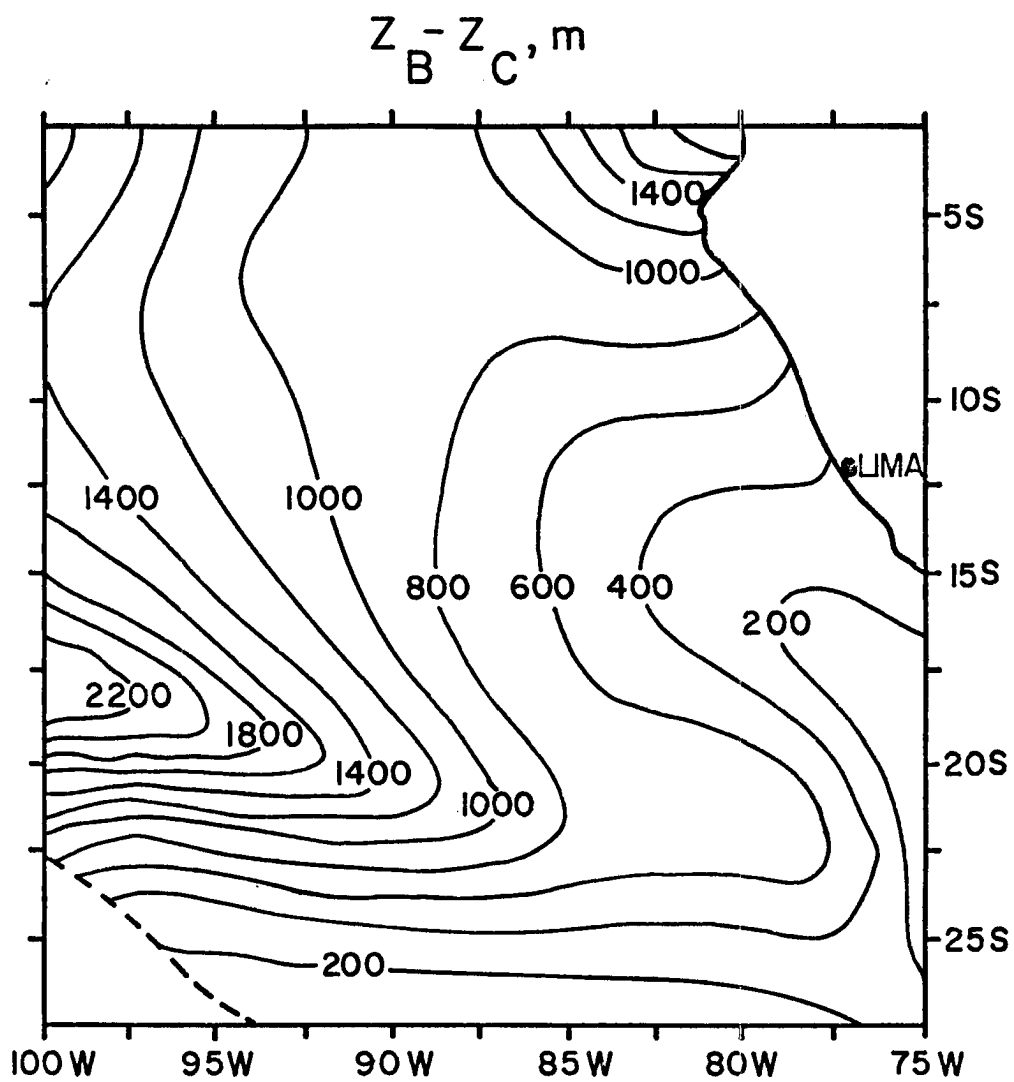


Figure 4.2c July depth of the cloud layer.

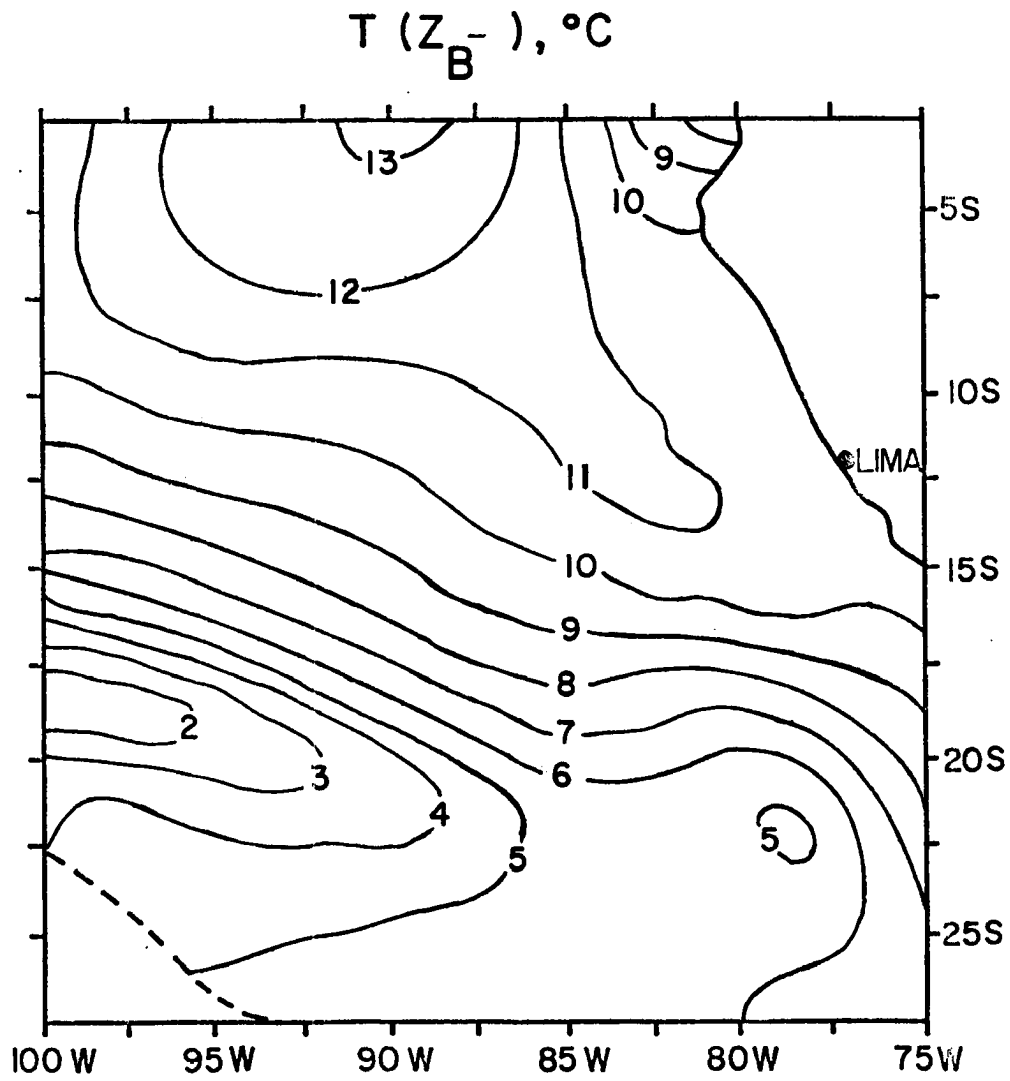


Figure 4.2d July cloud top temperature.

The increases of h_M (Figure 4.3a) and $(q+l)_M$ towards the equator can be compared to T_S . h_M has a northwestward gradient while $(q+l)_M$ has an almost northward gradient. Thus, h_M in particular reflects the warmer water towards the northwest. In the model equations, h_M and $(q+l)_M$ are independent variables which differ by a third variable, $(s-L\ell)_M = h_M - L(q+l)_M$, where s represents the dry static energy ($=c_p T + gz$). Since any two of these variables is sufficient to uniquely determine the third, a plot of $(s - L\ell)_M$ was not included. That field, however, was found to increase very slowly towards the northwest, indicating that h_M increases slightly faster than $L(q+l)_M$, or that there is a slight increase of temperature in the mixed layer towards the northwest. That increase is not strong enough to insure an increase in z_C .

Our temperature data do not have enough resolution to show the mesoscale features of cold water upwelling along the coast, but as we have seen, the equatorward movement along the trajectories takes the air over increasingly warmer water. This advection over warmer water can be seen in the sequence of vertical profiles of $\rho \overline{w'h'}$ and $L\rho \overline{w'(q'+l')}$ (Figures 4.4 and 4.5). These profiles were plotted every 300 km along the trajectory beginning at $76.5^\circ W$, $27.5^\circ S$ as indicated by the small circles in Figure 4.1c, and labelled with the time in hours from initialization. At the initial time are the horizontally homogeneous steady state profiles with $\rho \overline{w'h'}_S = \rho \overline{w'h'}_B$ and $L\rho \overline{w'(q'+l')}_S = L\rho \overline{w'(q'+l')}_B$. The turbulent fluxes jump to zero at z_B^+ . As the air moves equatorward, the fluxes at the surface exceed the fluxes at the top of the layer, resulting in a convergence of h and $(q+l)$ in the mixed layer. That convergence is directly responsible for the equatorward increase in h_M and $(q+l)_M$.

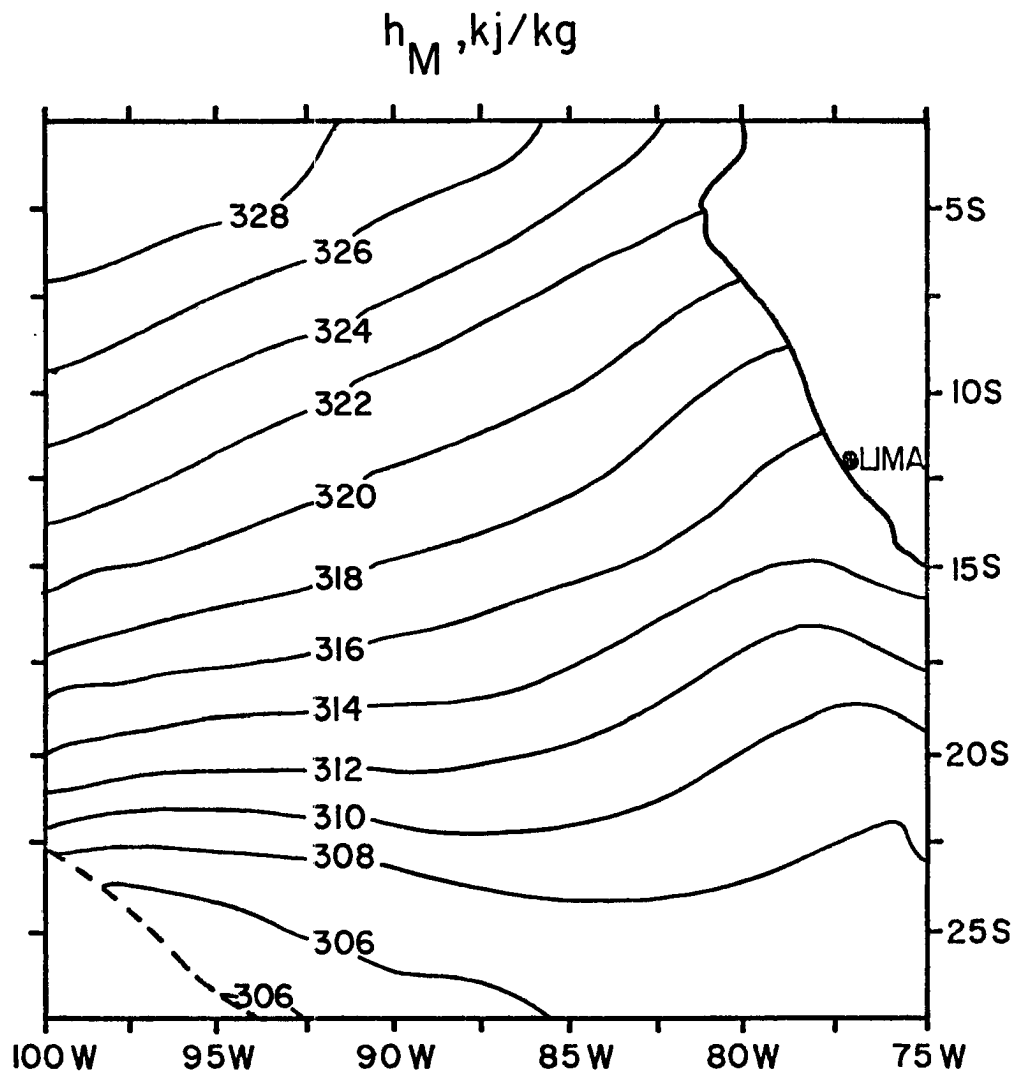


Figure 4.3a July mixed layer moist static energy.

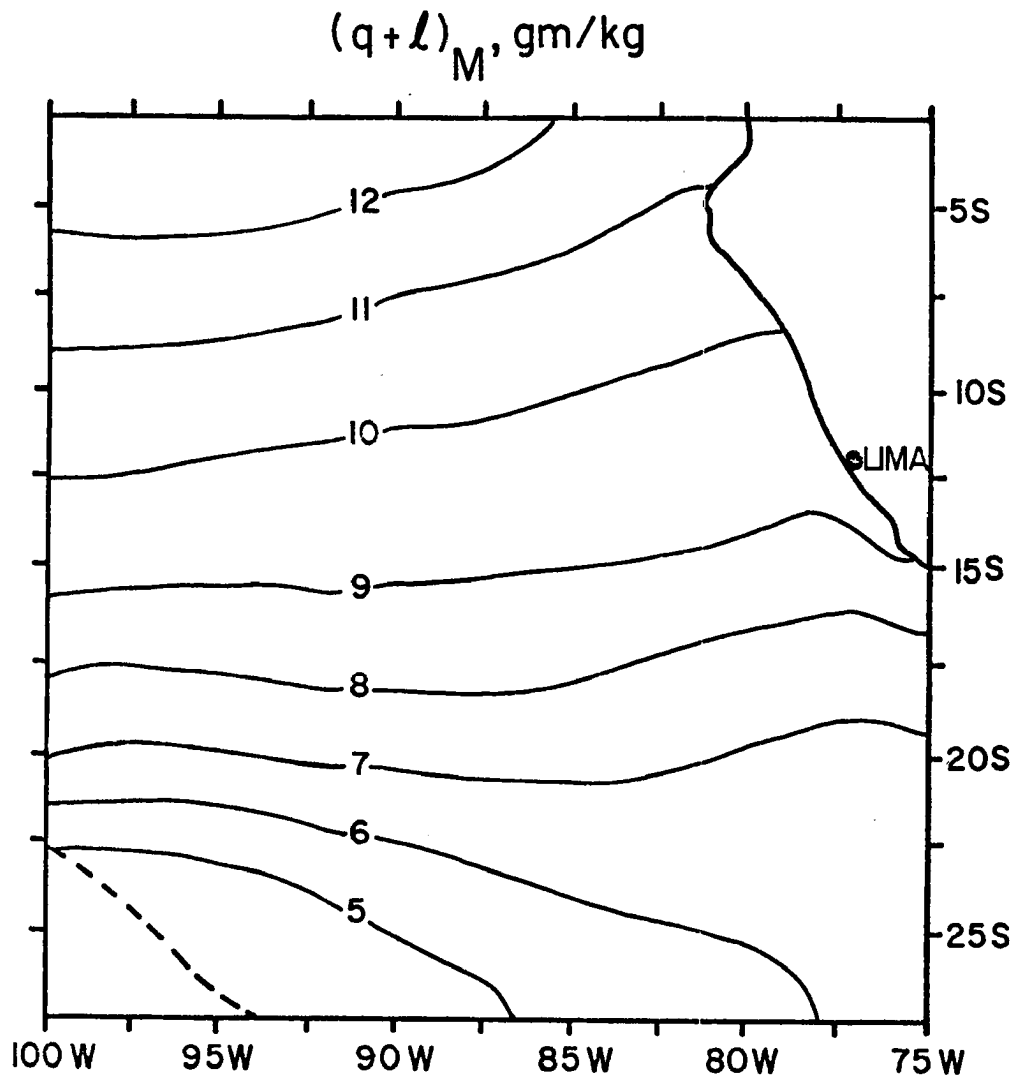


Figure 4.3b July mixed layer total water mixing ratio.

JULY

$$\rho \overline{w' h'}$$
, watts/m²

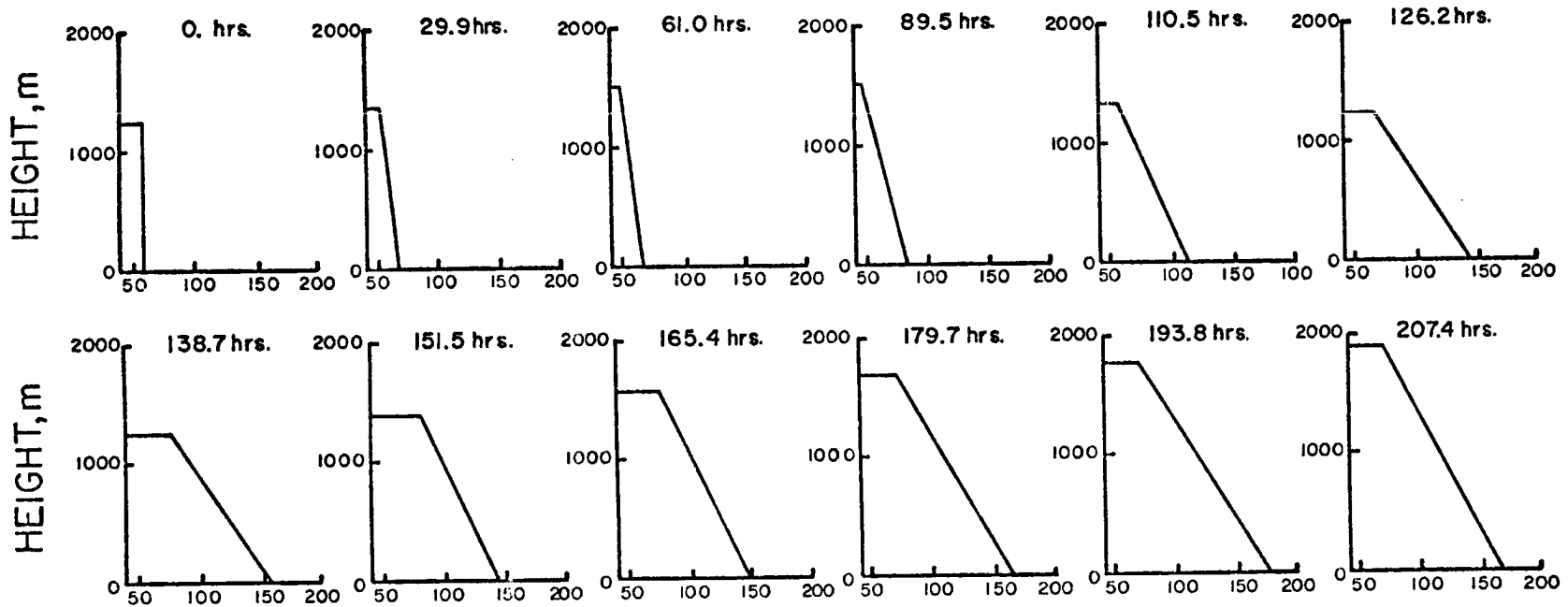


Figure 4.4 July vertical profiles of the turbulent moist static energy flux every 300 km along the trajectory beginning at 76.5°W, 27.5°S. Time in hours from initial-ization is indicated.

JULY

$$L\rho \overline{w'(q'+\ell')}, \text{ watts/m}^2$$

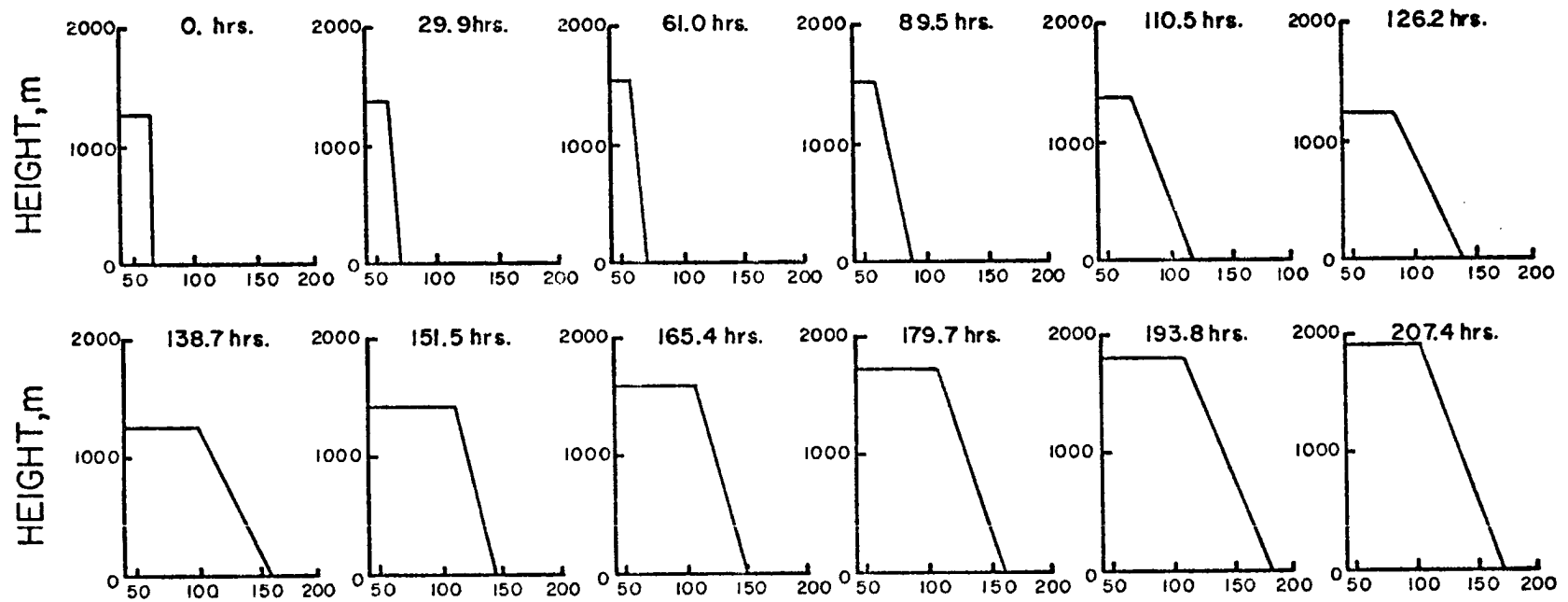


Figure 4.5 July vertical profiles of the turbulent flux of total water every 300 km along the trajectory beginning at 76.5°W, 27.5°S. Time in hours from initialization is indicated.

The $(\overline{w'h'})_S$ and $L\rho\overline{w'(q'+l')}$ fields (Figures 4.6a and 4.7a) are extremely similar; the only difference is that $L\rho\overline{w'(q'+l')}$ is slightly higher in most places. Since, by definition, $\overline{w'h'} = c_p \overline{w'T'} + L\overline{w'q'}$, and since $L\overline{w'l'}$ is zero at the surface, a small negative sensible heat flux is implied throughout most of the field. Figure 4.12, which shows $T_S - T_{\text{air at surface}}$, supports that conclusion ($T_{\text{air at surface}} = (h_M - L(q+l)_M)/c_p$). Both $\rho(\overline{w'h'})_S$ and $L\rho\overline{w'(q'+l')}$ are very well correlated with the V field.

Vertical profiles of $\rho\overline{w's_V'}$ are shown at the same points as those of $\overline{w'h'}$ and $L\rho\overline{w'(q'+l')}$ (Figure 4.8). At the initial time the profile of $\rho\overline{w's_V'}$ is the horizontally homogeneous steady state profile with $\rho(\overline{w's_V'})_S < 0$. Downstream, $\rho(\overline{w's_V'})_S$ becomes positive and the slopes of $\rho\overline{w's_V'}$ both in the cloud and subcloud layers become negative due to the same convergence of h and $q+l$ evident in the $\overline{w'h'}$ and $L\rho\overline{w'(q'+l')}$ profiles. Since the area under $\rho\overline{w's_V'}$ near the surface is almost always positive, the positive water vapor flux is enough to compensate for the negative heat flux.

The two dimensional fields of $\rho(\overline{w's_V'})_S$, $\rho(\overline{w's_V'})_{z_C^-}$, $\rho(\overline{w's_V'})_{z_C^+}$, and $\rho(\overline{w's_V'})_B$ are shown in Figure 4.9, where $(\overline{w's_V'})_{z_C^+} = \beta[(1 - \frac{z_C}{z_B})(\overline{w'h'})_S + \frac{z_C}{z_B}(\overline{w'h'})_B] - \epsilon L[(1 - \frac{z_C}{z_B})\overline{w'(q'+l')}_S + \frac{z_C}{z_B}\overline{w'(q'+l')}_B]$. Except for the initialization at the southern and eastern edges of the field, $\rho(\overline{w's_V'})_S$ remains mostly positive. $\rho(\overline{w's_V'})_{z_C^-}$ varies most slowly of the four fields, decreasing towards the west and always remaining negative as required by (2.16). We have found $(\overline{w's_V'})_{\min}$ always to occur at z_C^- . $\rho(\overline{w's_V'})_B$ has a strong decreasing gradient in the northern part of the field while $\rho(\overline{w's_V'})_{z_C^+}$ varies rapidly and increases

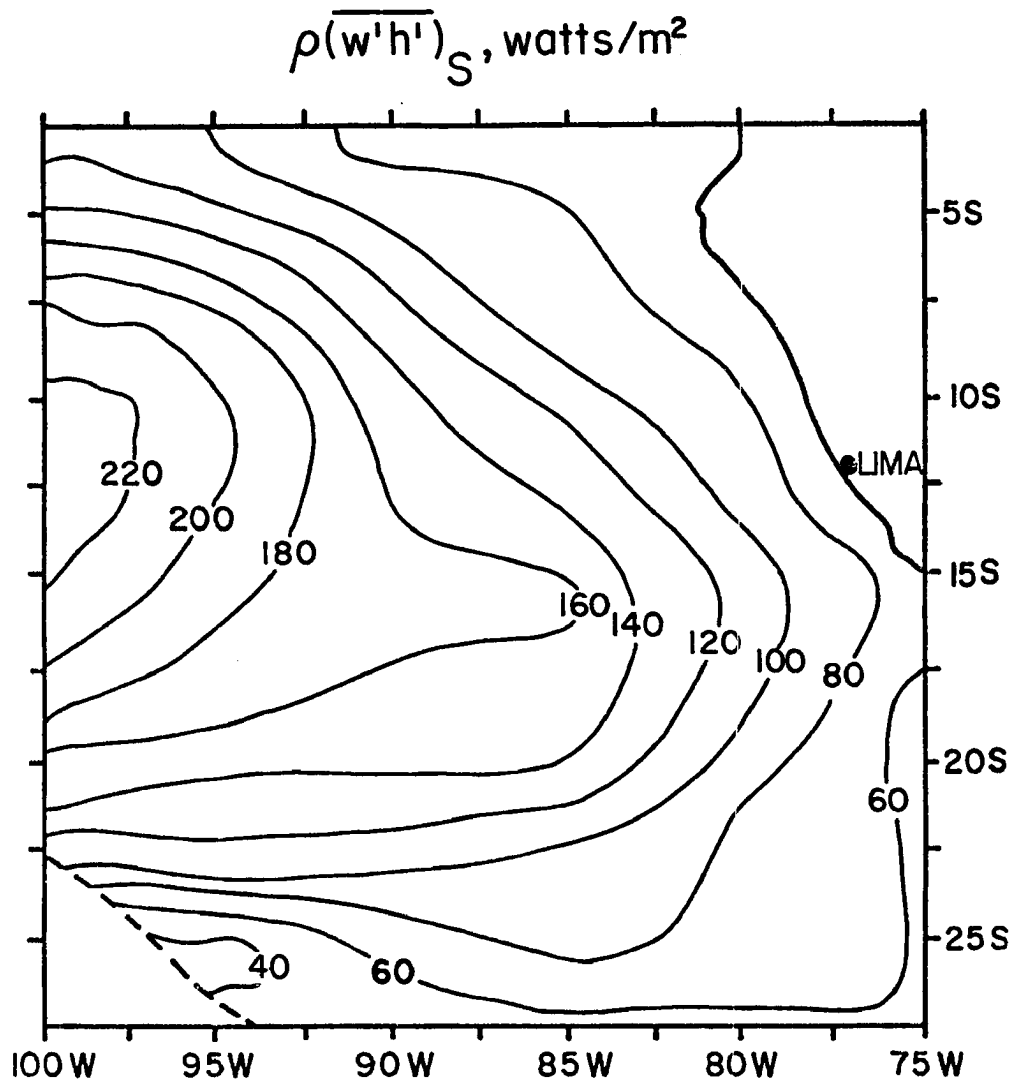


Figure 4.6a July turbulent moist static energy flux at the surface.

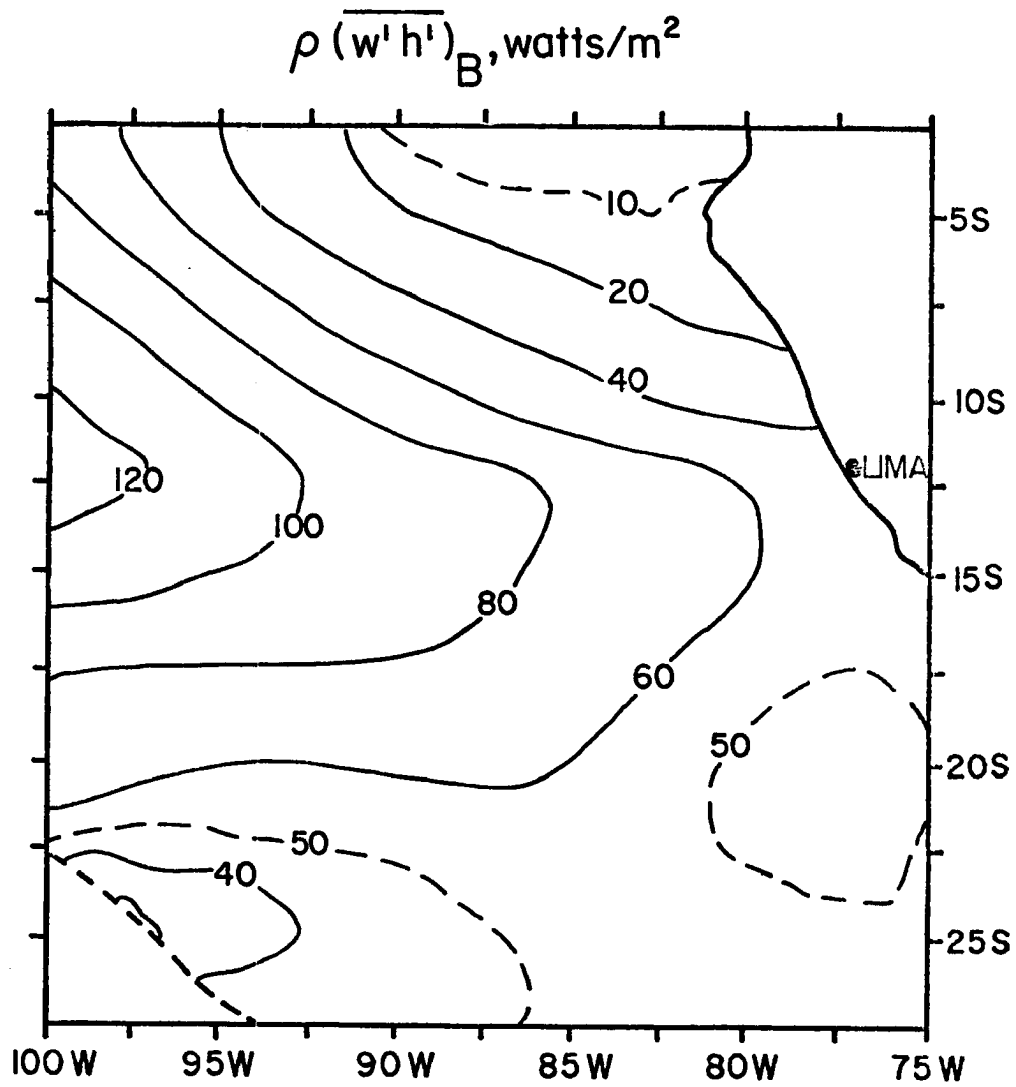


Figure 4.6b July turbulent moist static energy flux at the top of the layer.

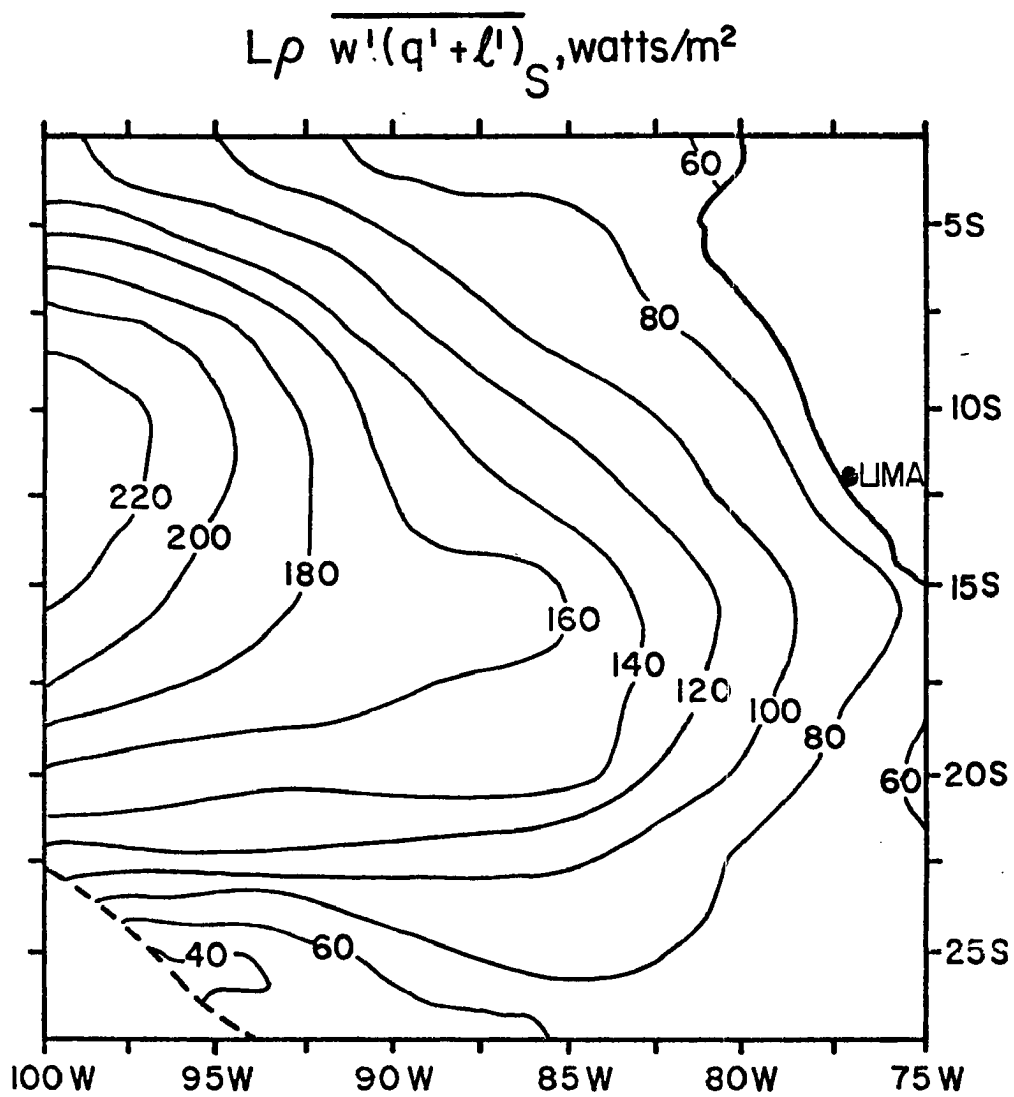


Figure 4.7a July turbulent flux of total water at the surface.

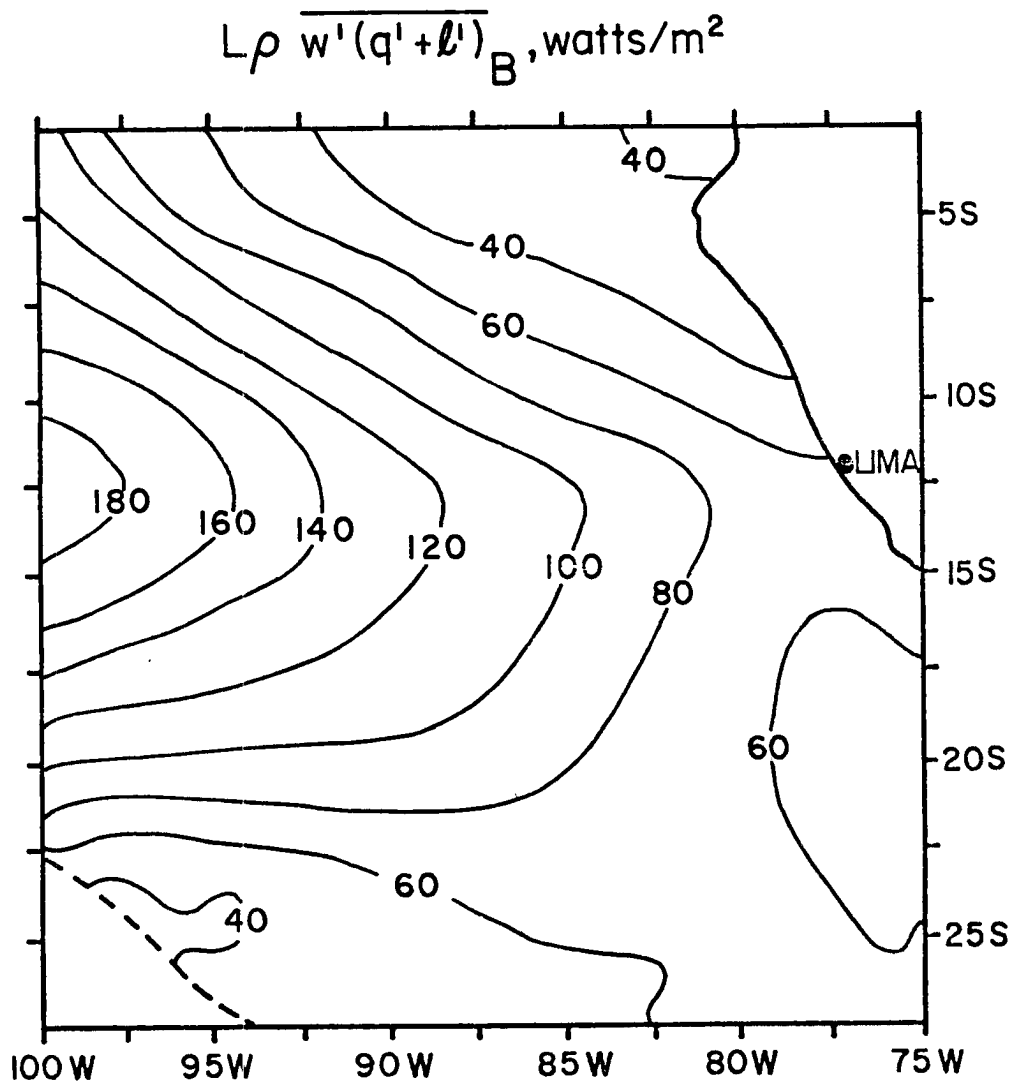


Figure 4.7b July turbulent flux of total water at the top of the layer.

JULY

$\rho \overline{(w' s_v')}$, watts/m²

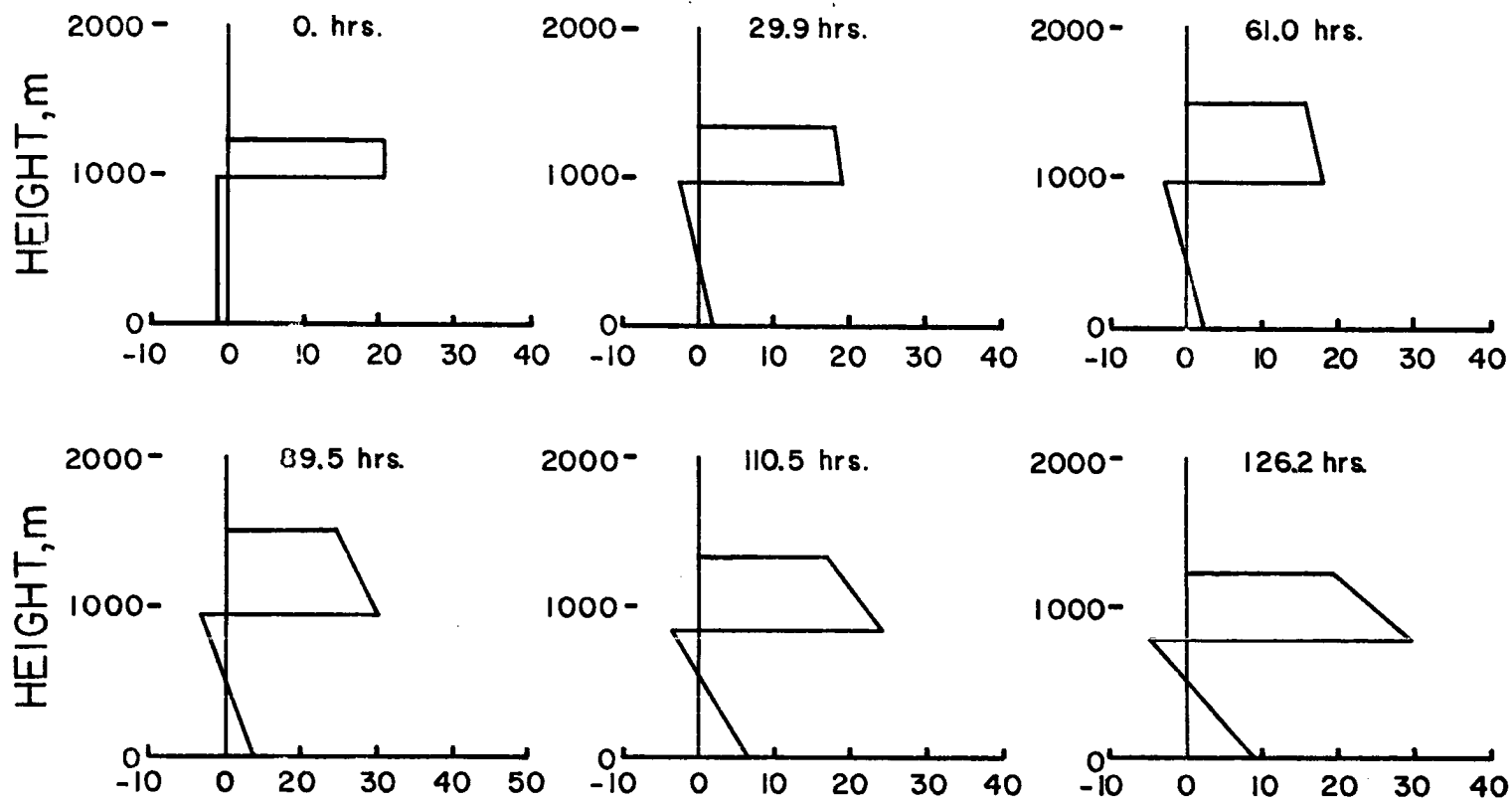


Figure 4.8 July vertical profiles of the turbulent virtual dry static energy flux every 300 km along the trajectory beginning at 76.5°W, 27.5°S. The time in hours from initialization is indicated.

JULY

$\rho (\overline{w' s_v'})$, watts/m²

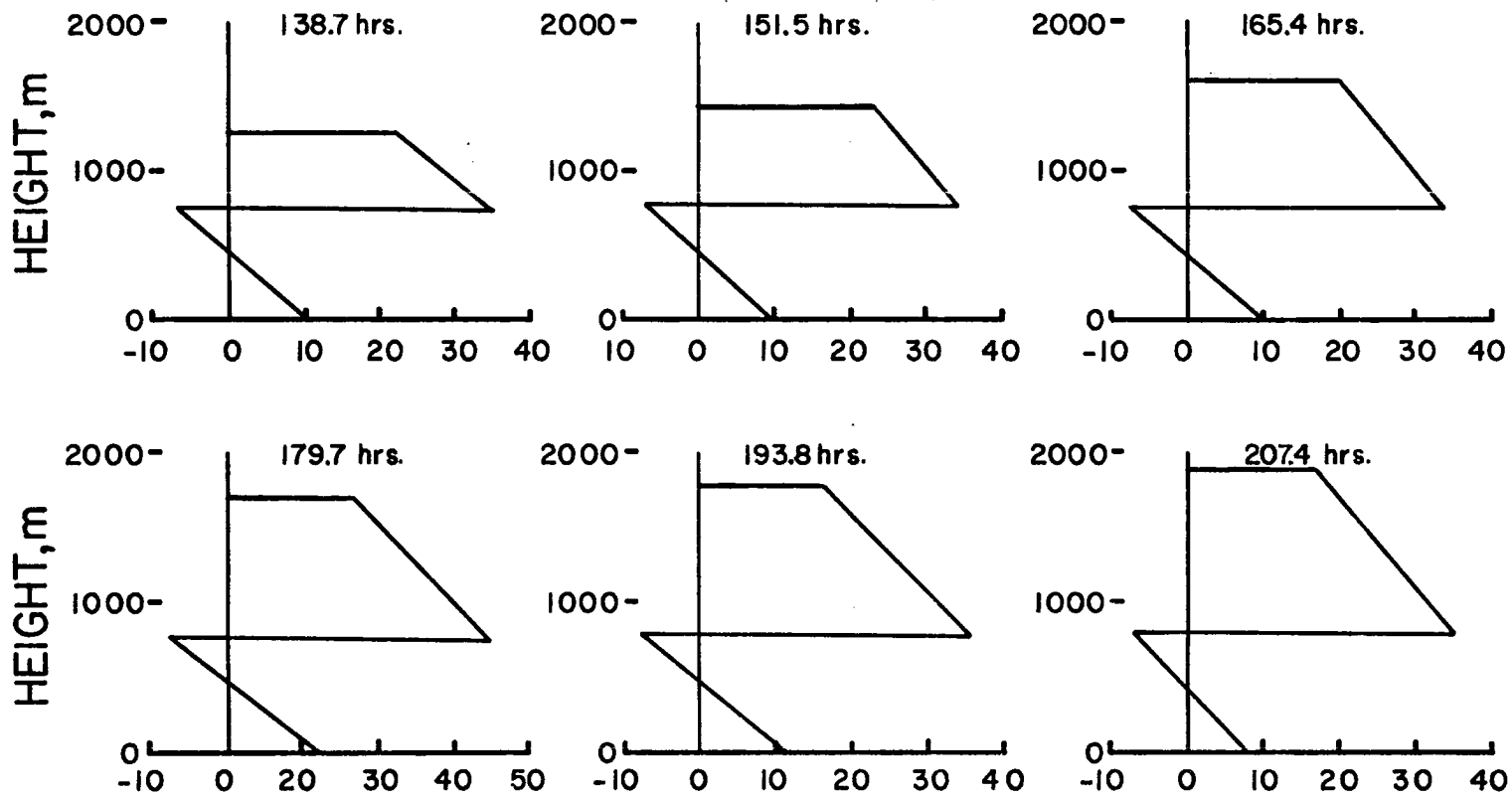


Figure 4.8 Continued.

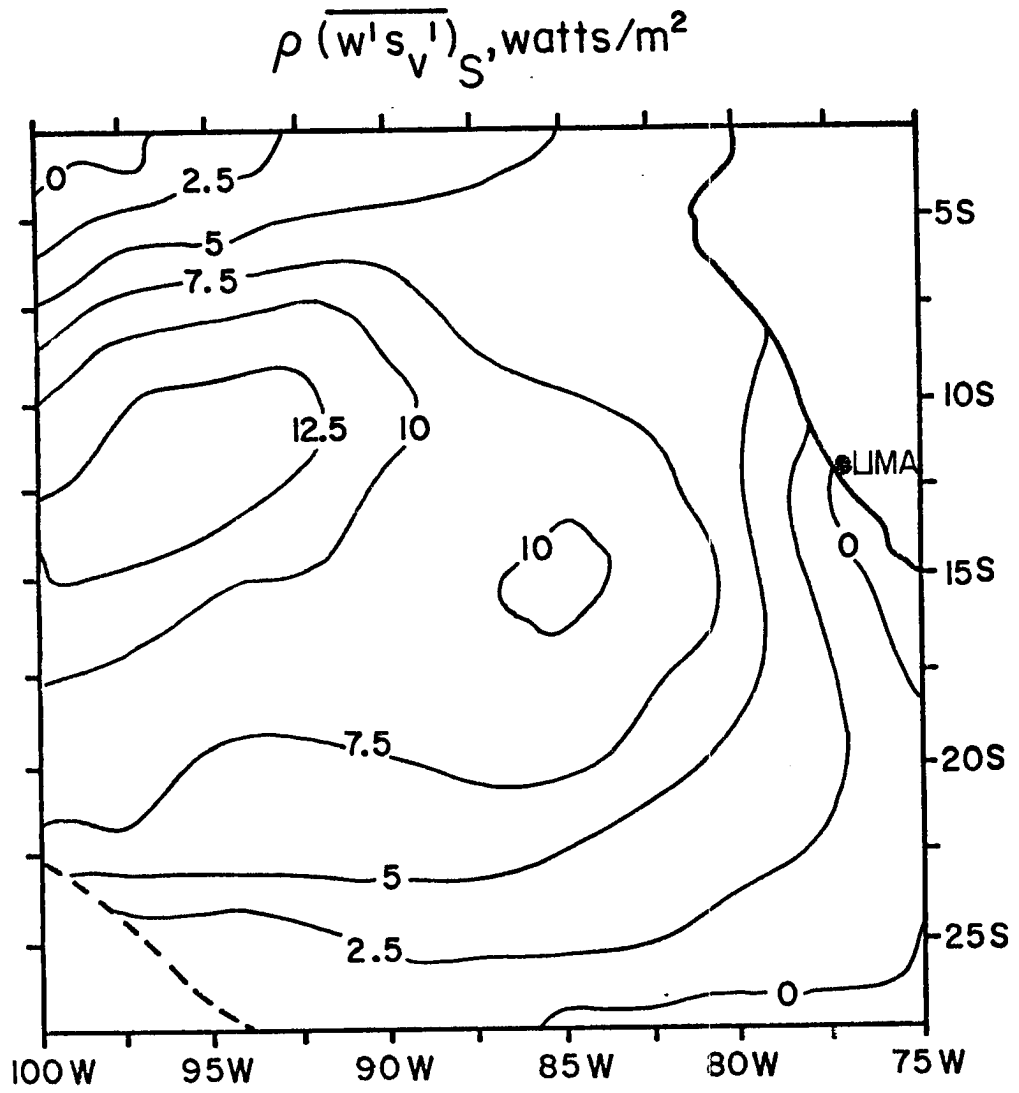


Figure 4.9a July turbulent flux of virtual dry static energy at the surface.

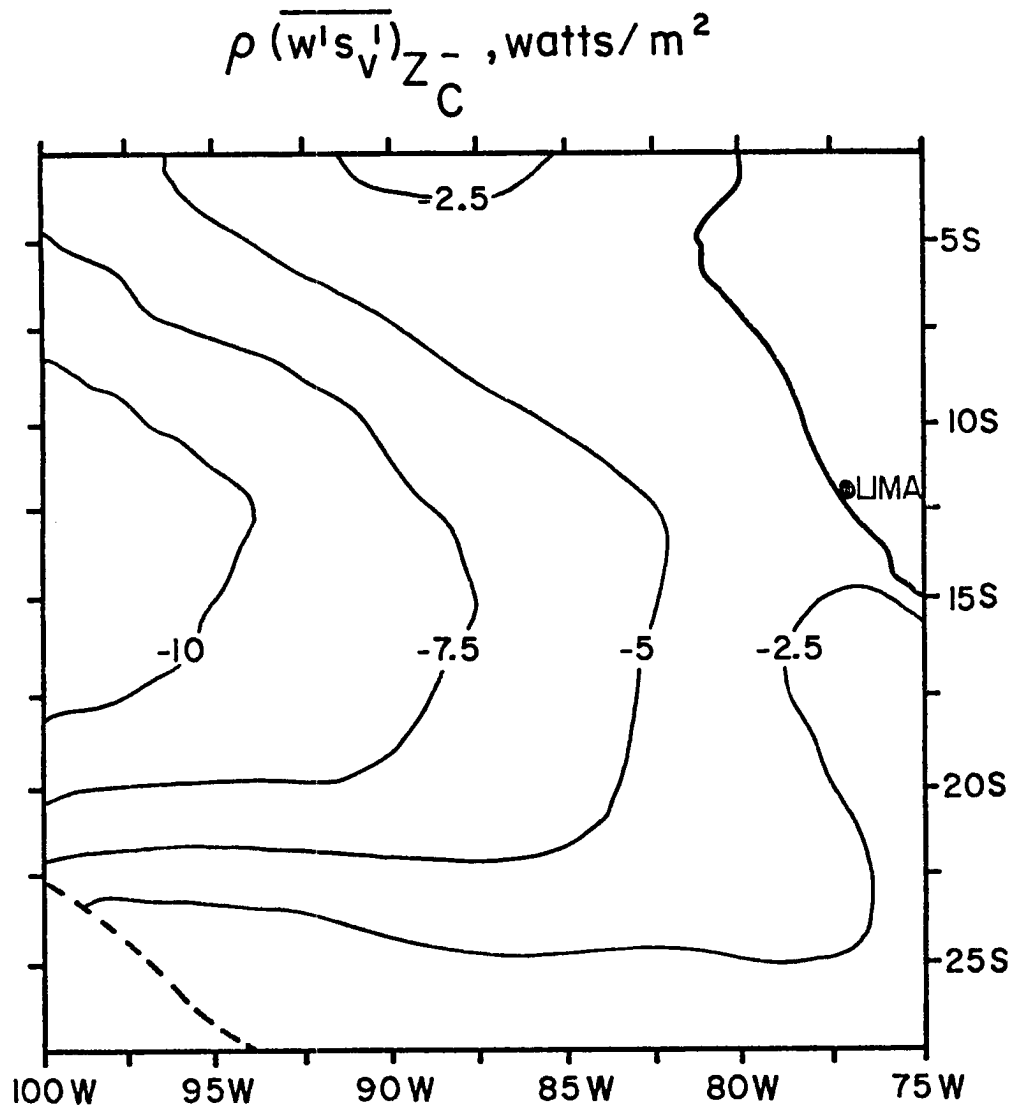


Figure 4.9b July turbulent flux of virtual dry static energy just below cloud base.

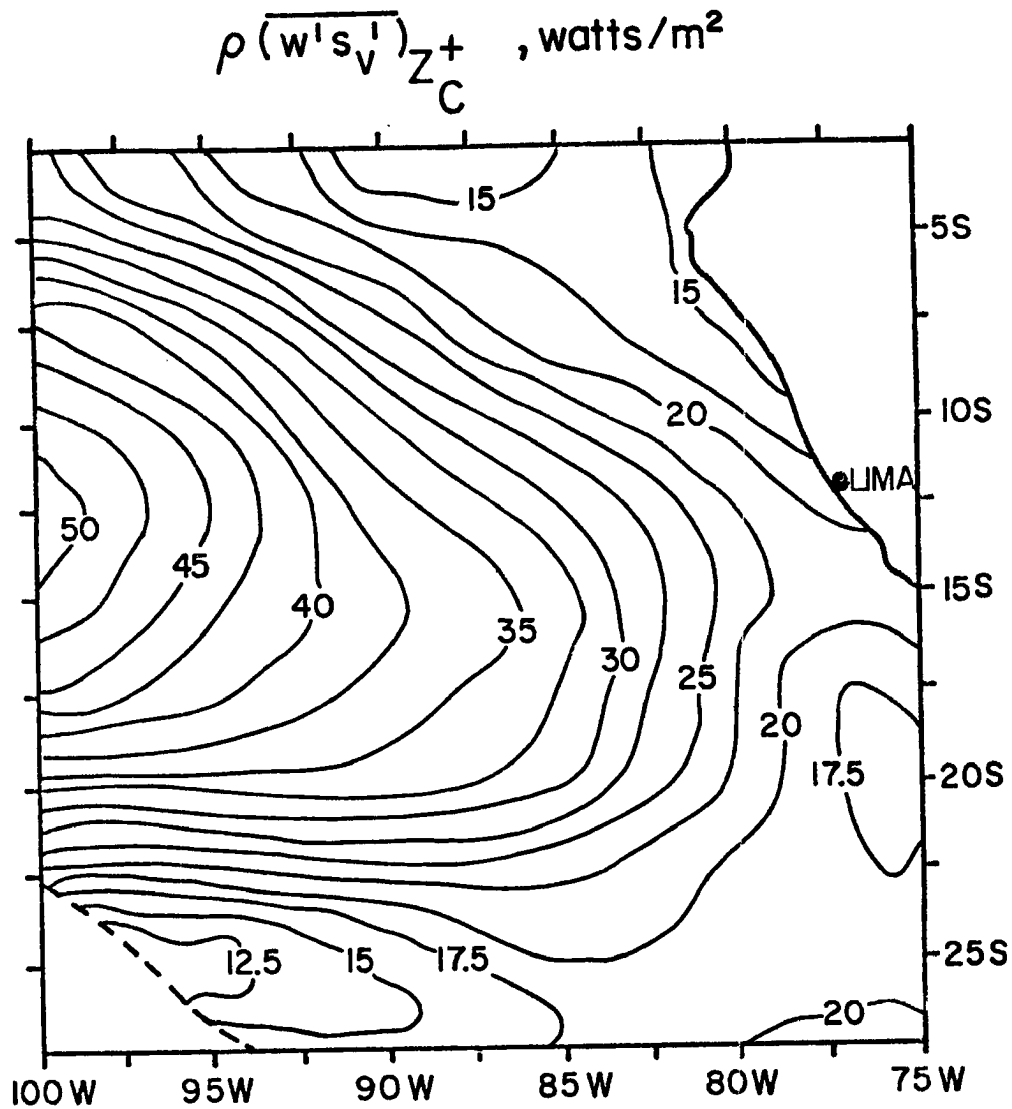


Figure 4.9c July turbulent flux of virtual dry static energy just above cloud base.

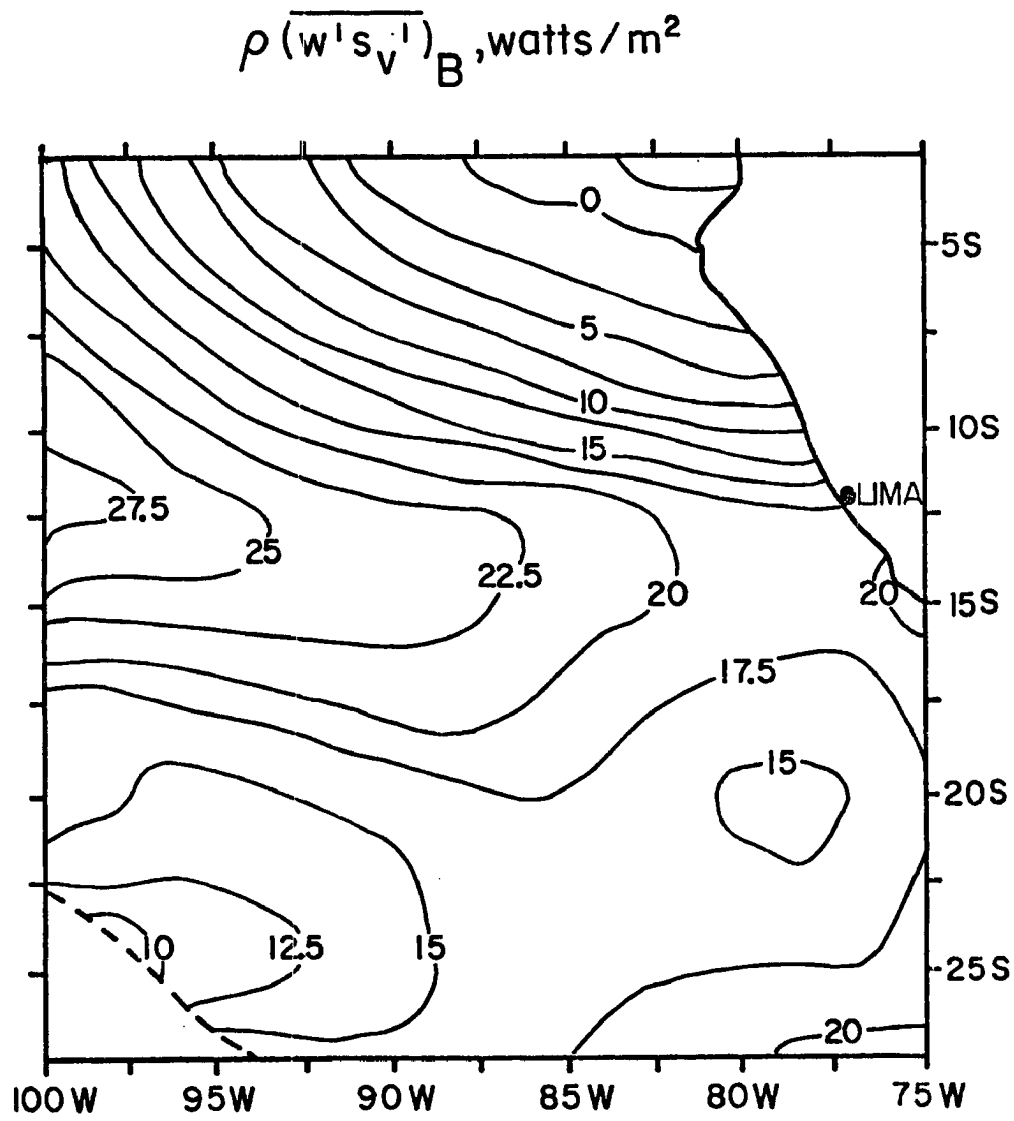


Figure 4.9d July turbulent flux of virtual dry static energy at layer top.

towards the west. Similar gradients appear in the $\overline{\rho w^T h^T}$ and $L \overline{\rho w^T (q^T + \ell^T)}$ fields of which $\overline{\rho w^T s_V^T}$ is a linear combination.

Since the scale height, H , and density, ρ , are functions solely of T_S , they were not plotted. The ϵ field is not shown either because it is so flat. ϵ and H increase with increasing T_S and ρ decreases. Typical values for H , ρ and ϵ letting $T_S = 20^\circ\text{C}$, are 8585 m, 1.212 kg/m^3 , and 0.120, respectively. The β , γ , and b fields are shown in Figure 4.13. All three fields have isolines paralleling those of T_S . β decreases slightly to the northwest, while both γ and b increase by more than 50%. b is particularly important in the computation of z_C ; the increase of b towards the north corresponds to the decrease of z_C .

Most of the model results agree well with reasoning from an intuitive standpoint. The increases of h_M and $(q + \ell)_M$ towards the equator, for example, are what we expect from the warmer sea surface temperature there. In terms of cloud top, base, and depth fields, the model has produced low level, fairly shallow clouds with both cloud depth and height increasing away from the coast. Ideally, the cloud top temperature field (Figure 4.2d) should be compared to monthly averaged satellite data, but unfortunately such data were not readily available. It is easy to make direct comparisons between some of the fields (such as z_B or the surface fluxes) and the input fields, but with others (such as the fluxes at the top of the layer) it is more difficult to pinpoint the cause of any particular feature. In one sense, those fields are the most interesting since they are difficult to predict from a physical standpoint. Assuming the model is reasonable based upon results that do

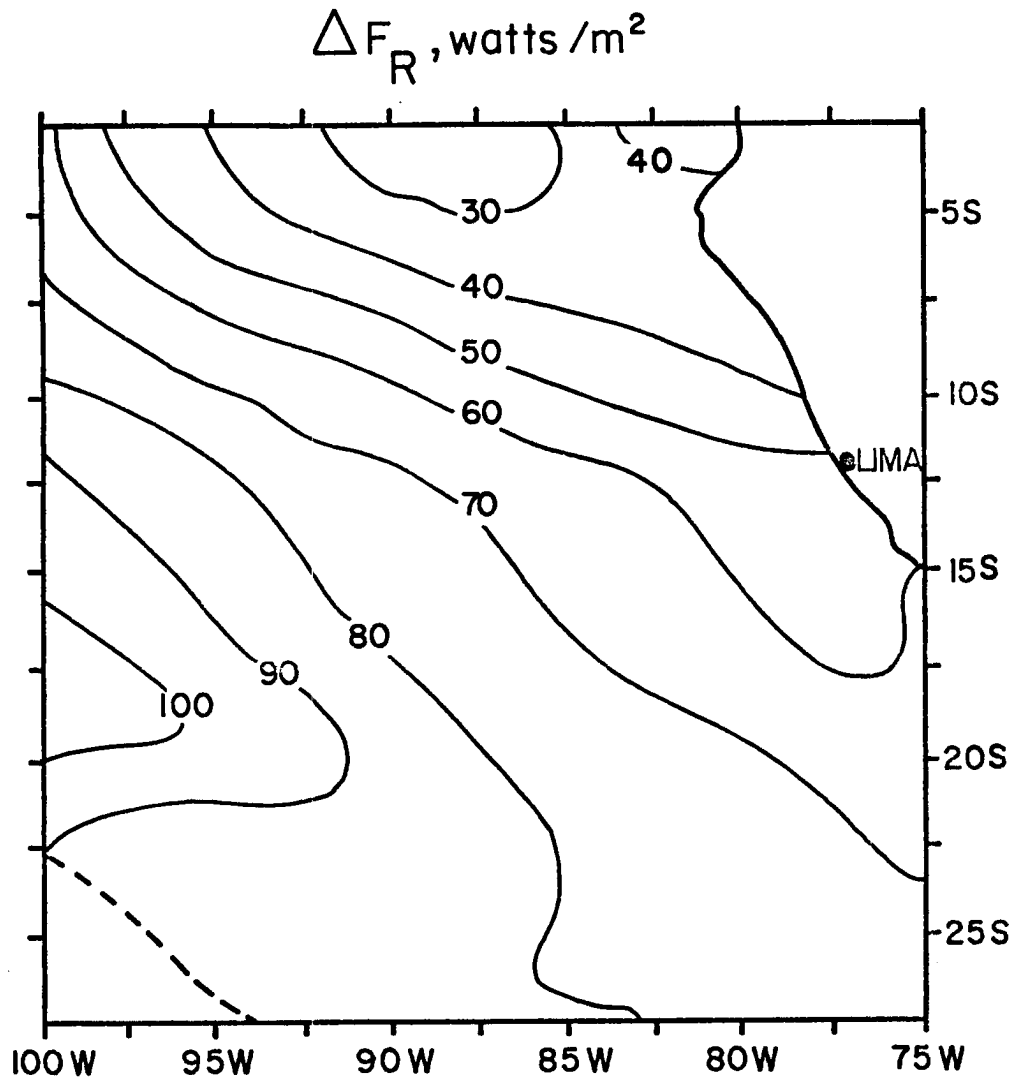


Figure 4.10a July jump of total radiative flux at cloud top.

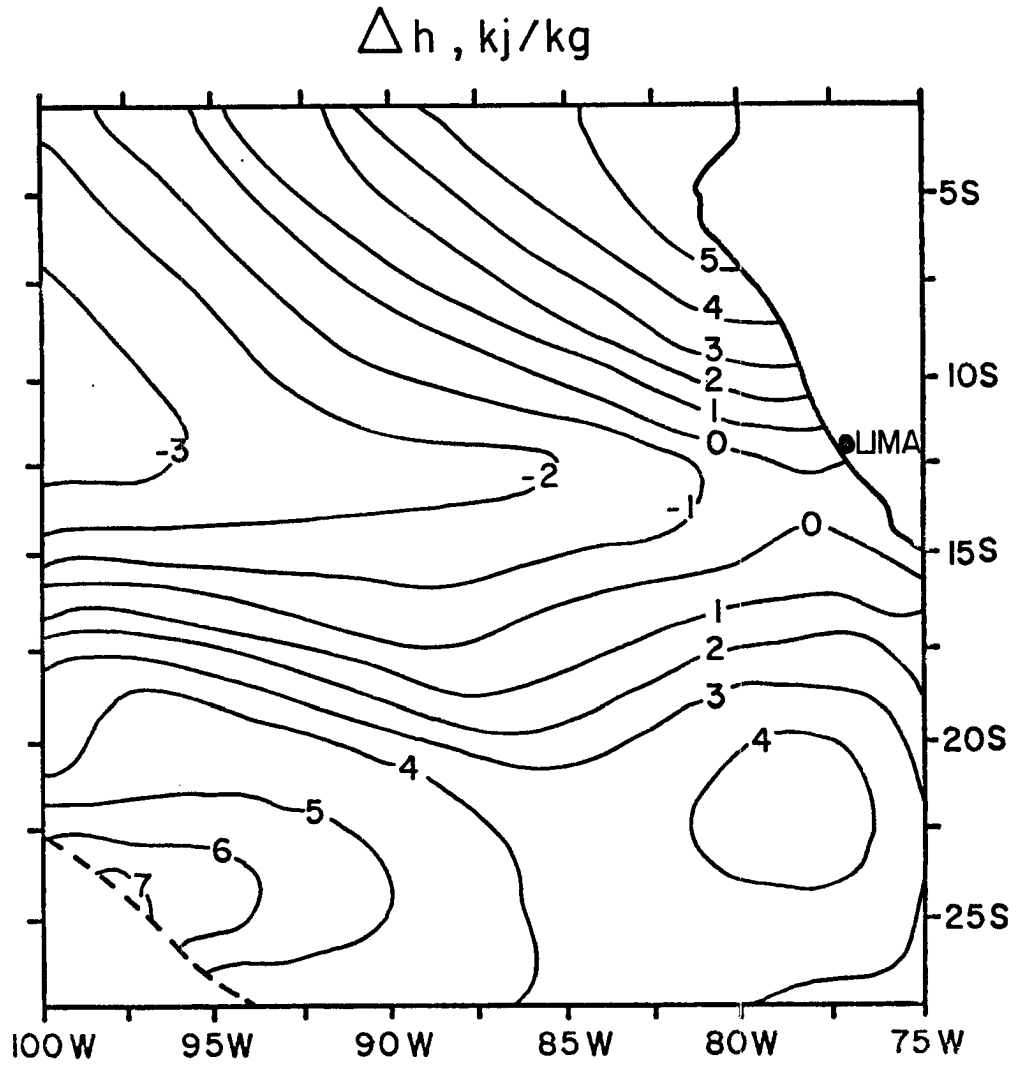


Figure 4.10b July jump of moist static energy at cloud top.

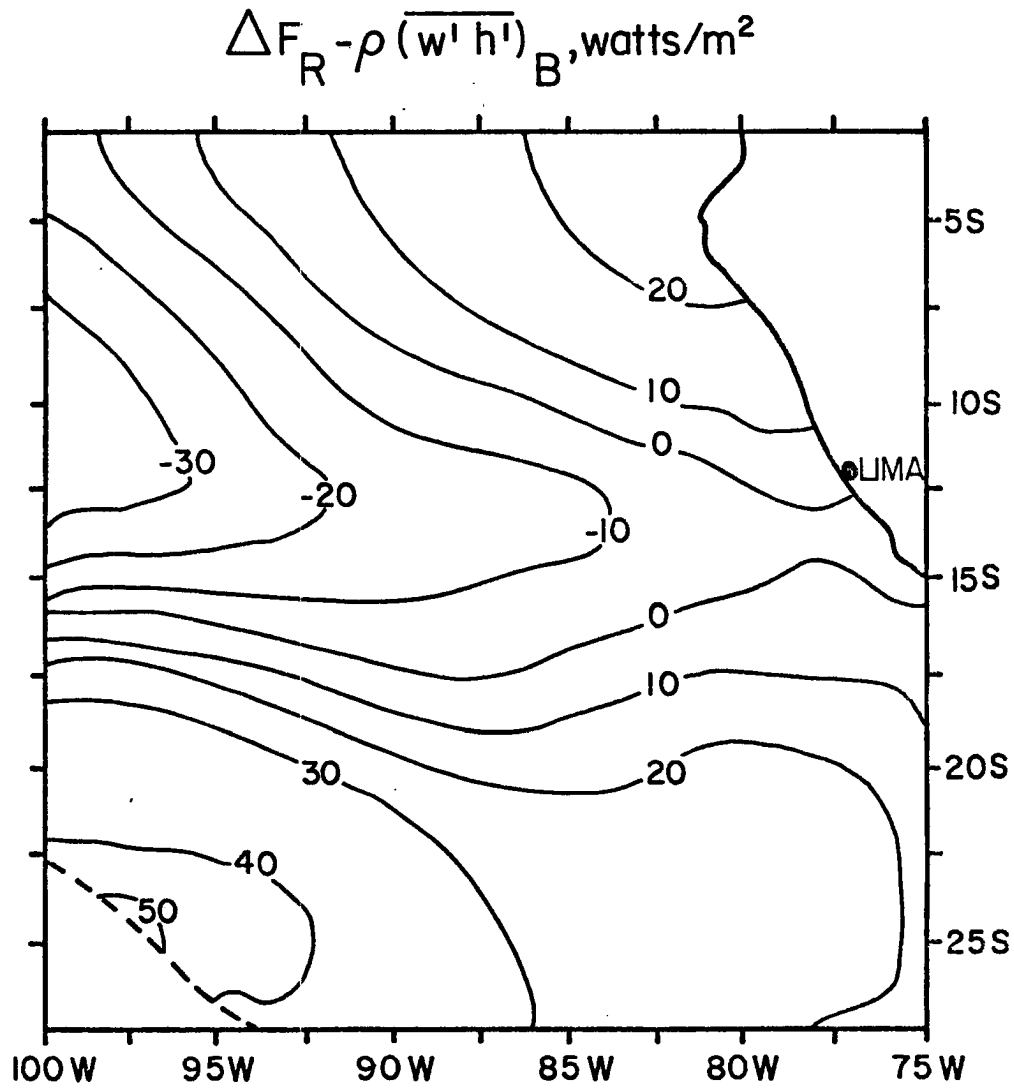


Figure 4.11a July jump of radiative flux at cloud top minus the turbulent flux of moist static energy at cloud top.

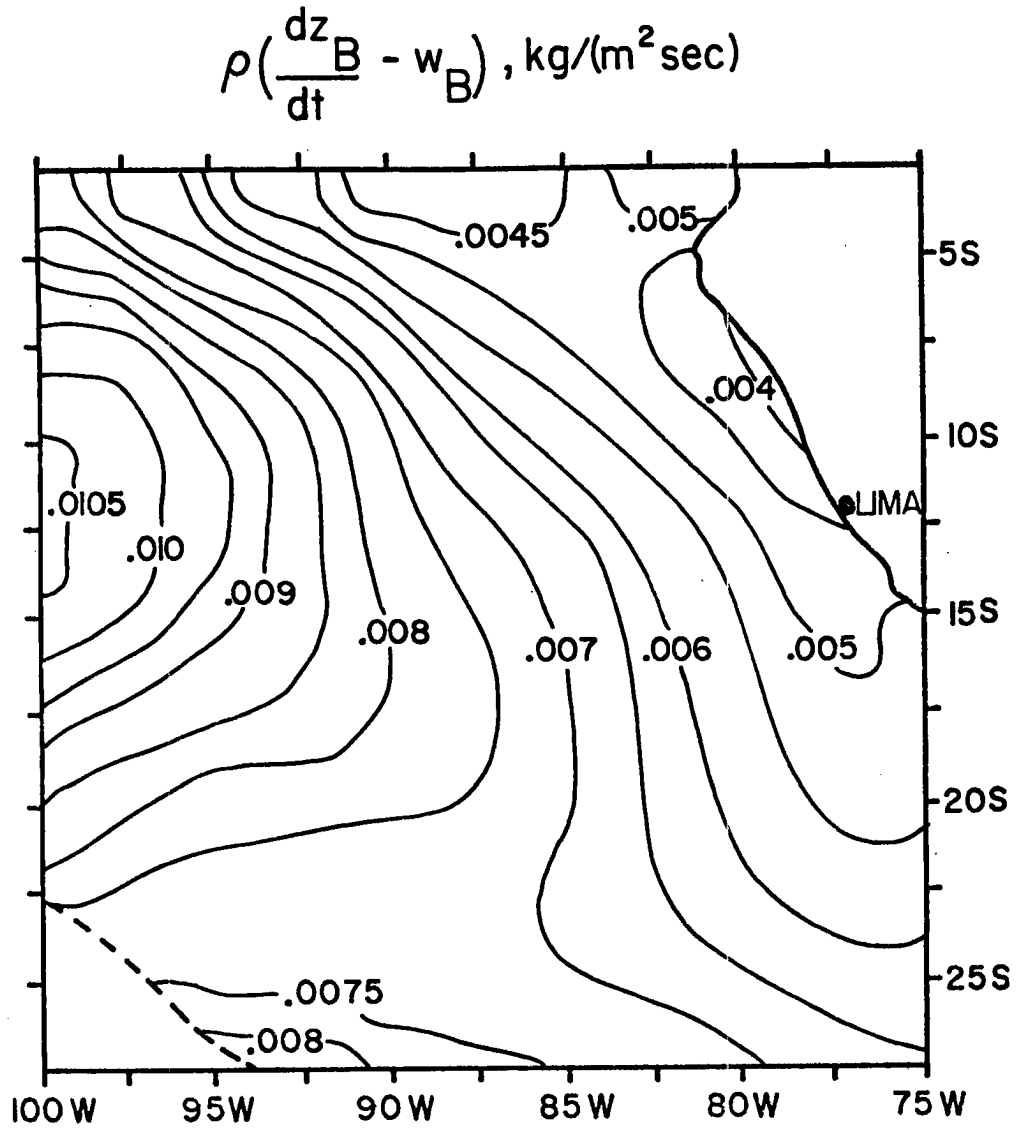


Figure 4.11b July mass entrainment at cloud top.

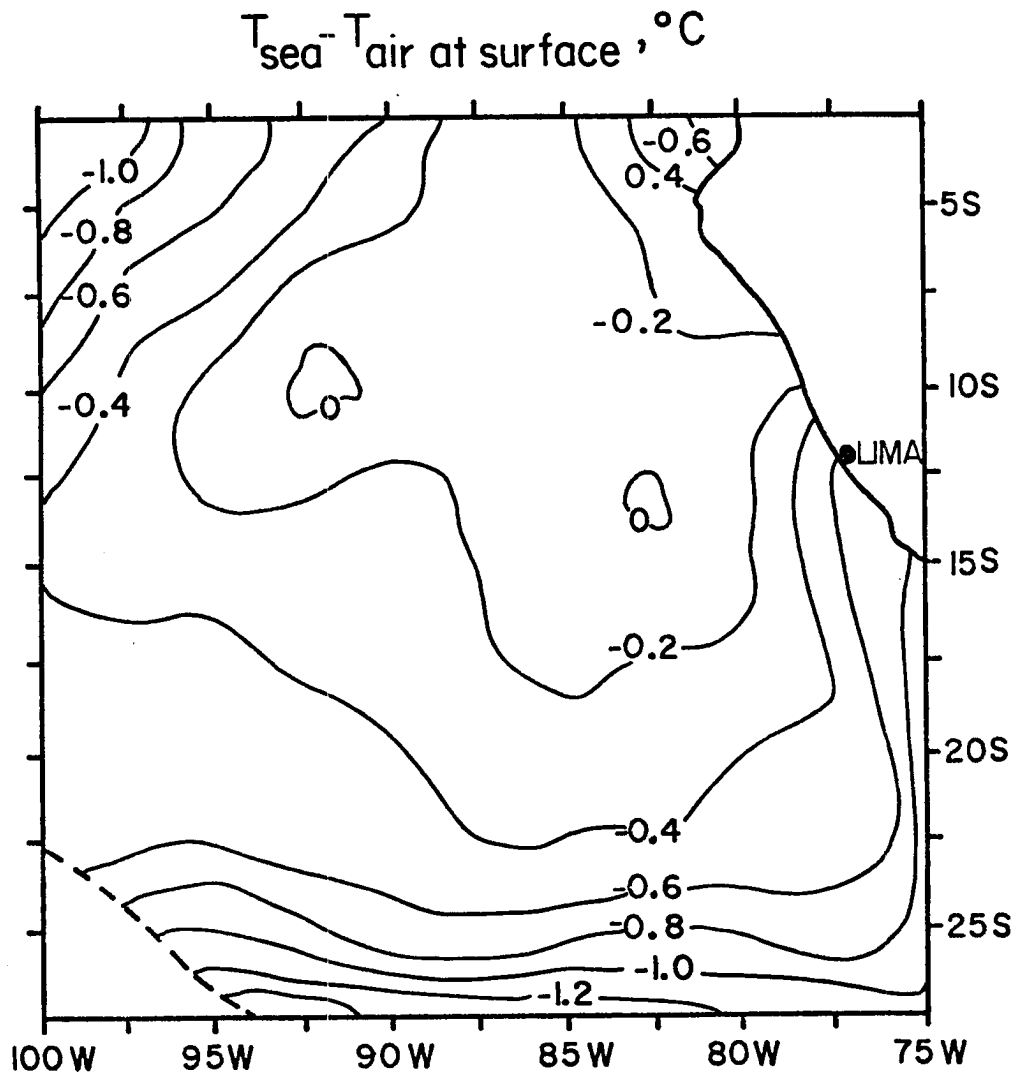


Figure 4.12 July difference between the sea surface temperature and the air temperature at the surface.

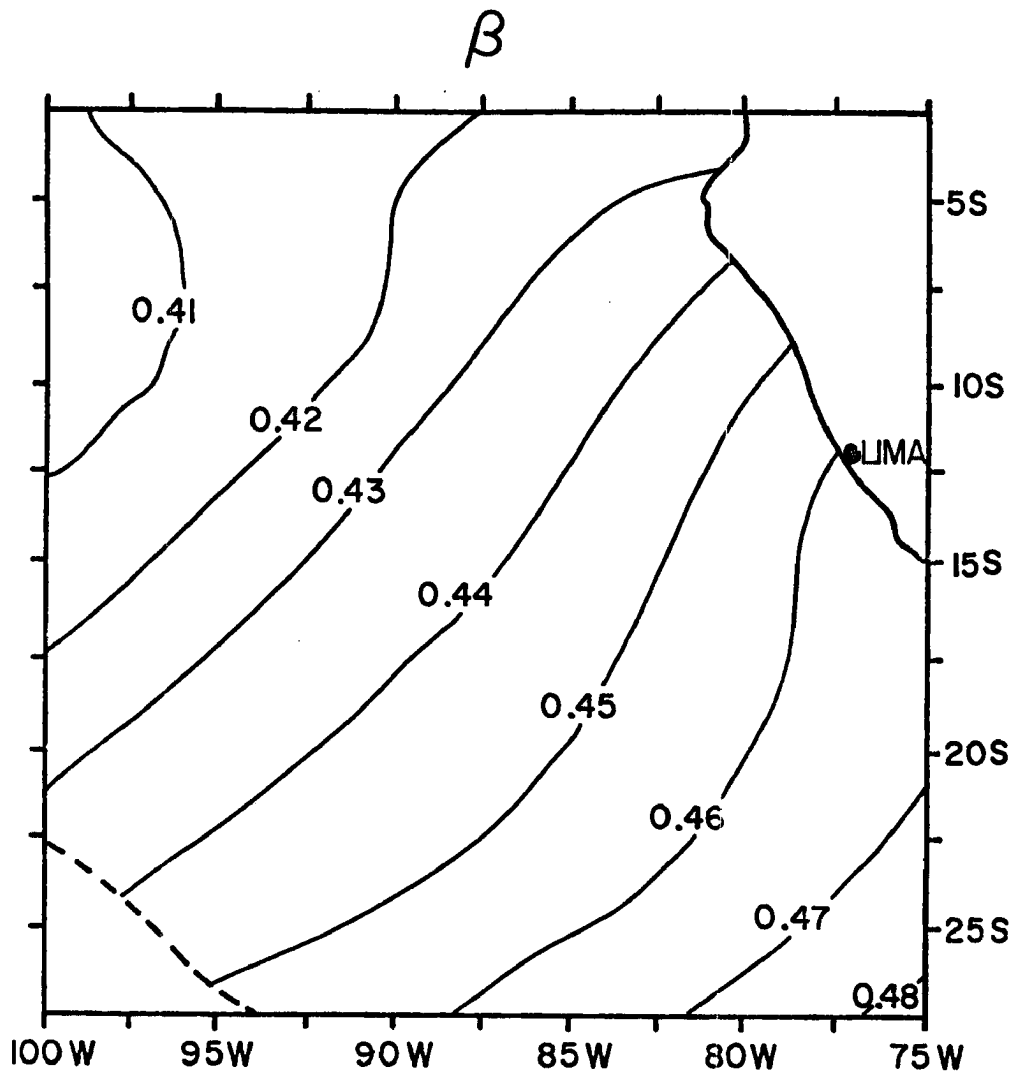
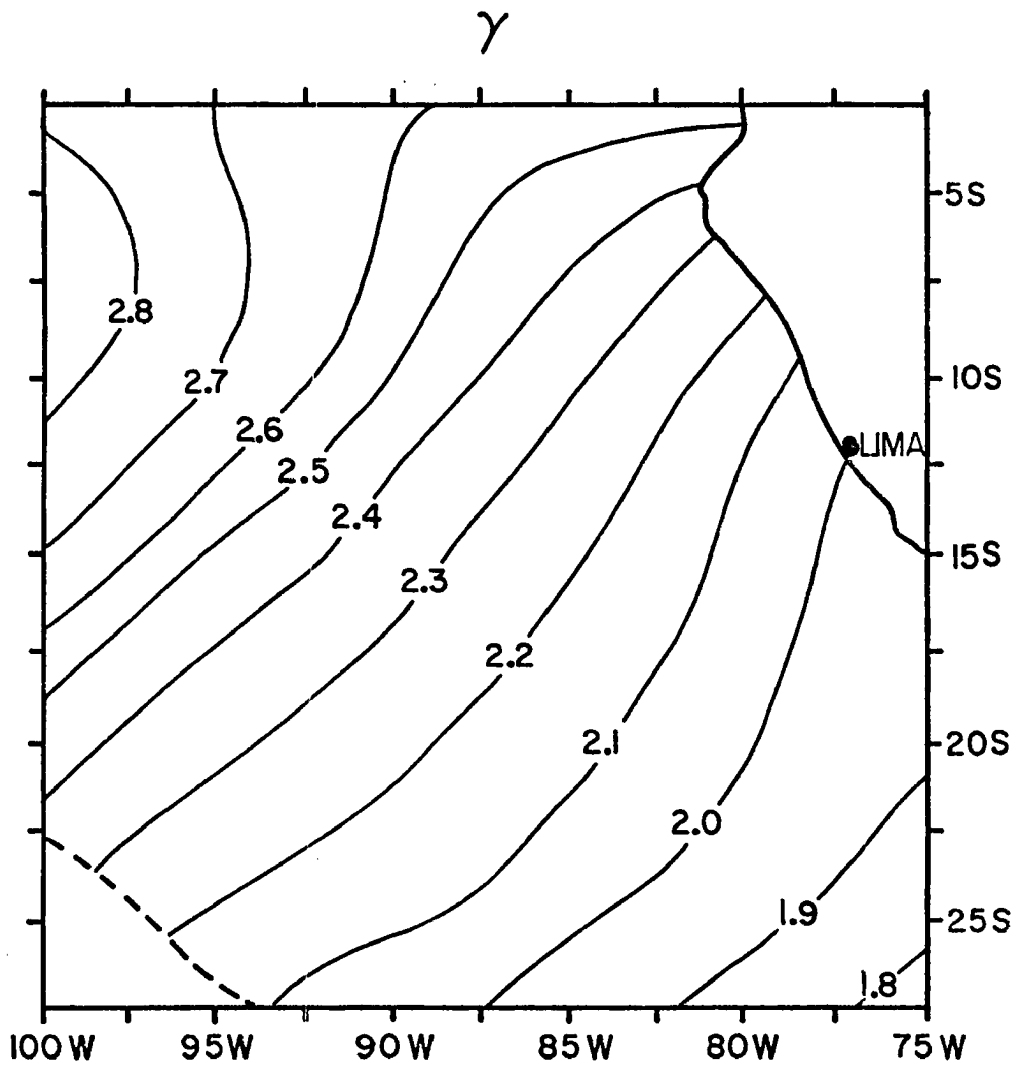


Figure 4.13a July β .

Figure 4.13b July γ .

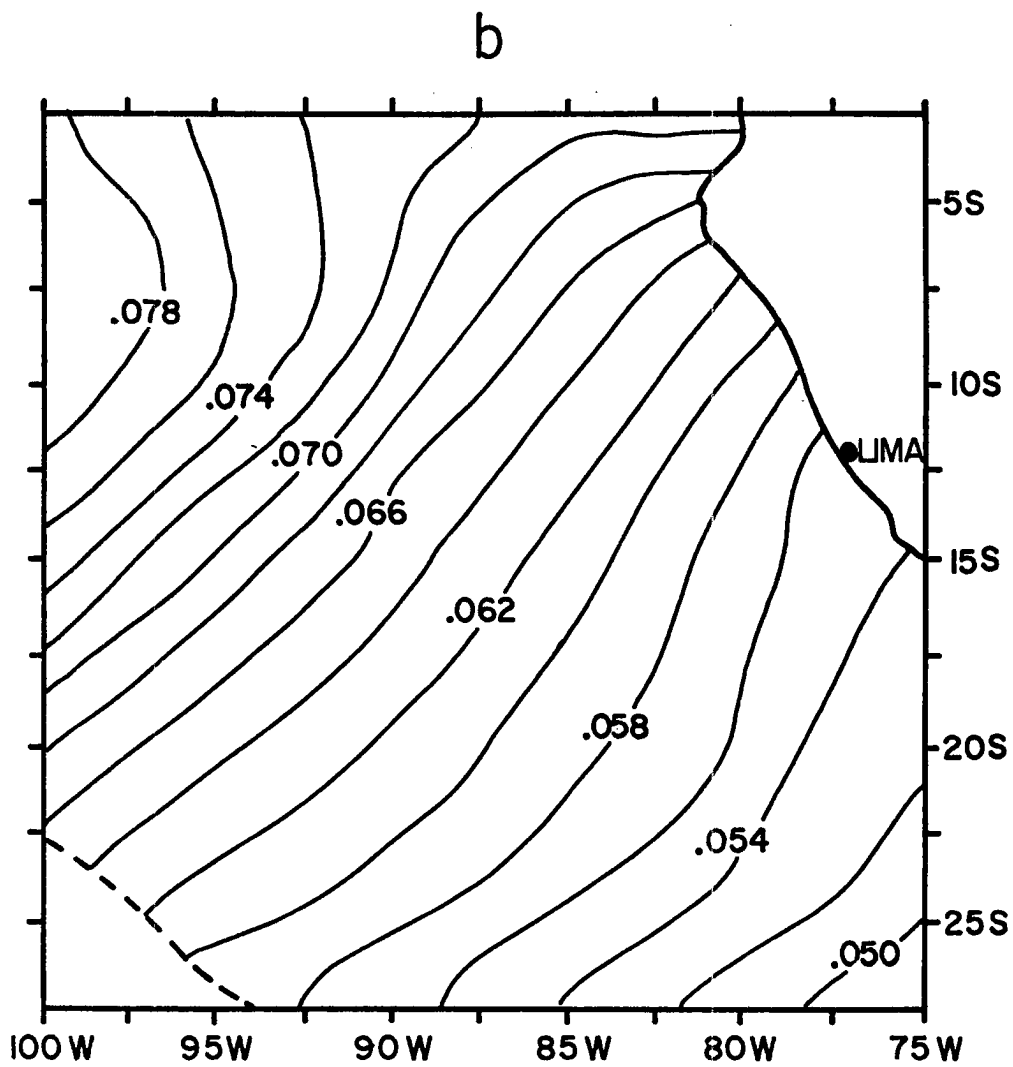


Figure 4.13c July b.

seem feasible, we can gain information about those fields whose structure may not otherwise be as obvious. In any case, none of the fields (with the exception of the H , ρ , ϵ , γ , β and b fields) are perfectly correlated with any of the input fields; rather, they all show the influence of complicated interactions with other model variables as well. It is regrettable that there is no data from this part of the globe with which to compare the model results.

There are some reservations to be kept in mind when interpreting the results. Some of the fields (such as the flux fields) reflect to a degree the starting place of the trajectories at the southern and eastern edges. One implicit assumption of the model is that all the air in the northwestern regions, that is, downstream along the trajectories, has been modified in the same manner as the air upstream along the trajectories. There is, however, a discontinuity arising because some of the trajectories were begun on the eastern edge and some on the southern edge. This discontinuity has been smoothed by the interpolation.

In section 4.2, we discuss the results of the August case, in section 4.3 we investigate the July case with no solar absorption, and in section 4.4 we discuss the July case with a lower initial divergence.

4.2 Results of the August Case

The movement along the trajectories over the input fields of T_S , V , and D for August is shown in Figure 4.14. The other variables that are different for August than for July are the temperature and moisture structure above the mixed layer, the downward longwave radiative flux above the mixed layer, and the shortwave absorption. All these are similar to July's. Since it is reasonable to assume the same physical

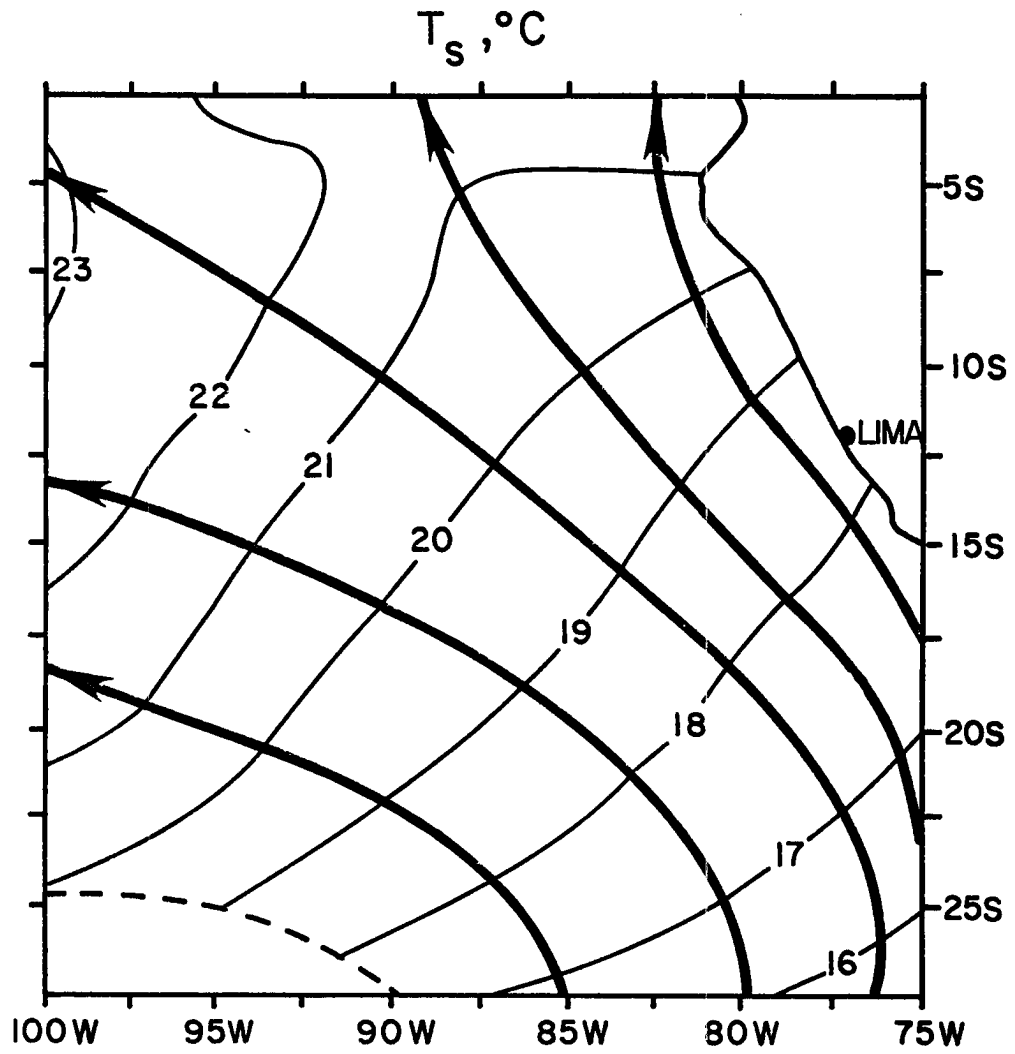


Figure 4.14a August input variable of sea surface temperature. Heavy lines indicate trajectories.

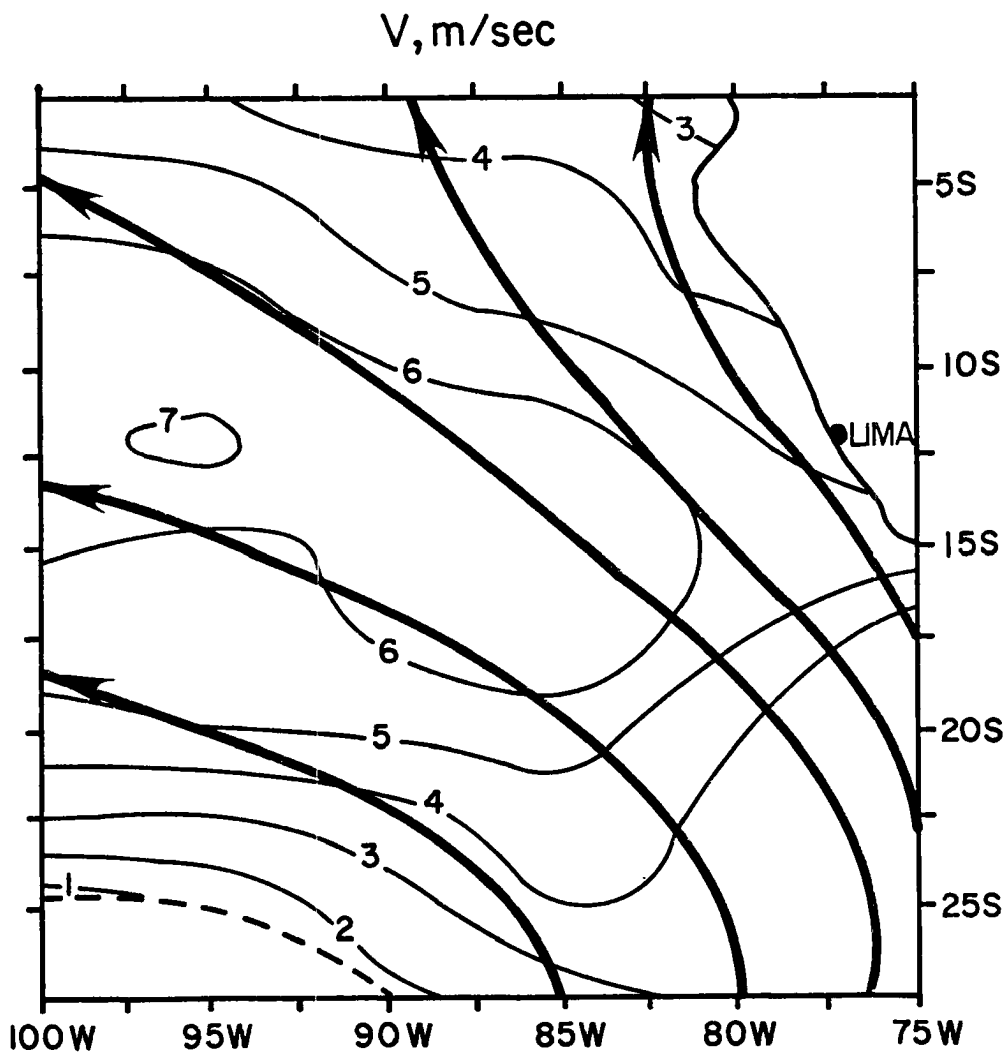


Figure 4.14b August input variable of surface wind speed. Heavy lines indicate trajectories.

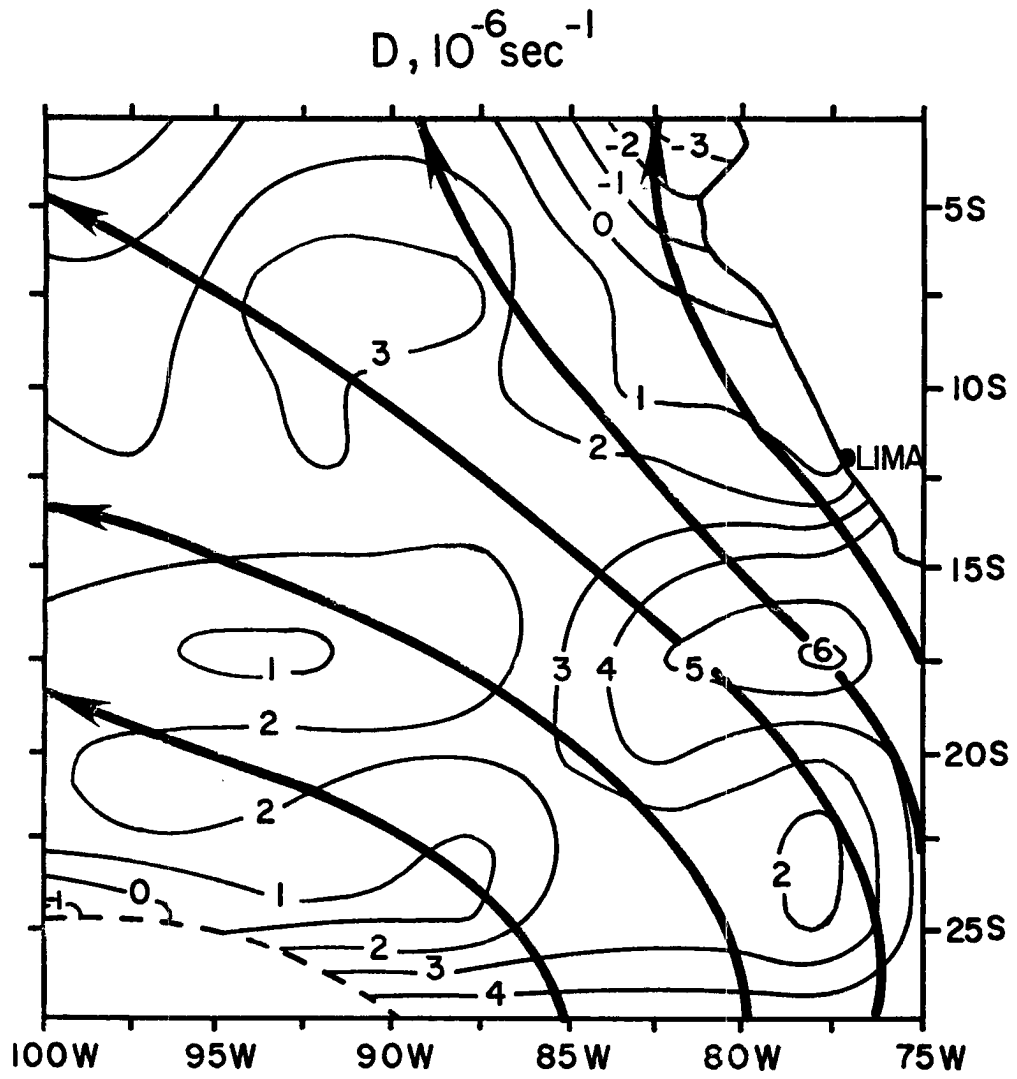


Figure 4.14c August input variable of large-scale divergence. Heavy lines indicate trajectories.

processes at work in August, our purpose in presenting the August case is primarily to compare it to the July case.

The strong western gradient so pronounced in the July z_B field is nearly absent in August (Figure 4.15a). This difference can be traced to the divergence field which is about $1 \times 10^{-6} \text{ sec}^{-1}$ higher in this region than that of July's. In relative terms, that is almost a 100% increase. Overall, the August z_B field is lower.

z_C (Figure 4.15b) is 100 m - 200 m lower in August. Since T_S is about the same for both months, the difference is most likely the result of the $(q+l)_M$ field (Figure 4.16b) which is about .5 gm/kg - 1 gm/kg higher in August. h_M in August is higher as well (Figure 4.16b), but a comparison of the $(s - L\ell)_M$ fields reveals the August subcloud layer is somewhat cooler throughout most of the region, also contributing to the lower z_C .

Though both z_B and z_C decrease in August, $z_B - z_C$ is shallower downstream (Figure 4.15c). As in the July case, the contours of the August $z_B - z_C$ field resemble those of the z_B field.

Because V is comparable in both months, the higher h_M and $(q+l)_M$ in August are accompanied by smaller $\rho(\overline{w'h'})_S$ and $L\rho\overline{w'(q'+l')}_S$ fields while $\rho(\overline{w'h'})_B$ and $L\rho\overline{w'(q'+l')}_B$ are both lower and flatter (Figures 4.17 and 4.18). The linear combination of these fields given by the $\rho\overline{w's_V'}$ fields is shown in Figure 4.19. $\rho(\overline{w's_V'})_B$ in August does not have as marked a western gradient near the middle of the field as does July, because those gradients in the $\rho(\overline{w'h'})_B$ and $L\rho\overline{w'(q'+l')}_B$ fields are weaker.

Although the input variables for August are much the same as for July, there are still noticeable differences in their output fields.

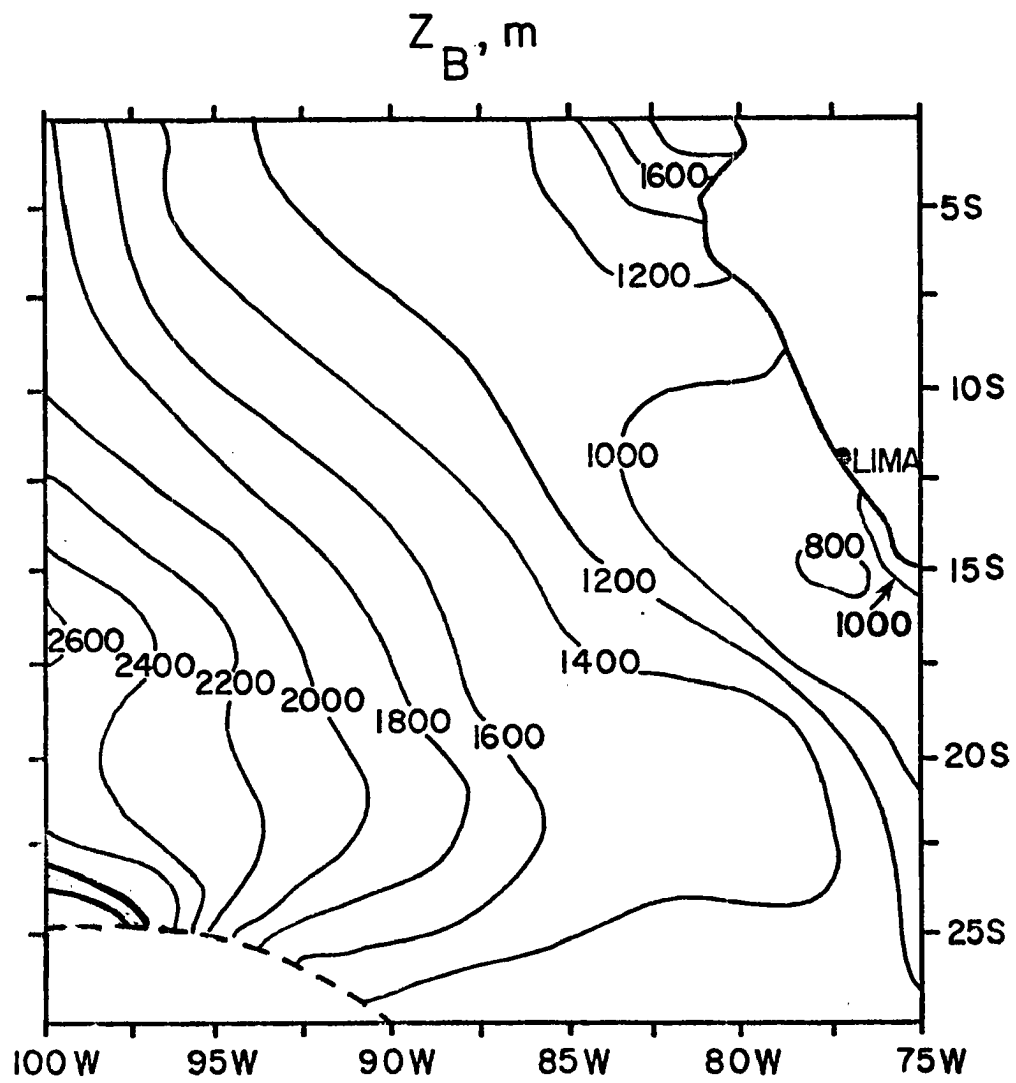


Figure 4.15a August cloud top.

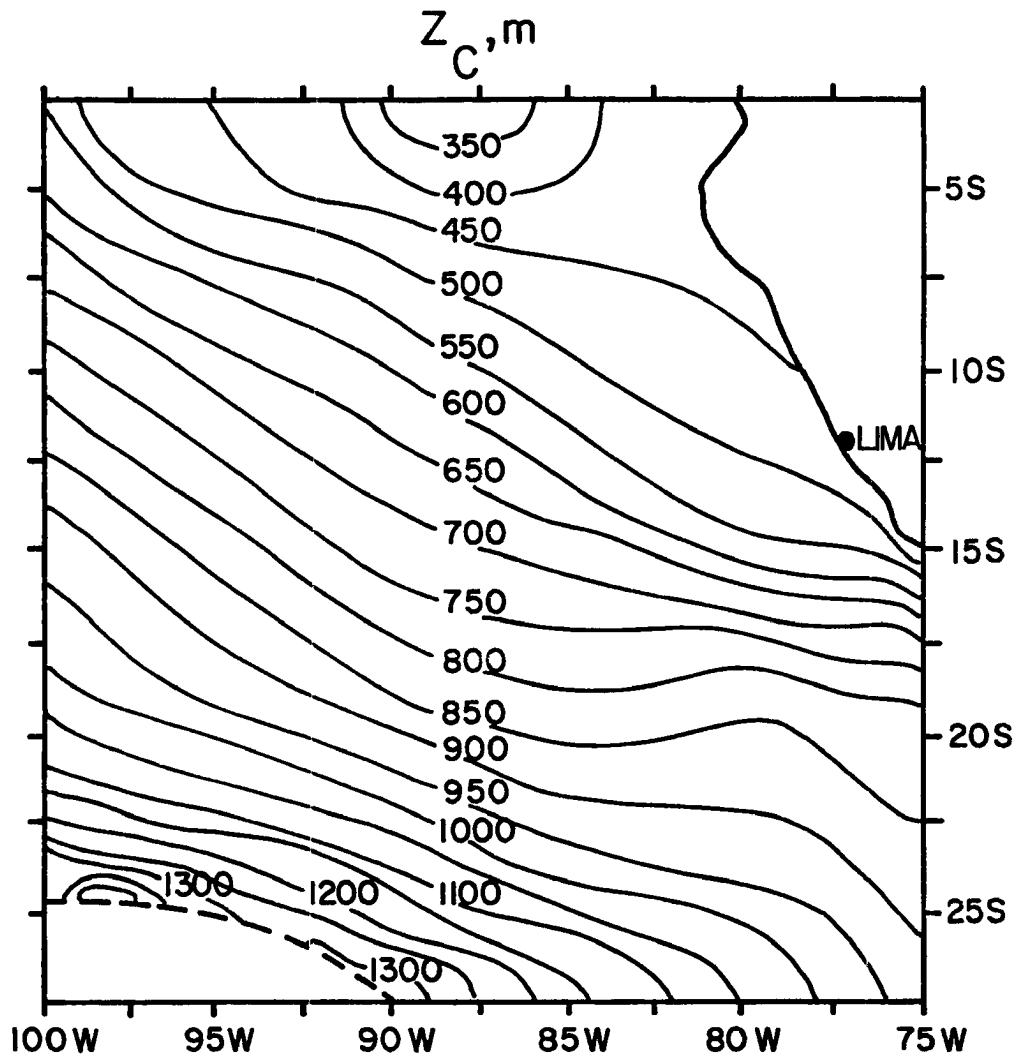


Figure 4.15b August cloud base.

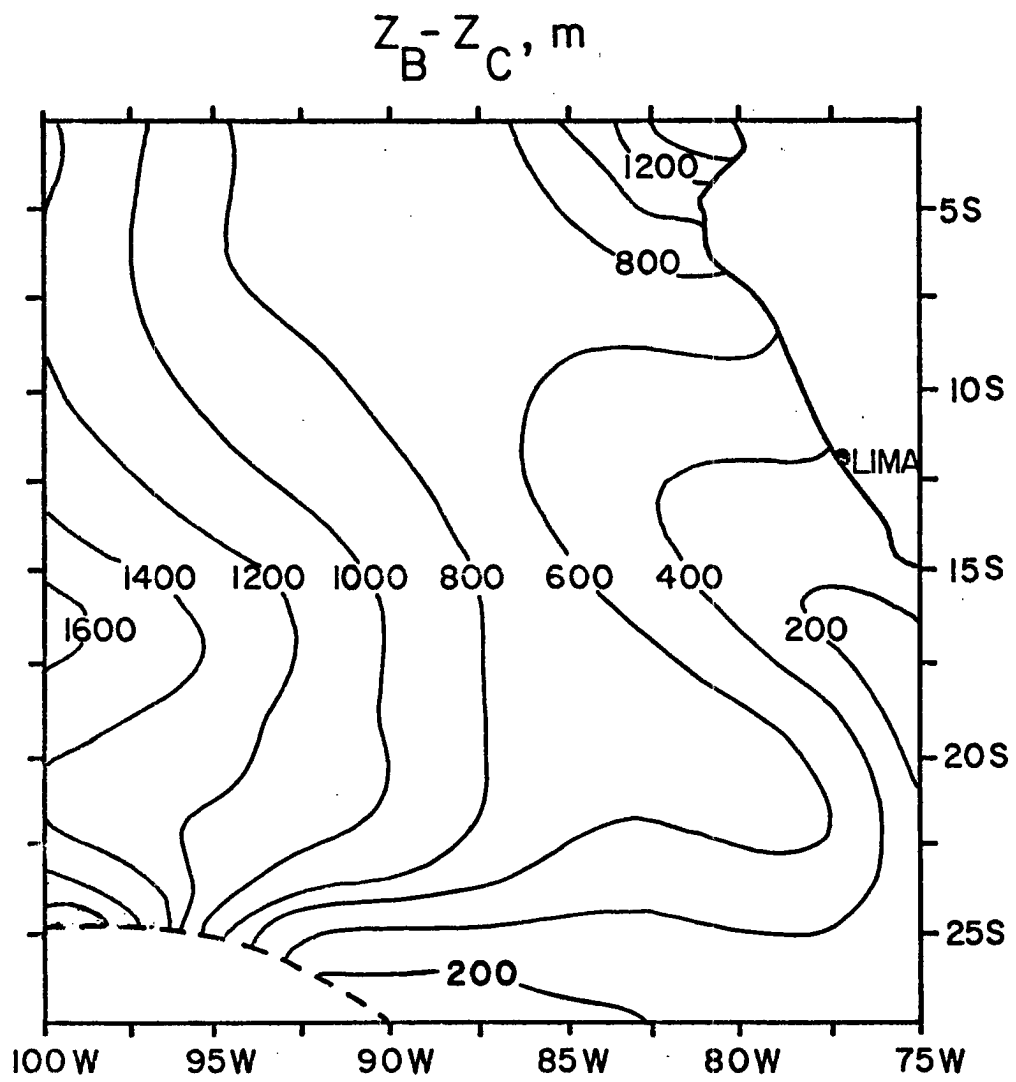


Figure 4.15c August depth of the cloud layer.

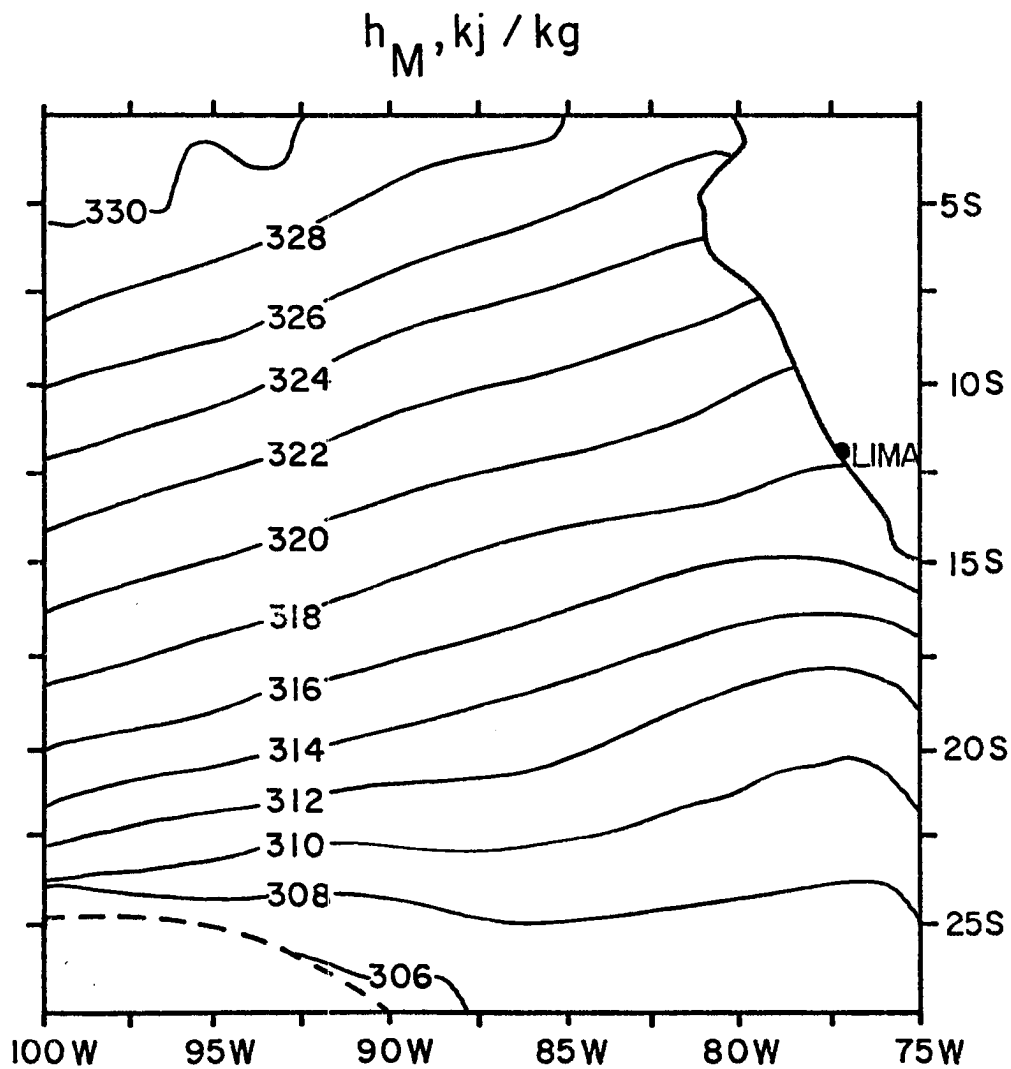


Figure 4.16a August mixed layer moist static energy.

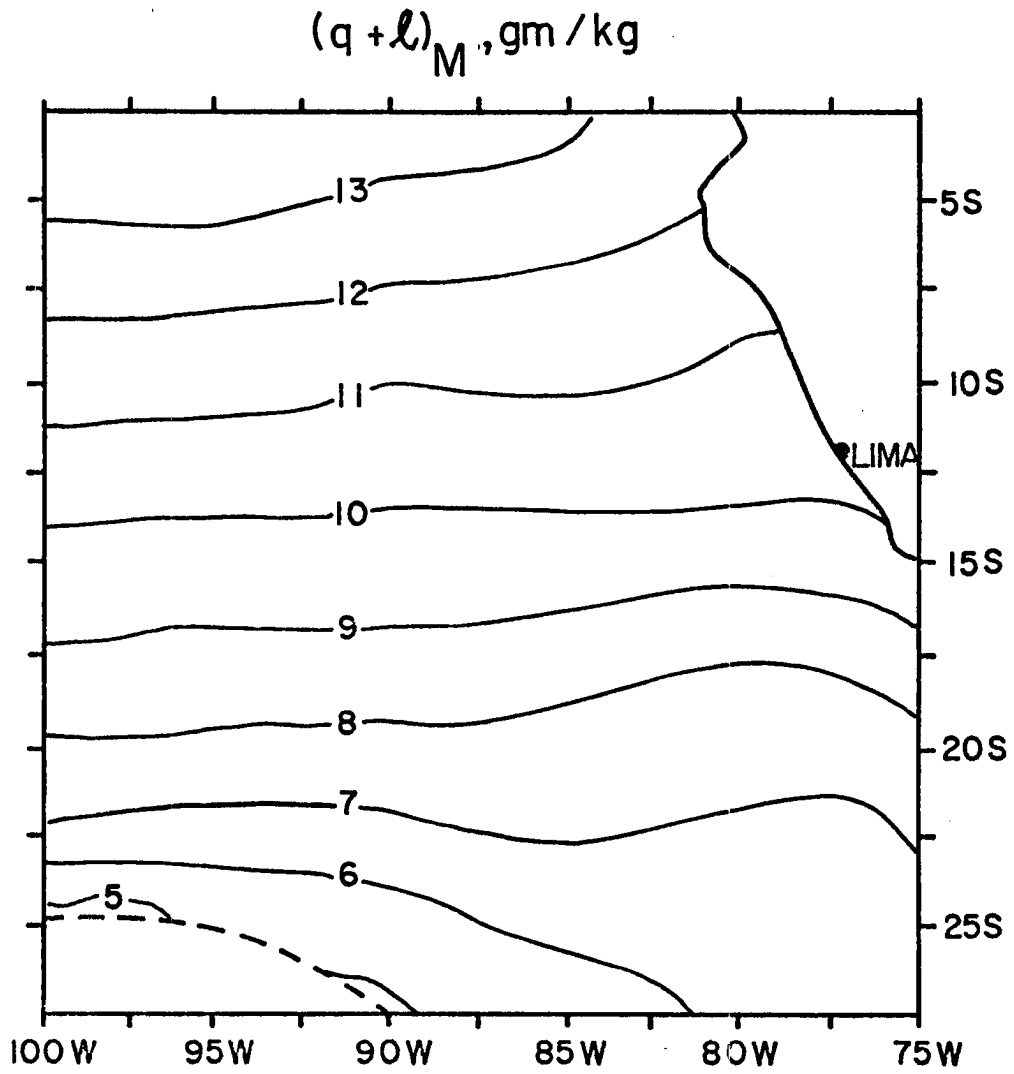


Figure 4.16b August mixed layer total water mixing ratio.

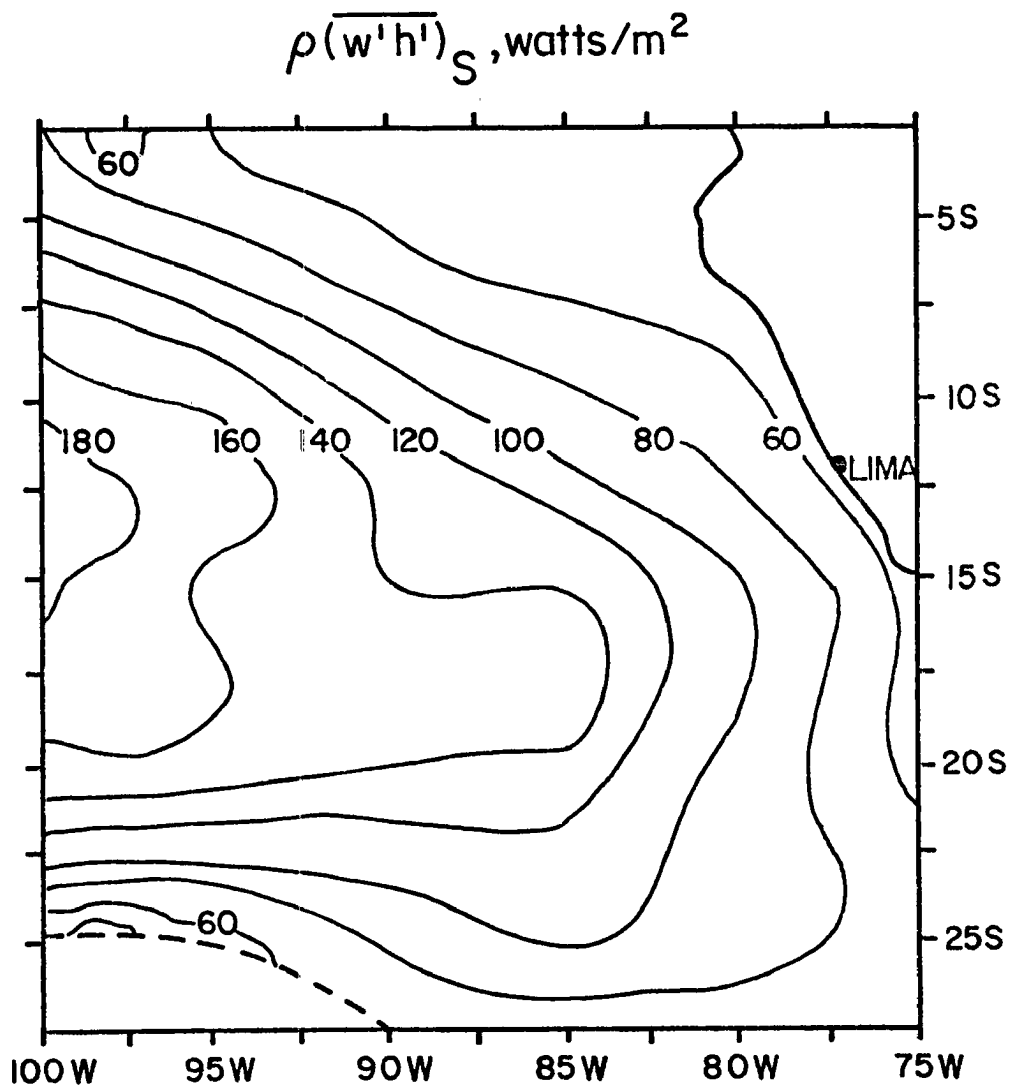


Figure 4.17a August turbulent flux of moist static energy at the surface.

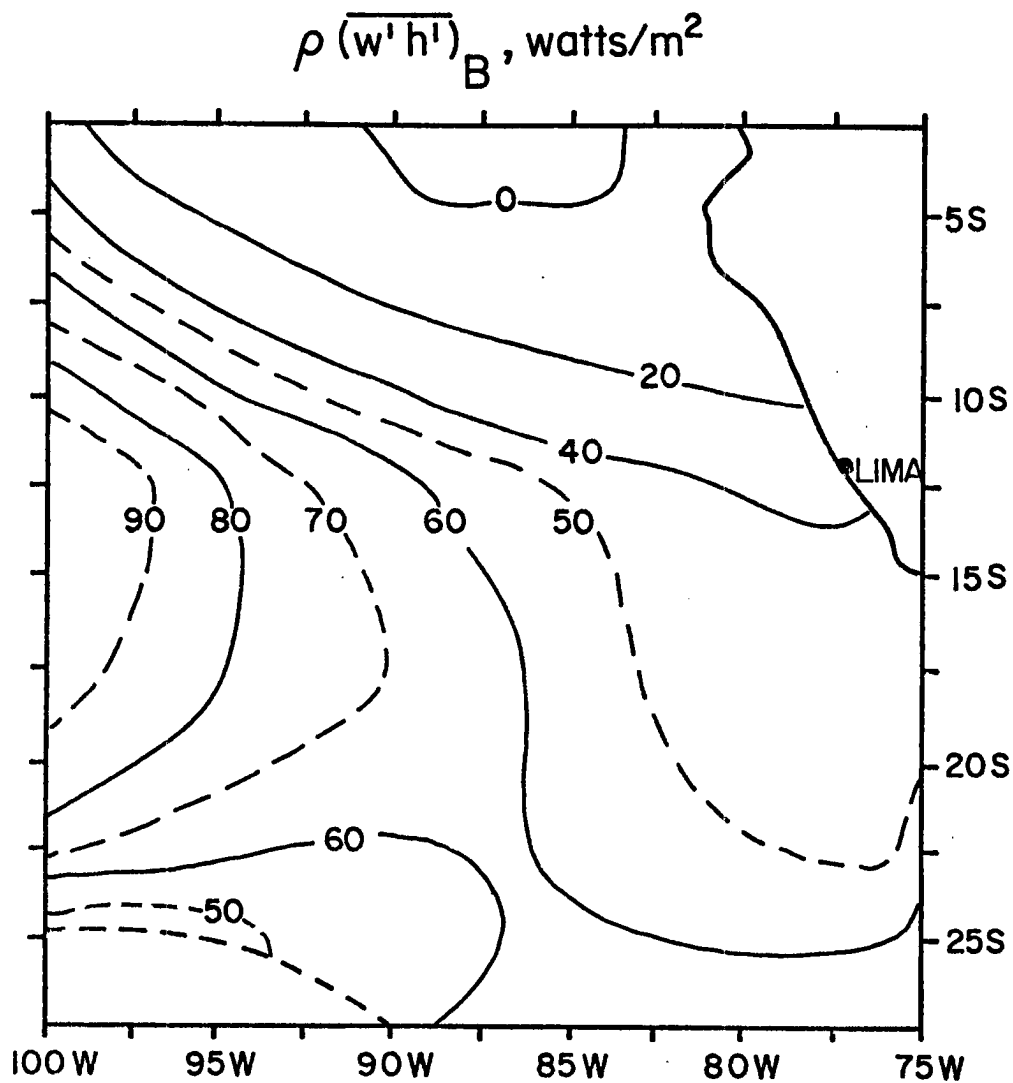


Figure 4.17b August turbulent flux of moist static energy at the top of the layer.

$$L\rho \overline{w'(q'+\ell')}_{S}, \text{watts/m}^2$$

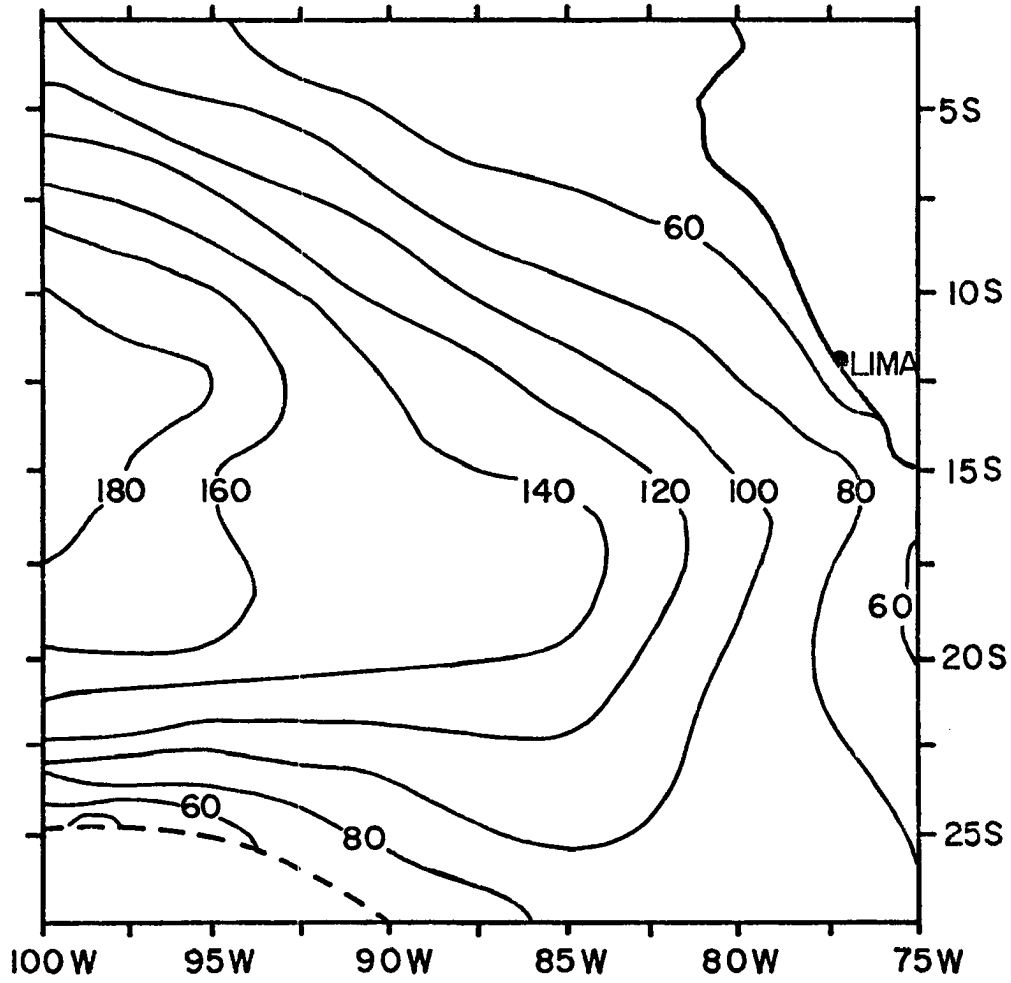


Figure 4.13a August turbulent flux of total water at the surface.

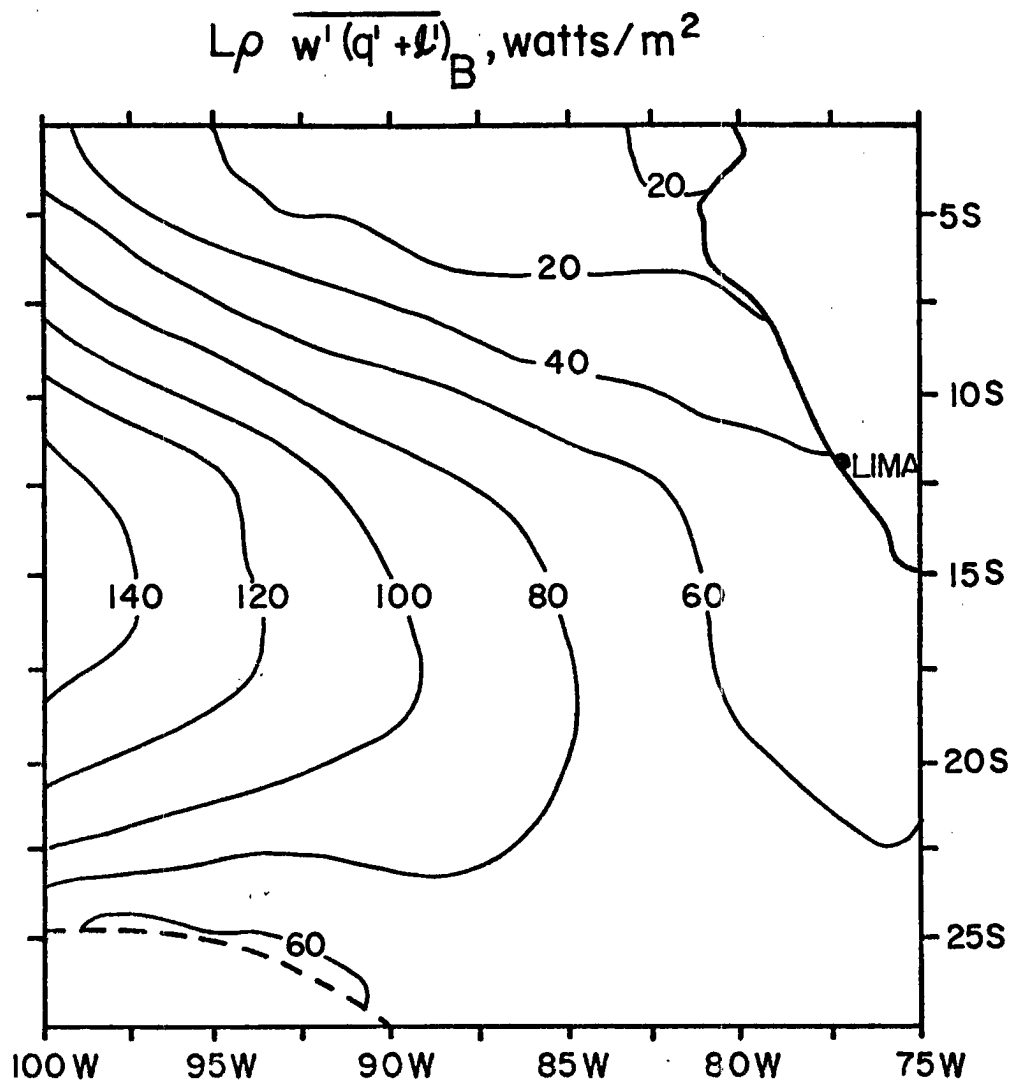


Figure 4.18b August turbulent flux of total water at the top of the layer.

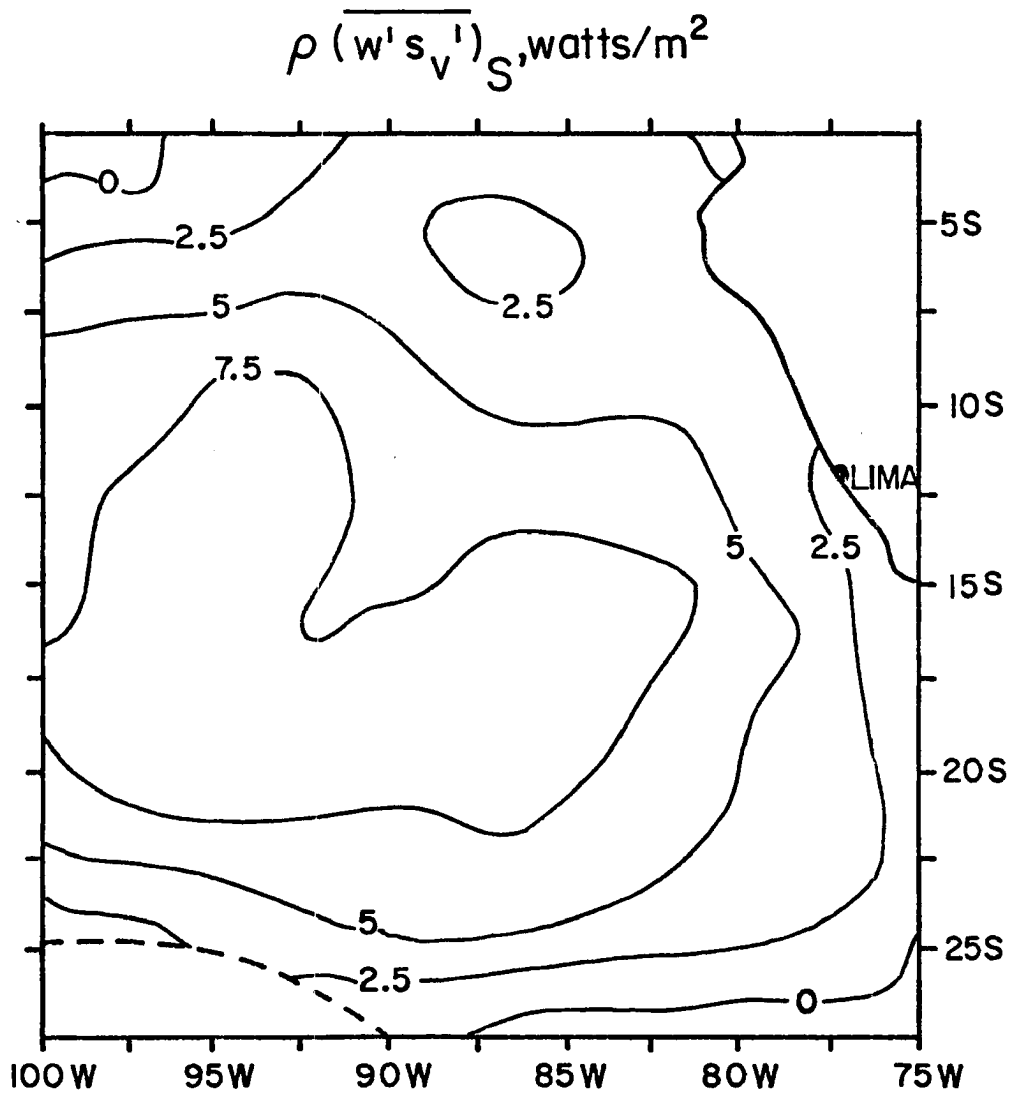


Figure 4.19a August turbulent flux of virtual dry static energy at the surface.

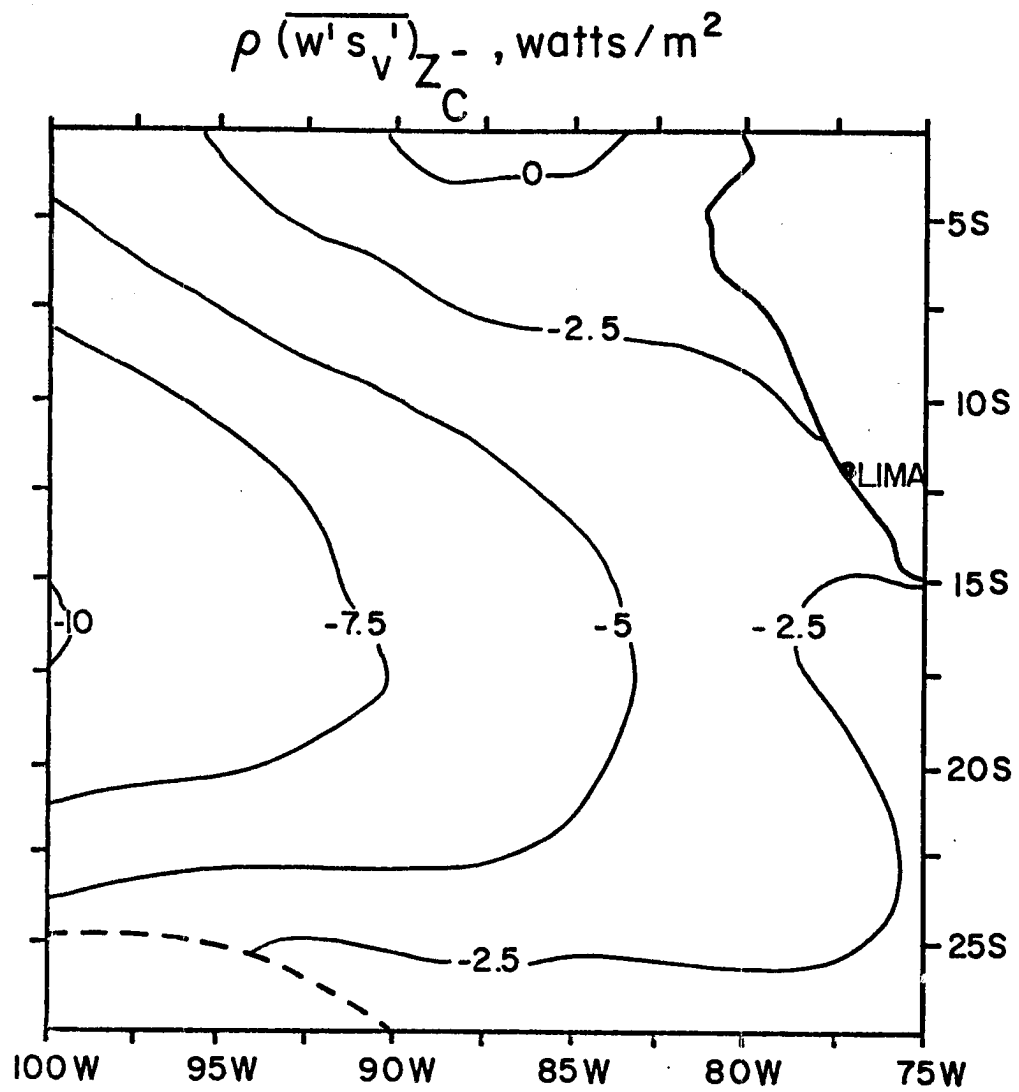


Figure 4.19b August turbulent flux of virtual dry static energy just below cloud base.

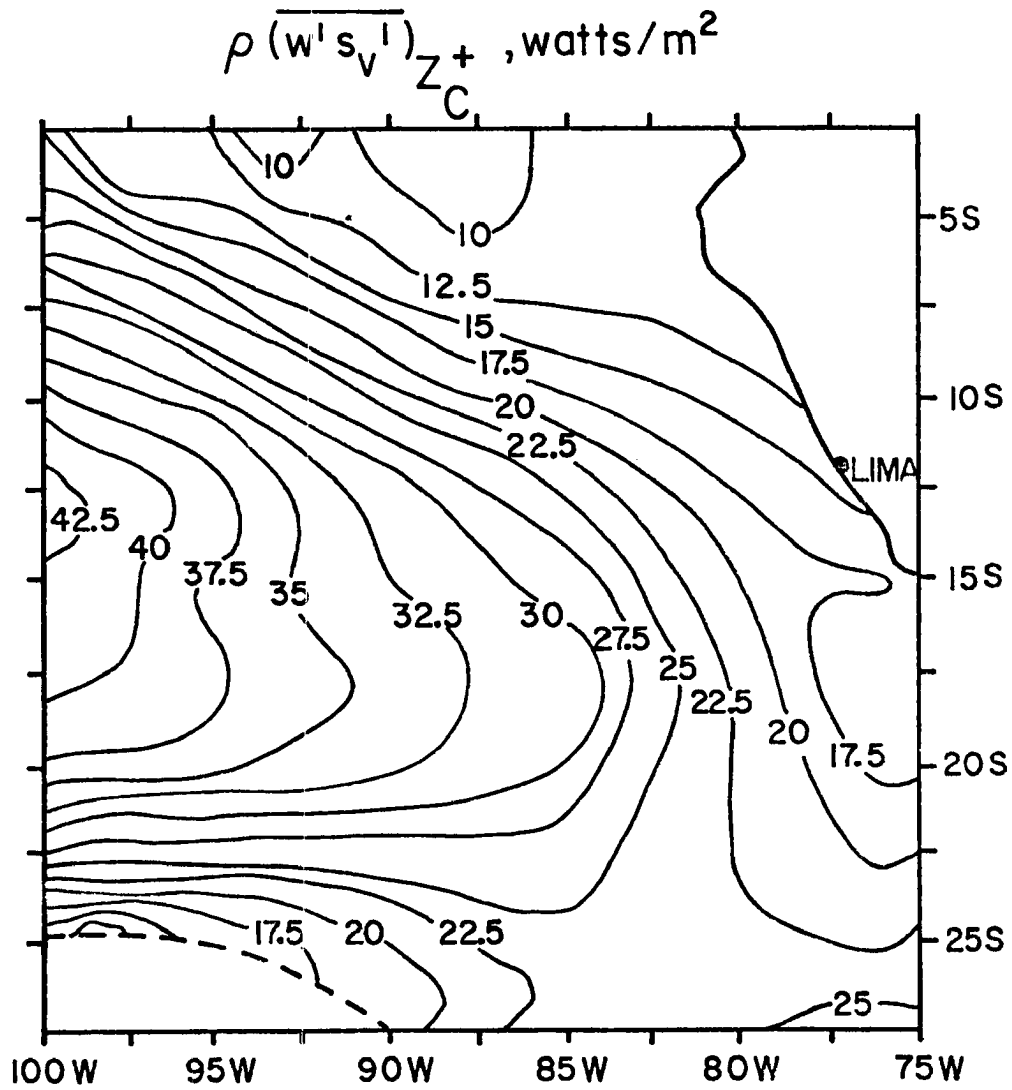


Figure 4.19c August turbulent flux of virtual dry static energy just above cloud base.

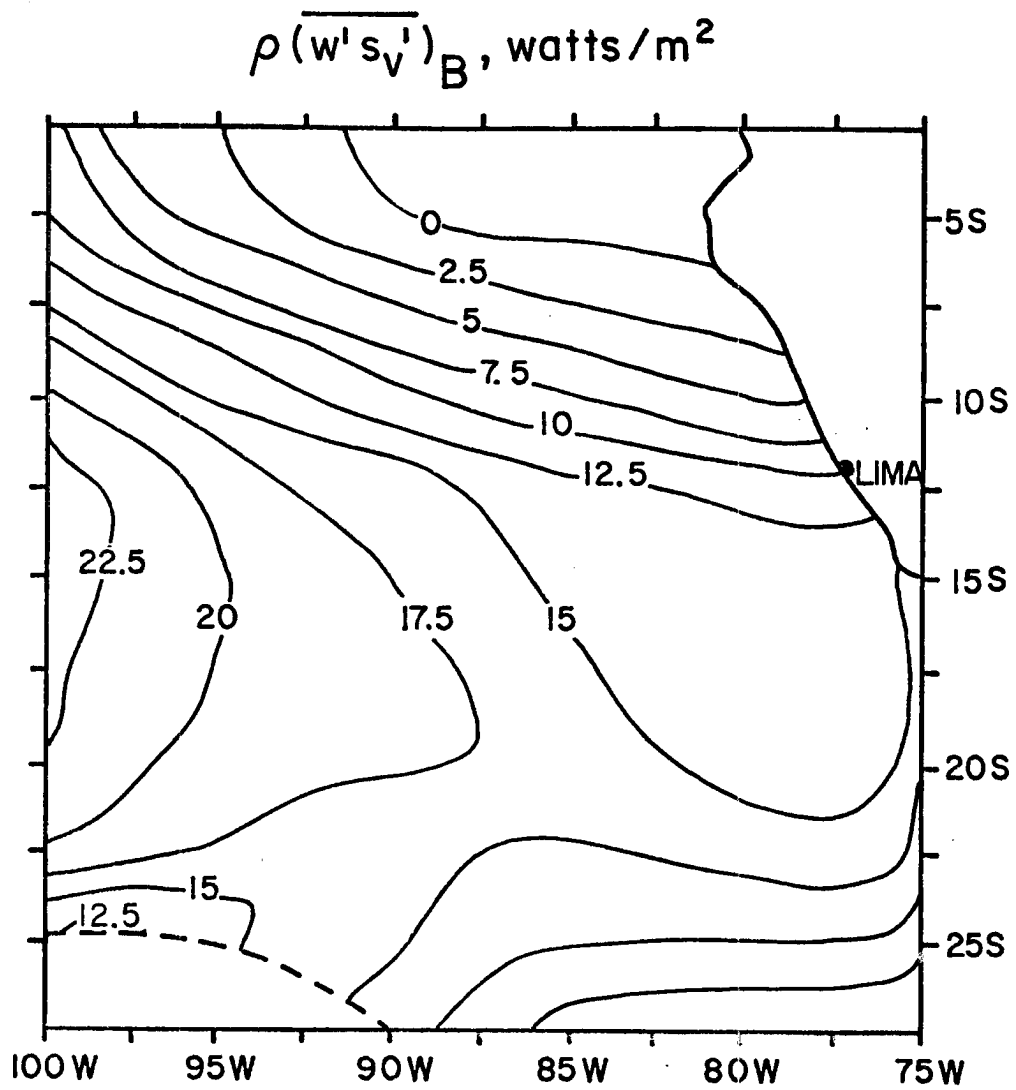


Figure 4.19d August turbulent flux of virtual dry static energy at layer top.

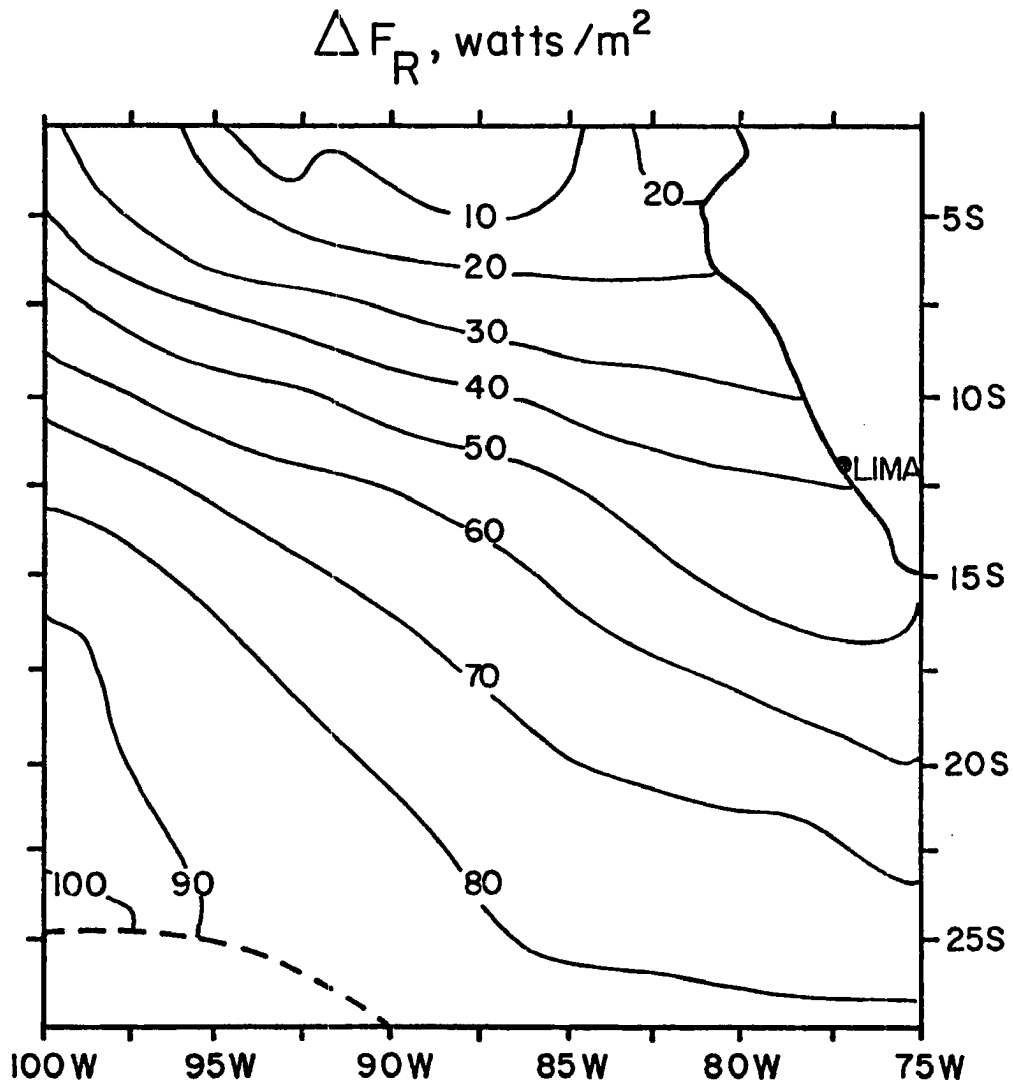


Figure 4.20 August jump of total radiative flux at cloud top.

Thus, the model is sensitive to the complex interactions between slight changes in these parameters.

4.3 Results of the July Case with No Solar Absorption

The input fields for the case of July with no solar absorption are, of course, the same as those for July with solar absorption. Also, H , ρ , ϵ , γ , β , and b are the same since they simply depend upon T_S . This case is easier than the August case to discuss because only one input parameter has been changed; therefore, any difference between these fields and the fields for July with solar absorption are due only to the absence of absorption. Clearly, all the fields in the no absorption case react the same way to T_S , V , and D as in the absorption case. Thus, the shape of the contours is very much the same, and the differences are primarily those of magnitude. Which fields differ the most, that is, in which fields does solar absorption play a greater role, is one question we shall explore in this section. The ΔF_R field for the no absorption case is presented for reference (Figure 4.25a).

The primary field in which we expect to see a difference, and an increase, is the z_B field (Figure 4.21a). z_B is indeed 200 m - 400 m higher in the absence of solar absorption, with a low of 1200 m rather than 1000 m, and a high of over 3800 m. 3800 m is higher than the tops of typical stratocumulus, so perhaps another type of cloud regime dominates this region. The same may be said for the regions of very high cloud top (above 2600 m) in the case with solar absorption. Because z_B is higher, the entrainment in the no absorption case (Figure 4.22) is also greater.

The z_C field too, rises in the absence of solar absorption (Figure 4.21b). In the no absorption case, $(q+l)_M$ is lower, accounting for the

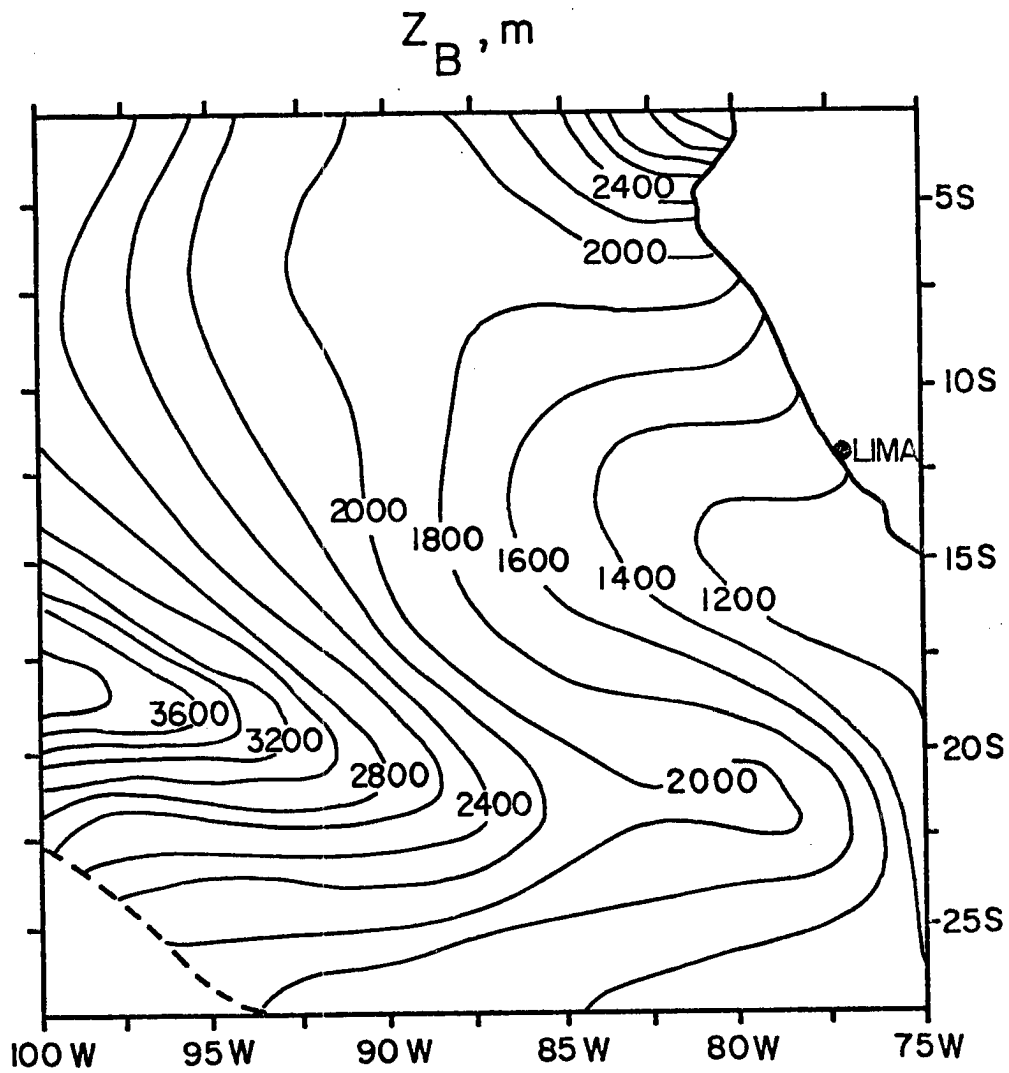


Figure 4.21a Cloud top for the July case with no solar absorption.

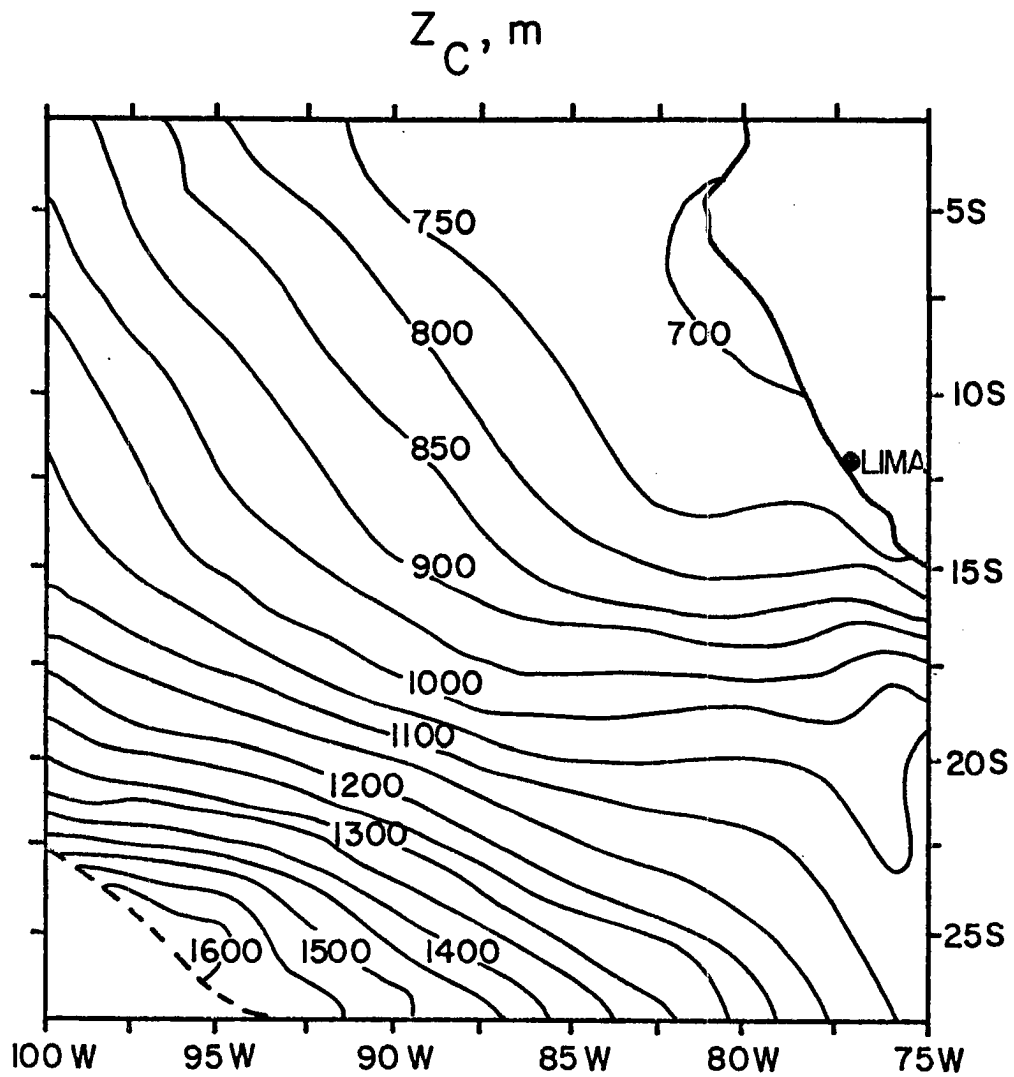


Figure 4.21b Cloud base for the July case with no solar absorption.

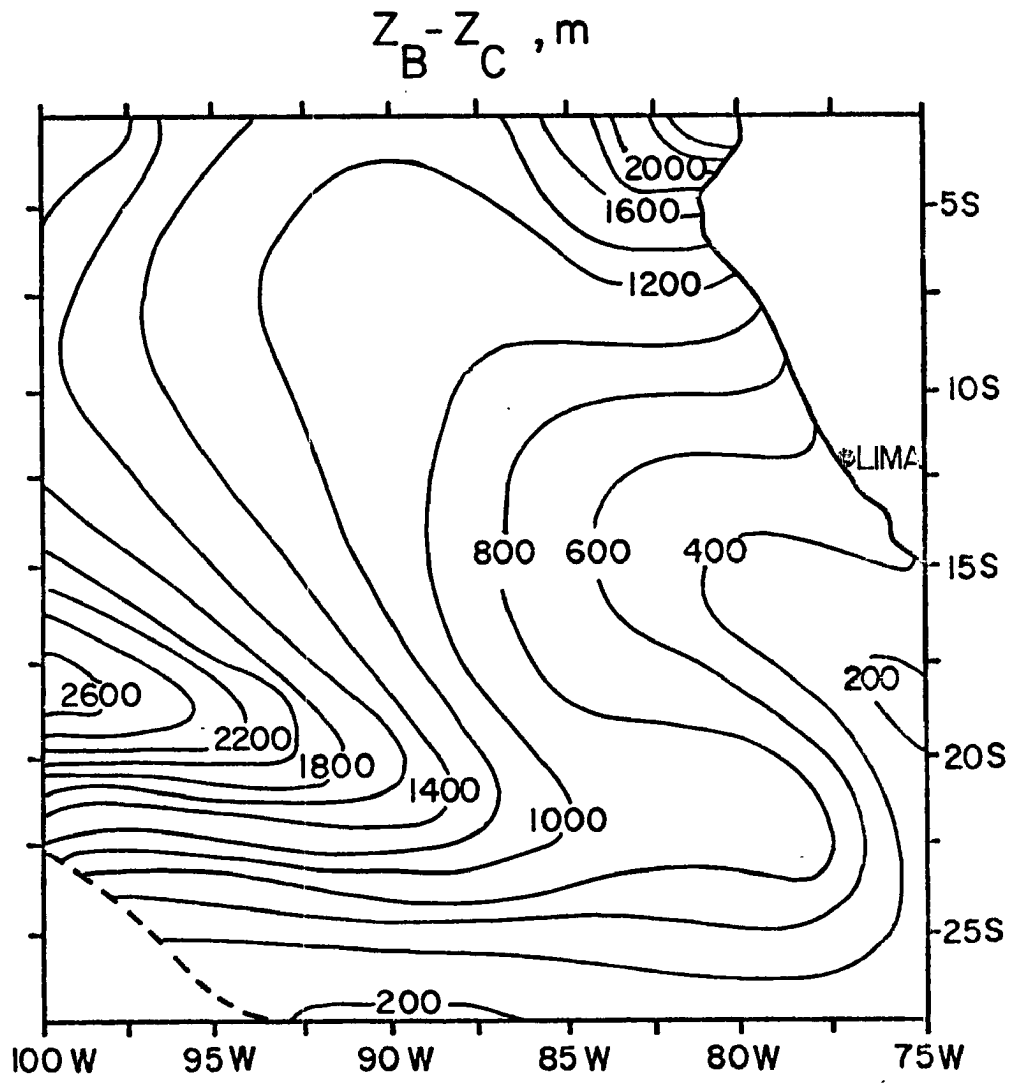


Figure 4.21c Depth of the cloud layer for the July case with no solar absorption.

higher z_C . In turn, the drier mixed layer may be due to greater entrainment of dry air at cloud top. Since $z_B - z_C$ (Figure 4.21c) is deeper in the no absorption case, we can conclude that the greater radiative cooling at cloud top is more effective in raising z_B than z_C .

Though h_M as well as $(q+l)_M$ is lower without solar absorption, one surprising model result is that $(s-Ll)_M$ is slightly higher. Because of greater cloud top radiative cooling, we initially expect the mixed layer to be cooler; however, the temperature is modified by the depth of the layer as well as other variables, and these lead to a slightly warmer subcloud layer. Correspondingly, there is a larger negative surface heat flux, given by $T_{\text{sea}} - T_{\text{air}}$ at surface, in the no absorption case (Figure 4.26).

The higher $\rho(\overline{w'h'})_S$ and $L\rho\overline{w'(q'+l')}_S$ fields correspond to the smaller h_M and $(q+l)_M$, while their fluxes at z_B are similar though somewhat higher downstream in the no absorption case (Figures 4.23 and 4.24). The $\rho\overline{w's_V}$ fields are much alike in both cases, with a higher jump across cloud base in the absence of solar absorption.

Finally, the higher z_B and lower h_M give rise to a significantly different Δh field (Figure 4.25b), with Δh more than 2 kJ/kg higher in many places. The zero line of Δh also begins farther to the west.

We can speculate that if we were to increase the solar absorption at cloud top to a maximum "high noon" value, we would see the same trends as in our no absorption and daily averaged absorption situations. That is, the cloud layer would sink and become shallower as the mixed layer would moisten.

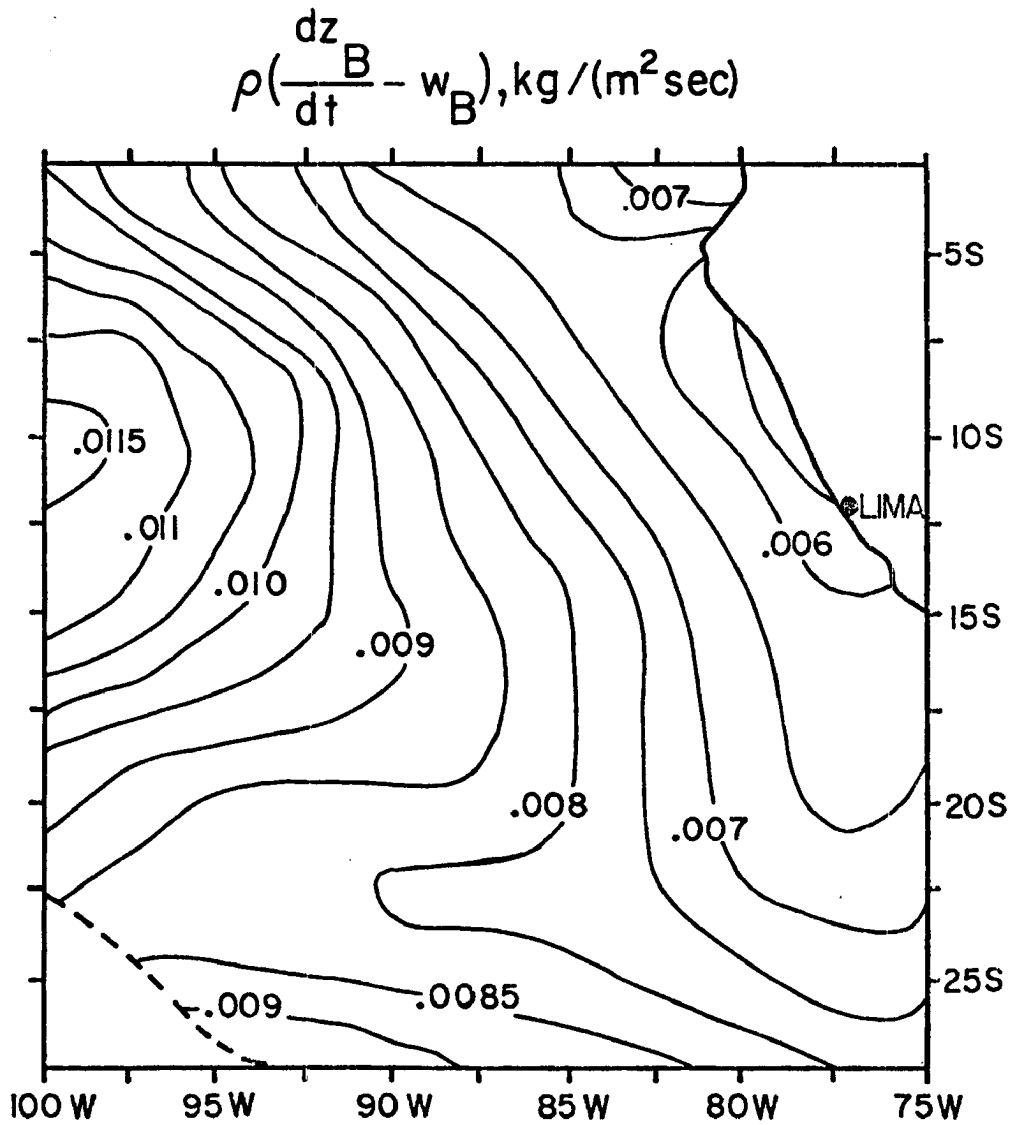


Figure 4.22 Mass entrainment at cloud top for the July case with no solar absorption.

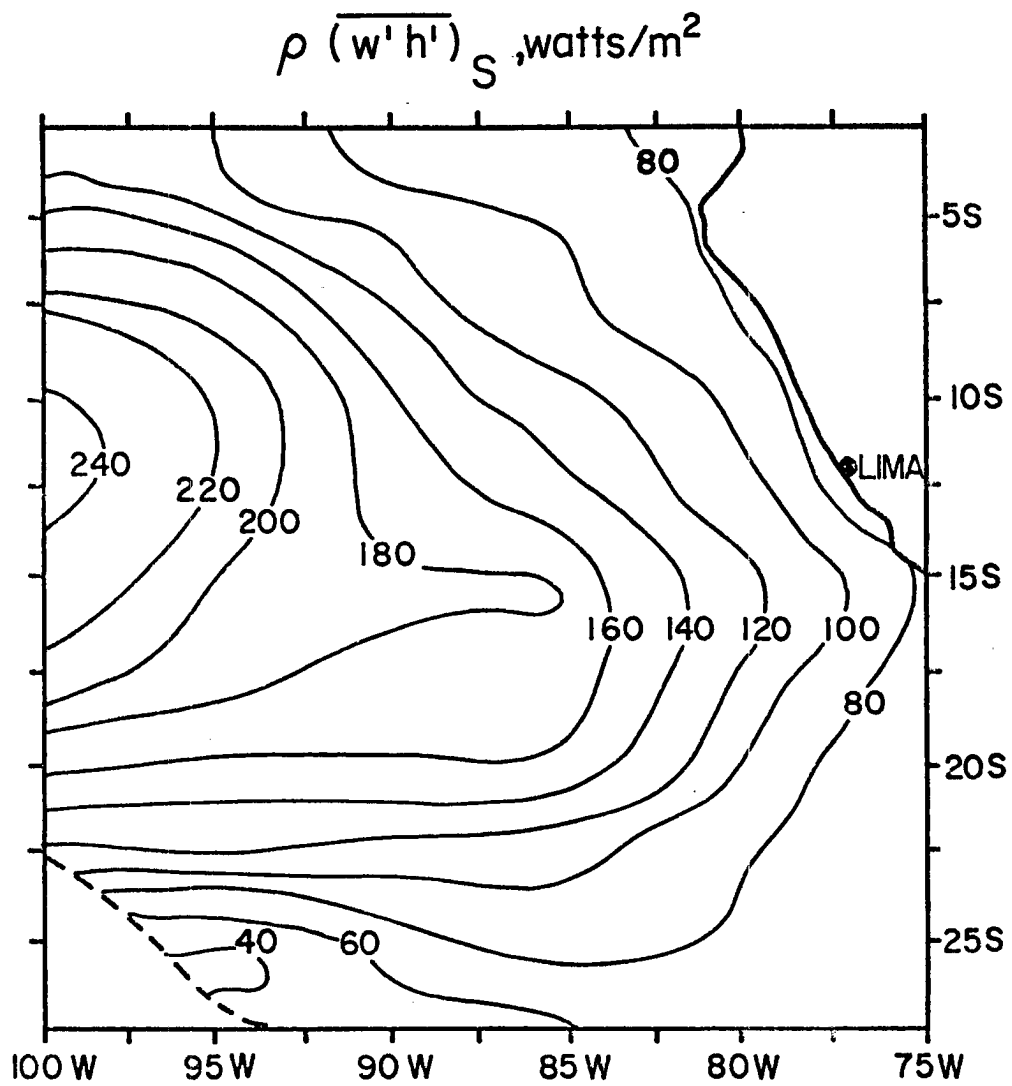


Figure 4.23a Turbulent flux of moist static energy at the surface for the July case with no solar absorption.

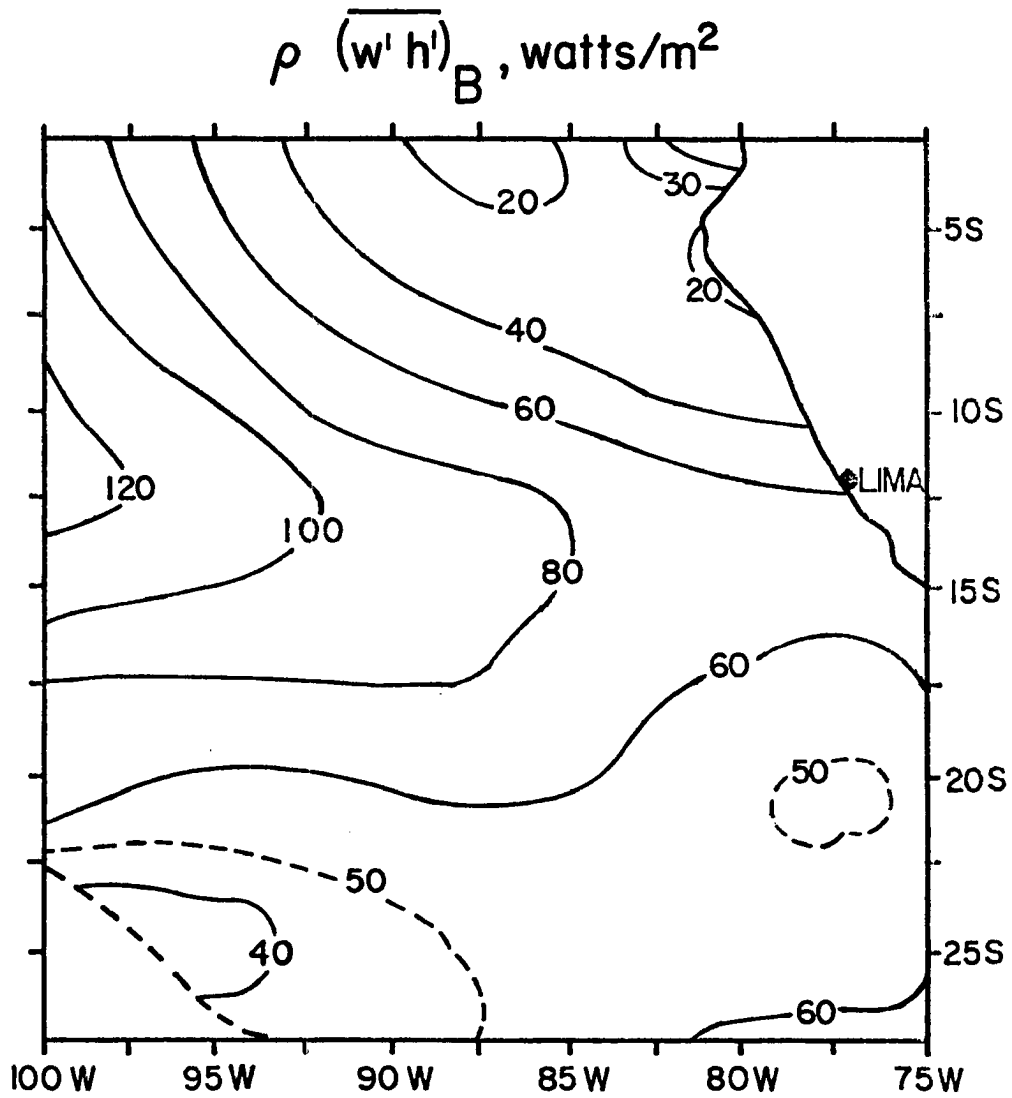


Figure 4.23b Turbulent flux of moist static energy at the top of the layer for the July case with no solar absorption.

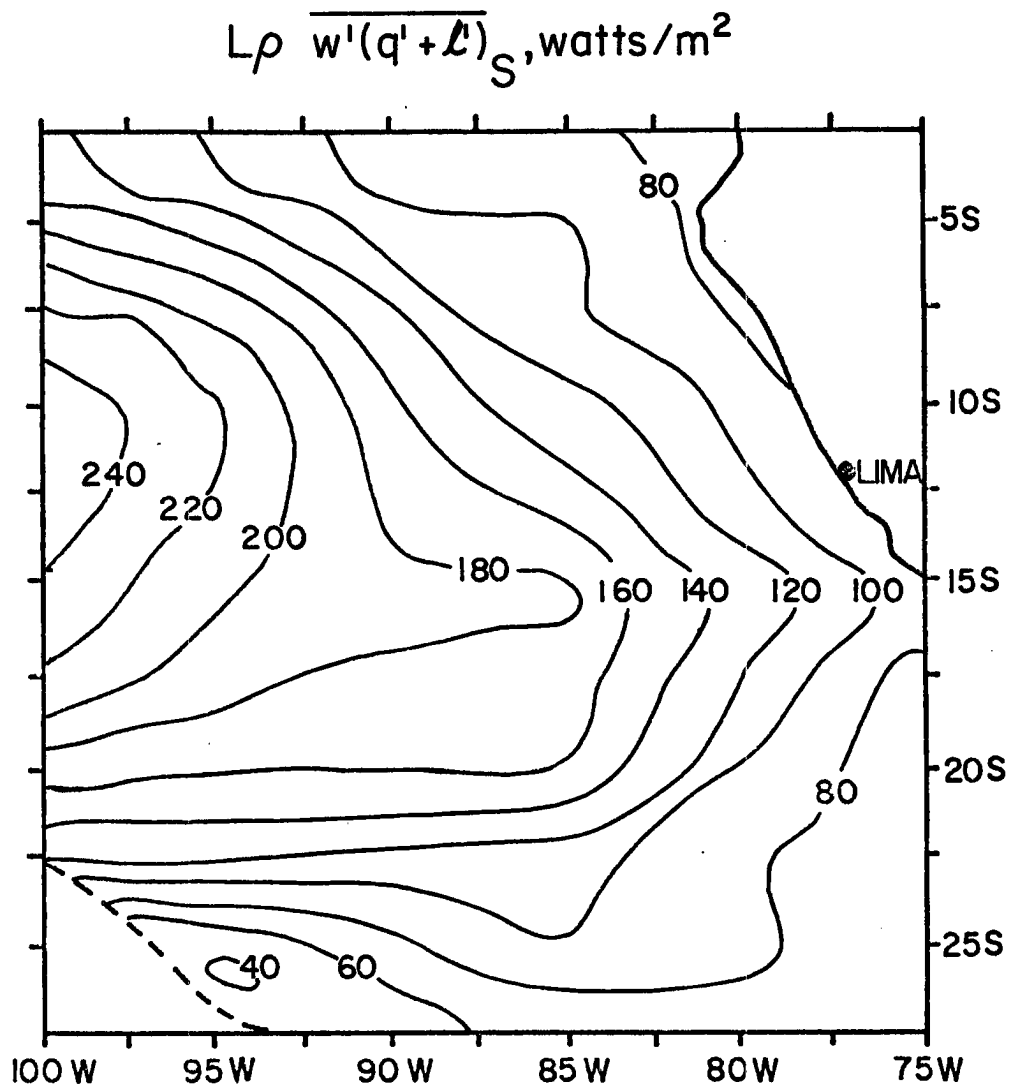


Figure 4.24a Turbulent flux of total water at the surface for the July case with no solar absorption.

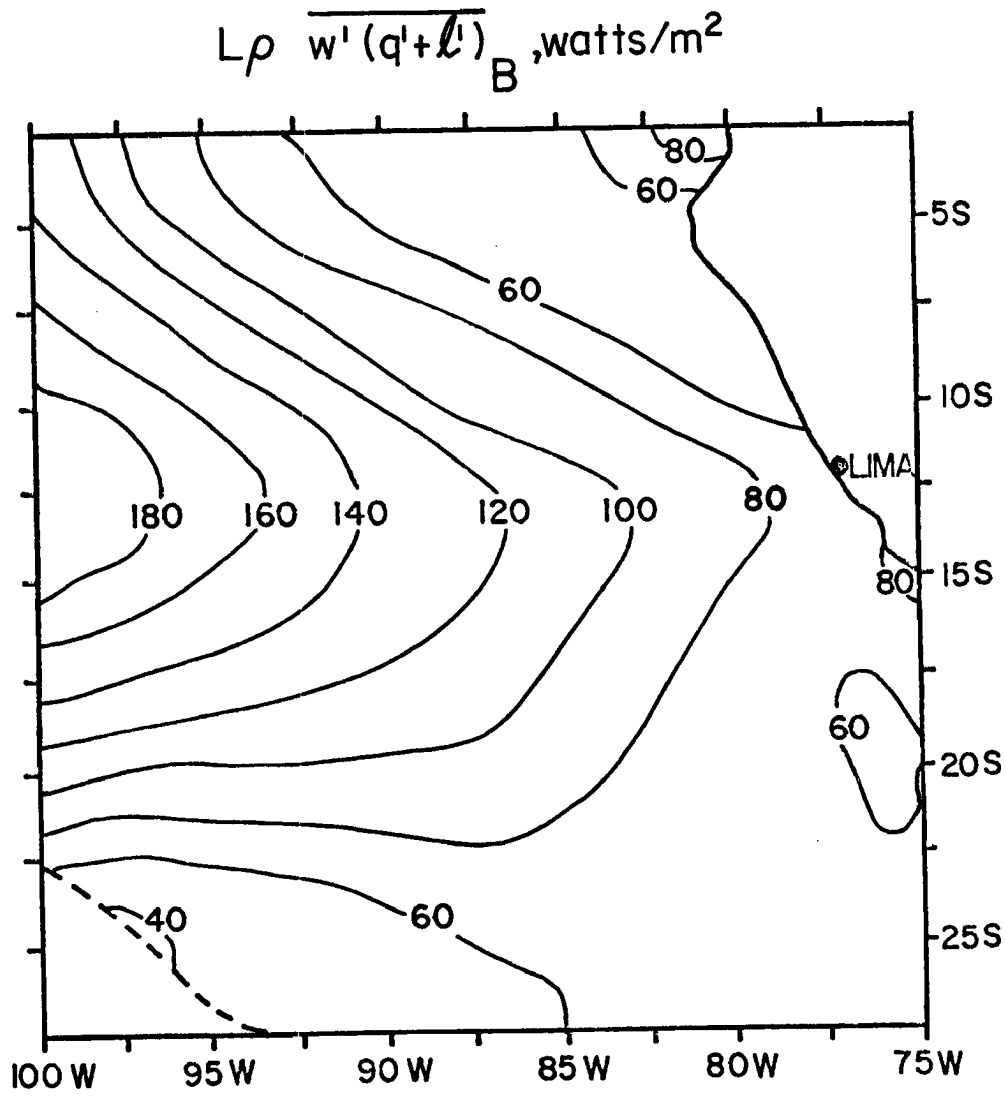


Figure 4.24b Turbulent flux of total water at the top of the layer for the July case with no solar absorption.

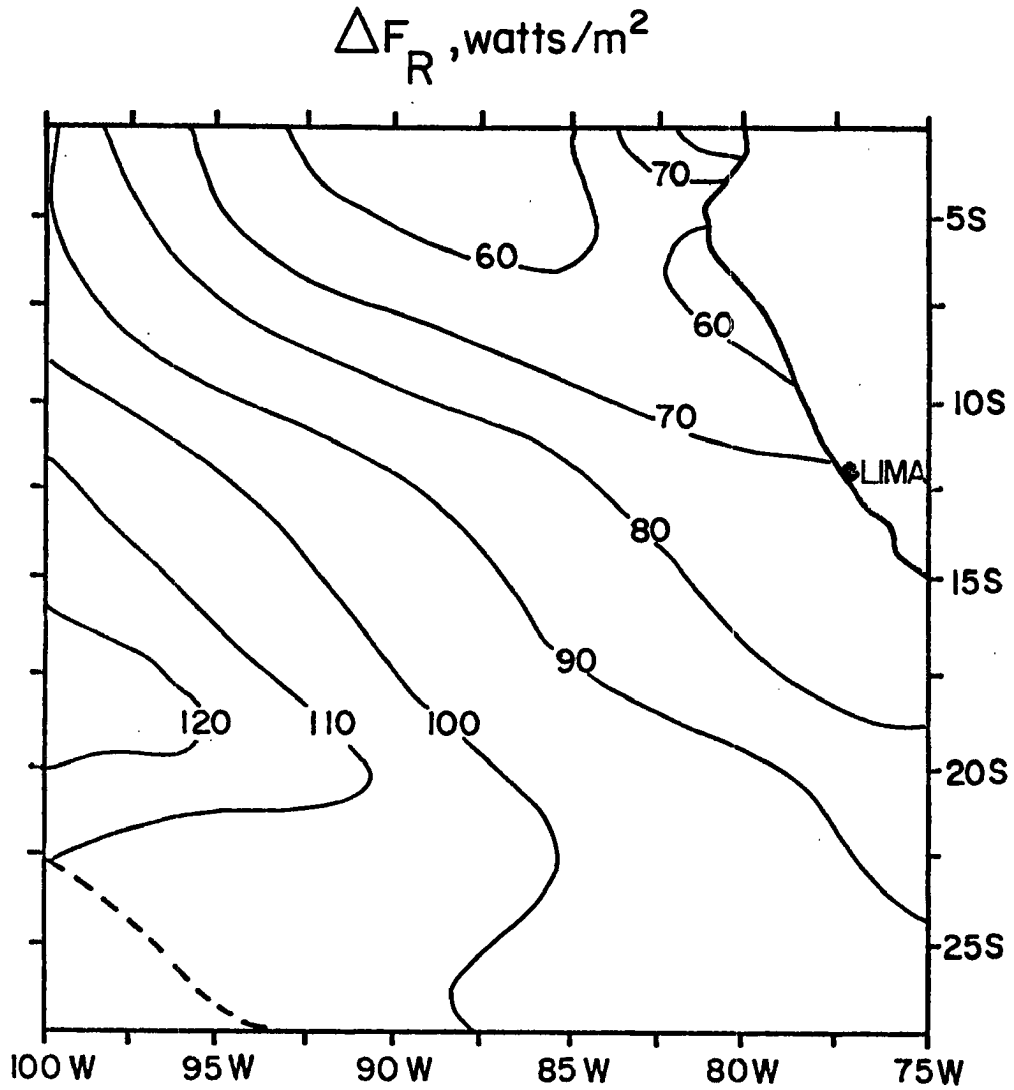


Figure 4.25a Jump of total radiative flux at cloud top for the July case with no solar absorption.

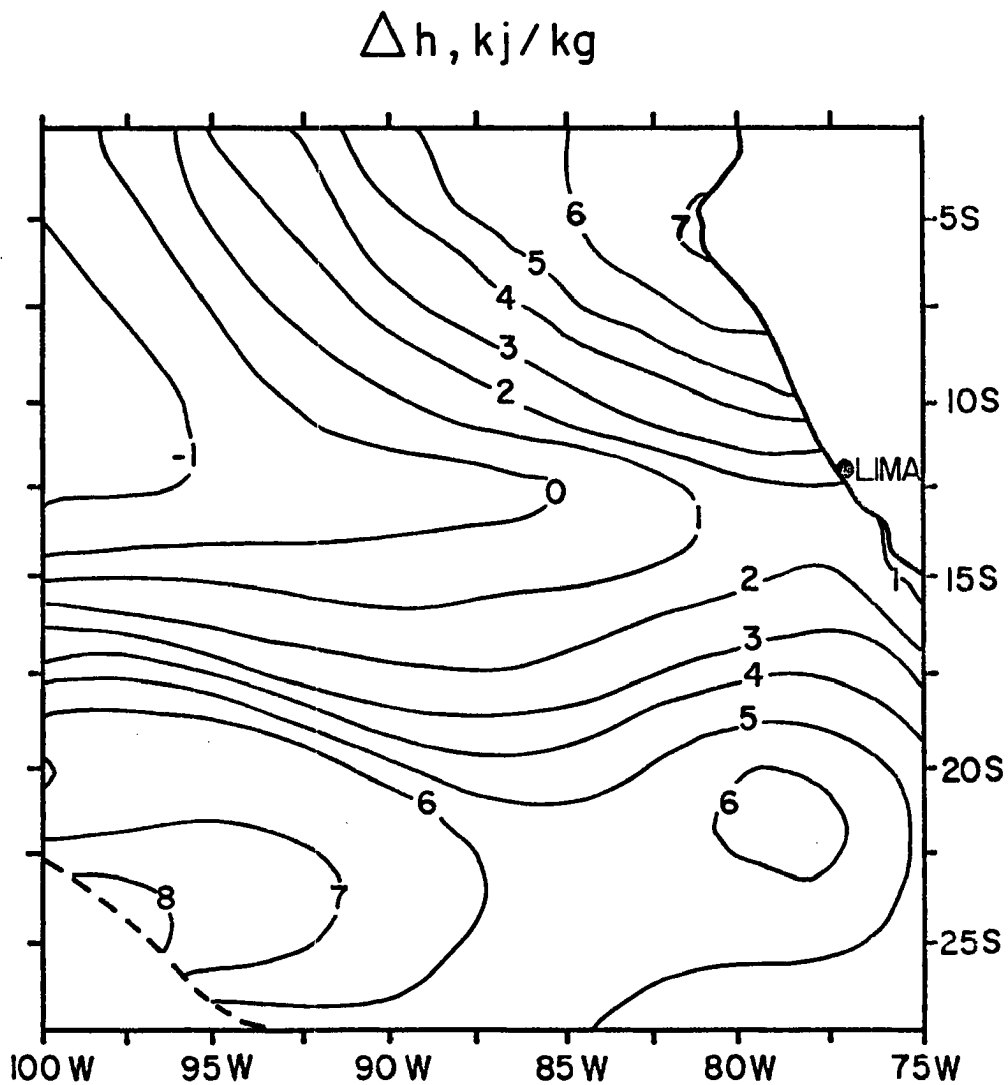


Figure 4.25b Jump of moist static energy at cloud top for the July case with no solar absorption.

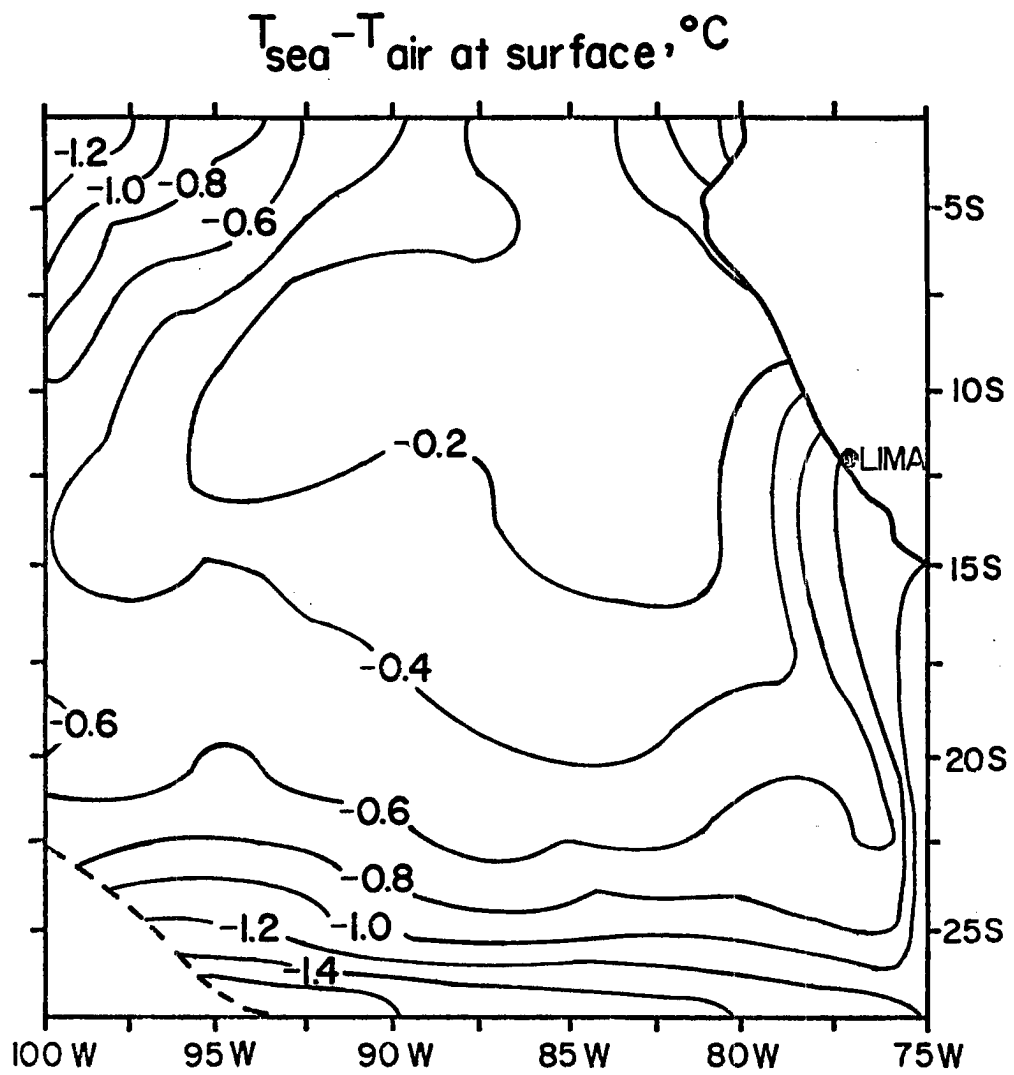


Figure 4.26 Difference between the sea surface temperature and the air temperature at the surface for the July case with no solar absorption.

4.4 Results of the July Case with a Different Initial Divergence

An additional experiment was performed initializing the July model with a divergence of $3.0 \times 10^{-6} \text{ sec}^{-1}$, which is closer to the average value of the divergence field. The fields principally affected by the lower divergence were the z_B and $z_B - z_C$ fields (Figures 4.27a and 4.27c), which were raised 200 m - 400 m. z_C is also slightly higher with the lower initial divergence (Figure 4.27b), and the Δh field (Figure 4.28) which requires $h(z_B(x)^+)$ rose as a result of the higher cloud tops. The remaining fields showed only slight increases or decreases, giving credence to their values as computed from the input parameters, rather than as functions of the initialization.

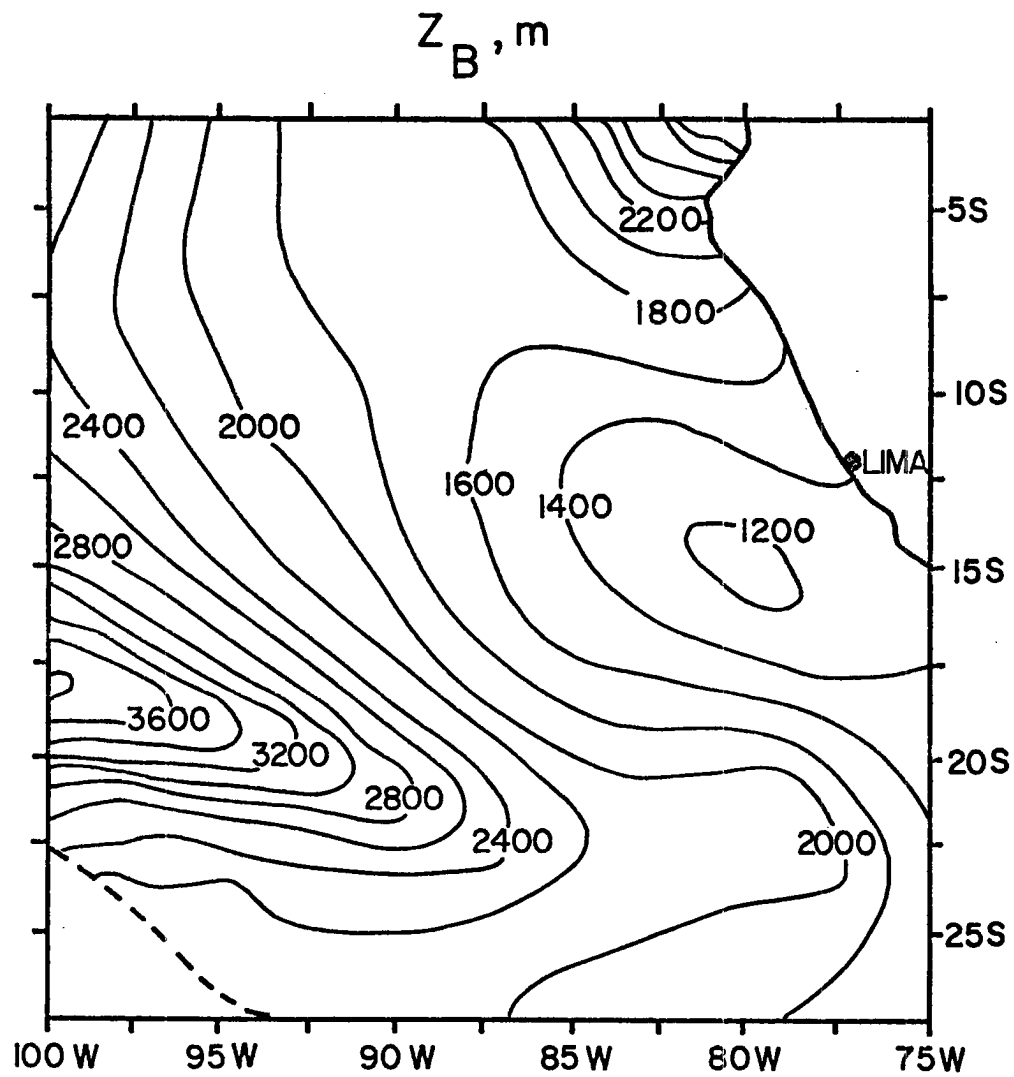


Figure 4.27a Cloud top for the July case with an initial divergence of $3.0 \times 10^{-6} \text{sec}^{-1}$.

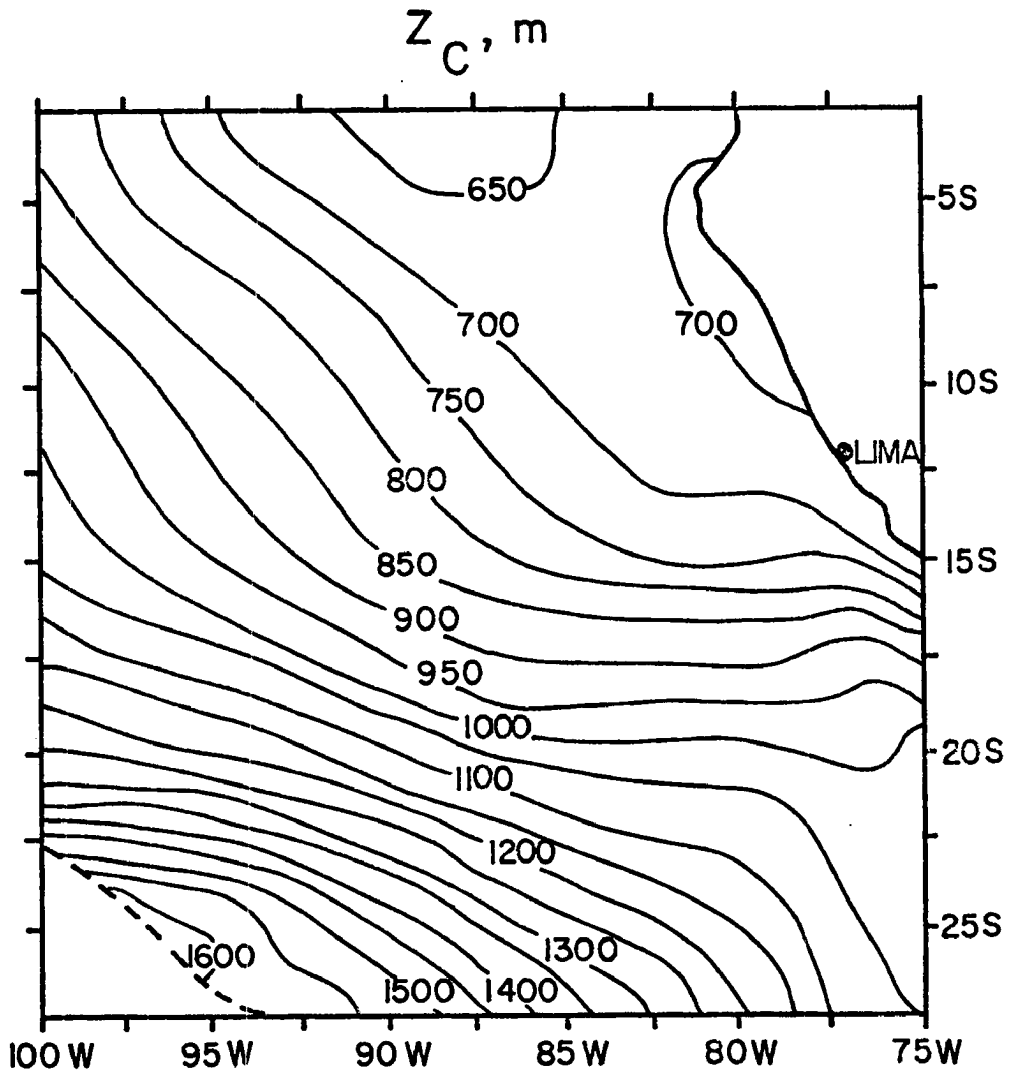


Figure 4.27b Cloud base for the July case with an initial divergence of $3.0 \times 10^{-6} \text{sec}^{-1}$.

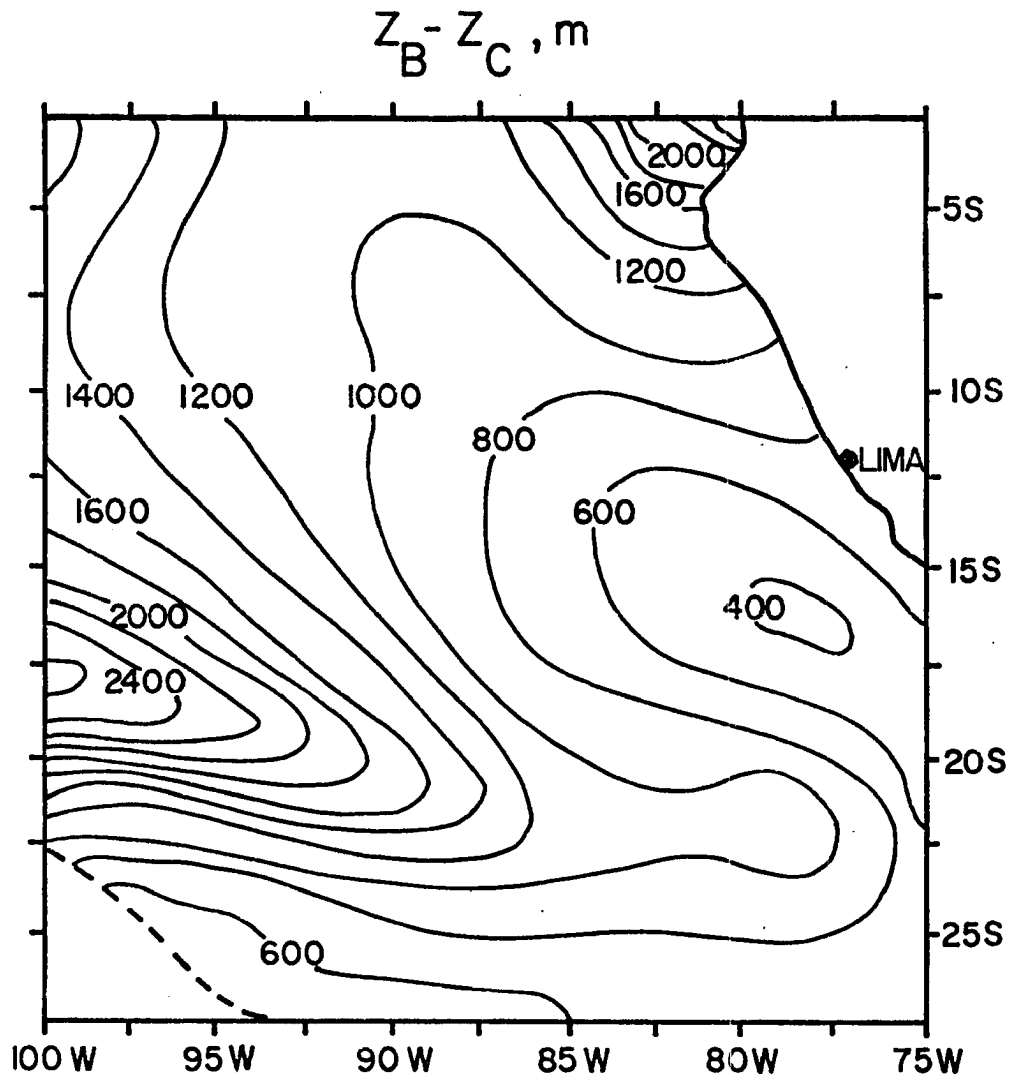


Figure 4.27c Depth of the cloud layer for the July case with an initial divergence of $3.0 \times 10^{-6} \text{sec}^{-1}$.

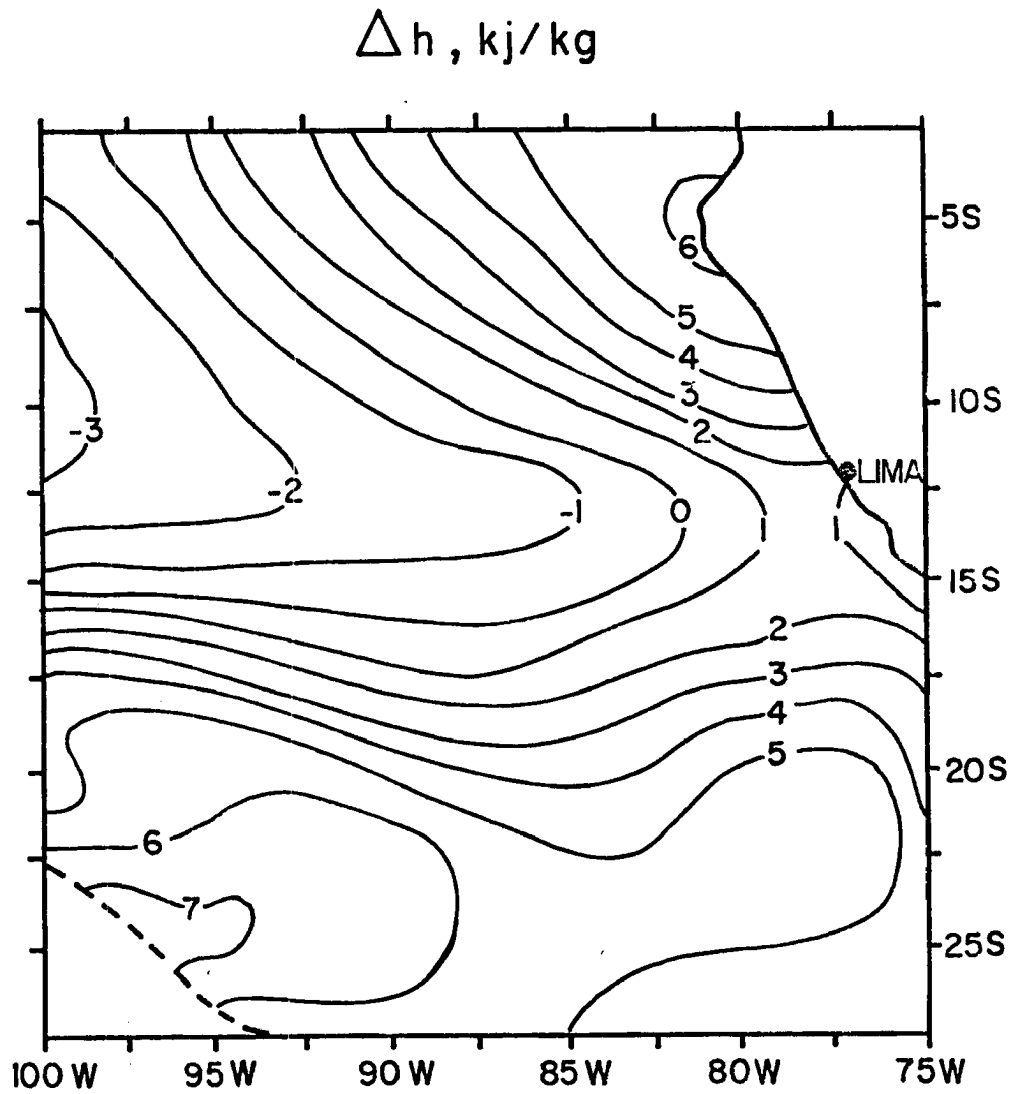


Figure 4.28 Jump of moist static energy at cloud top for the July case with an initial divergence of $3.0 \times 10^{-6} \text{sec}^{-1}$.

5.0 CONCLUSIONS

We have modeled the cloud-topped mixed layer as it moves towards the equator in the eastern South Pacific. The warmer equatorward sea surface temperatures cause increases in h_M and $(q+\ell)_M$, while cloud top height and depth are most strongly dependent upon divergence. In addition, we have gained information about the heat and moisture fluxes which are not as easy to determine observationally.

The August mixed layer was found to be lower and moister than that of July, as a result of only slight differences in the input parameters. In the July case with no solar absorption, that is, greater radiative cooling at cloud top, we found higher cloud tops and a thicker cloud layer.

Though the contour fields are relative, it is of some interest to examine their absolute numerical values. The cloud top and depth fields are somewhat higher than expected in view of data about stratocumulus in other regions of the globe, where average values of cloud top are 500 m - 2600 m and cloud depth from 200 m - 1000 m. Since cloud base itself is relatively high, mainly as a result of the temperature and moisture of the mixed layer, we might infer that the stratocumulus off the South American coast are, on the average, somewhat higher and deeper than stratocumulus observed in the northern hemisphere (Wakefield and Schubert, 1976; Neiburger, et al., 1961). Such a phenomenon may be related to the warmer sea surface temperatures off the South American coast. Though July and August are winter months in the southern hemisphere, the sea surface temperatures associated with the stratocumulus regime are several degrees higher than those associated with California

stratocumulus prevalent in the northern hemisphere summer. These warmer temperatures exist because the South American stratocumulus occur so much closer to the equator, a result of the northward shifted Hadley cell. It is likely that had our sea surface temperature data shown upwelling, the cloud top heights (near the coast, at least) would have been somewhat lower. It would be interesting to see if our hypothesized higher South American stratocumulus is verified by data.

The handling of the radiation also has an effect upon the model. Figure 3.3 was derived for clear conditions. It is also possible to impose an upper level cirrus on the soundings for the three stations; this increases the downward longwave radiative flux and thus decreases the radiative cooling through the atmosphere below and at stratocumulus top, suppressing mixed layer growth. However, another effect of the cirrus is the decrease of the large-scale subsidence (Albrecht and Cox, 1975). This is because in the dry, nonturbulent air above the mixed layer, the subsidence warming balances the radiational cooling. With a decrease in subsidence, the mixed layer will grow faster. Thus, two opposing effects are at work when the radiation profiles are changed as a result of upper level cirrus. There is no feedback in our model between the radiative cooling and the surface divergence. However, since the divergence is obtained from an average of many days, with and without cirrus, this effect is implicitly included.

Another assumption that has bearing on our results is that all the solar absorption and longwave radiative cooling occurs in an infinitesimally thin layer at cloud top. If the solar absorption were spread throughout the cloud, ΔF_R would become larger, resulting in faster cloud top growth. If the longwave cooling were spread throughout the cloud,

ΔF_R would decrease, resulting in slower cloud top growth. Since the longwave term is of greater magnitude than the shortwave term, the net effect of confining all radiative processes to the very top of the cloud probably leads to an overestimation of ΔF_R and hence, cloud top growth. The assumption, however, is probably not a bad one. It has been theoretically determined that a large portion of both the solar absorption and longwave cooling occurs in about the upper 50 m of the cloud, and drops off (quite rapidly in the case of longwave cooling) with cloud depth. If we were to change the radiation assumption, we would have to change other model equations as well for consistency, and cause needless complication.

This model could further be pursued by imposing a diurnal oscillation upon it. If there were data with which to make comparisons, we might have a better idea of how to initialize the model to yield better absolute numerical results. Also, it might be possible to couple our boundary layer model to an oceanic boundary layer model.

REFERENCES

- Albrecht, B., and S. K. Cox, 1975: The large-scale response of the tropical atmosphere to cloud-modulated infrared heating. J. Atmos. Sci., 32, pp. 16-24.
- Cox, S. K., 1973: Infrared heating calculations with a water vapor pressure broadened continuum. Quart. J. Roy. Meteor. Soc., 99, pp. 669-679.
- Cox, S. K., M. C. Polifka, K. Griffith, A. Rockwood and D. Starr, 1976: Radiative transfer computational routines for atmospheric science applications. CSU, Department of Atmospheric Science Report.
- Deardorff, J. W., 1976: On the entrainment ratio of a stratocumulus-topped mixed layer. Quart. J. Roy. Meteor. Soc., 102, pp. 563-582.
- Edinger, J. G., 1963: Modification of the marine layer over coastal southern California. J. Meteor., 2, pp. 706-712.
- James, D. G., 1959: Observations from aircraft of temperatures and humidities near stratocumulus clouds. Quart. J. Roy. Meteor. Soc., 85, pp. 120-130.
- Kraus, E. B., 1963: The diurnal precipitation change over the sea. J. Atmos. Soc., 20, pp. 551-556.
- Lenschow, D. H., 1972: Two examples of planetary boundary layer modification over the Great Lakes. J. Atmos. Sci., 30, pp. 568-581.
- Lilly, D. K., 1968: Models of cloud-topped mixed layers under a strong inversion. Quart. J. Roy. Meteor. Soc., 94, pp. 292-309.
- Miller, D. B., and R. G. Feddes, 1971: Global atlas of relative cloud cover 1967-1970. Joint production by U.S. Dept. of Commerce at U.S. Air Force, Washington, D. C. (Available from NTIS, Springfield, Virginia, AD739 434).
- Neiburger, M., 1949: Reflection, absorption, and transmission of insolation by stratus clouds. J. Meteor. 6, pp. 98-104.
- Neiburger, M., D. S. Johnson, and C. W. Chien, 1961: Studies of the structure of the atmosphere over the eastern Pacific Ocean in summer, I, The inversion over the eastern north Pacific Ocean. Univ. Calif. Publ. Meteor., 1, No. 1.
- Paltridge, G. W., 1973: Atmospheric radiation and the gross character of stratiform cloud. J. Atmos. Sci., 31, pp. 244-250.
- Schubert, W. H., 1976: Experiments with Lilly's cloud-topped mixed layer model. J. Atmos. Sci., 33, pp. 436-445.

- Schubert, W. H., J. S. Wakefield, E. J. Steiner, and S. K. Cox, 1977: Marine stratocumulus convection. To be submitted to J. Atmos. Sci.
- Wakefield, J. S., and W. H. Schubert, 1976: Design and execution of the marine stratocumulus experiment. Atmos. Sci. Paper 256, Colorado State University, 74 pp.
- Washington, W. M., and L. G. Thiel, 1970: Digitized global monthly mean ocean surface temperatures. NCAR TN-54, National Center for Atmospheric Research, 30 pp.
- Wyrтки, K., and G. Meyers, 1975: The trade wind field over the Pacific Ocean, Part I. The mean field and the mean annual variation. HIG-75-1. Hawaii Institute of Geophysics, University of Hawaii, 55 pp.
- Wyrтки, K., and G. Meyers, 1976: The trade wind field over the Pacific Ocean. J. Appl. Meteor., 15, pp. 698-704.

BIBLIOGRAPHIC DATA SHEET	1. Report No. CSU-ATSP	2.	3. Recipient's Accession No.
4. Title and Subtitle Stratocumulus Convection Off the South American Coast		5. Report Date May, 1977	
		6.	
7. Author(s) Ellen J. Steiner and Wayne H. Schubert		8. Performing Organization Rept. No.	
9. Performing Organization Name and Address Department of Atmospheric Science Colorado State University Fort Collins, CO 80523		10. Project/Task/Work Unit No.	
		11. Contract/Grant No. (NSF) DES 74-11438 ATM 76-09370	
12. Sponsoring Organization Name and Address National Science Foundation		13. Type of Report & Period Covered	
		14.	
15. Supplementary Notes			
16. Abstracts The stratocumulus regime off the South American coast is investigated using a horizontally inhomogeneous version of Lilly's (1968) cloud topped mixed layer model. This model is coupled with a longwave radiation model devised by Cox (1973) and Cox et al. (1976). Computed are the mixed layer temperature and moisture structure and convective fluxes as the marine layer air moves equatorward along trajectories calculated from the mean surface wind field. By the calculation of many such trajectories, two dimensional fields of the model parameters were derived for the region bounded by 75°W and 100°W, and 2.5°S and 27.5°S. Model runs were made for mean July and August conditions, and sensitivity tests were performed to show the effects of solar absorption and different initial divergences. Variations in the mixed layer temperature and moisture structure, and convective fluxes are described for each of these experiments.			
17. a. Keywords and Document Analysis. 17a. Descriptors Boundary Layer Cloud-topped Mixed Layer Marine Layer Mixed Layer Stratocumulus Clouds			
17b. Identifiers/Open-Ended Terms			
17c. COSATI Field/Group			
18. Availability Statement:		19. Security Class (This Report) UNCLASSIFIED	21. No. of Pages 97
		20. Security Class (This Page) UNCLASSIFIED	22. Price